Terahertz Nonlinear Optics of Graphitic Materials: From THz Pulse Manipulation to High-Harmonic Generation

Ali Maleki

Thesis submitted to the University of Ottawa
in partial Fulfillment of the requirements for the
Doctorate in Philosophy degree in Physics-Photonics

Department of Physics
Faculty of Science
University of Ottawa

Abstract

This thesis investigates the nonlinear optical behavior of graphitic materials in the terahertz (THz) frequency regime, with a focus on enhancing and understanding strong-field light–matter interactions in graphene and its derivatives, including graphene oxide (GO) and its reduced forms. By integrating theoretical modeling, numerical simulations, device fabrication, and experimental investigations of nonlinear THz phenomena, this work explores THz pulse manipulation and establishes a comprehensive platform for scalable and tunable THz nonlinear photonics.

We begin by establishing the theoretical foundations of THz nonlinear optics, including the derivation of the nonlinear wave equation, analysis of second- and third-order polarization responses, and the dynamics of carrier heating and saturable absorption in Dirac materials such as graphene. These concepts are experimentally realized using a high-field table-top THz system based on tilted-pulse-front optical rectification and electro-optic sampling. A key challenge in this regime—the detection of weak nonlinear signals amid broadband excitation in a noisy system—is addressed through the design and fabrication of metamaterial-based THz spectral filters featuring octave-wide bandwidths and high extinction ratios. These custom-built devices are engineered to shape the spectral content of the THz beam, enhance spectral isolation, and significantly improve detection sensitivity. In particular, a configuration of lowpass and highpass filters is developed to selectively transmit generated harmonic signals while suppressing the strong pump background, enabling reliable measurement of weak high-harmonic generation in subwavelength 2D samples.

Using this system, we demonstrate a multi-strategy platform for enhancing third-harmonic generation (THG) in graphene, integrating three complementary approaches: (i) stacking decoupled multilayer graphene sheets to increase the light–matter interaction length, (ii) applying electrical gating to dynamically modulate carrier density and optimize nonlinear conductivity, and (iii) coupling graphene with plasmonic metasurfaces to achieve strong local field enhancement. The synergy of these strategies leads to up to two orders of magnitude enhancement in THG efficiency, underscoring the critical role of both structural and

electronic tunability. Despite these gains, further improvement is limited by graphene's intrinsic linear absorption, which restricts the effective interaction length beyond a few layers. This motivates the use of alternative low-loss, tunable materials such as graphene oxide (GO), which combines reduced THz absorption, chemical flexibility, and access to nonlinear regimes beyond those of pristine graphene.

We next explore GO, a chemically functionalized derivative of graphene that features lower THz absorption and local symmetry breaking due to the presence of oxygen-containing functional groups. These groups can be gradually removed through chemical or thermal reduction, allowing for continuous tuning of GO's optical properties. Our experiments reveal a distinct nonlinear regime in GO, marked by the coherent generation of both odd and even-like harmonics, as well as a unique saturable transmission behavior under intense THz excitation. To interpret these effects, we develop a phenomenological two-level system model that accurately captures the field-dependent transmission response. This analysis identifies saturable transmission as a new symmetry-defying mechanism for wave mixing in functionalized 2D materials, enabling the generation of even-like harmonics without requiring long-range structural asymmetry.

Together, the results presented in this thesis establish graphitic materials—both pristine and functionalized—as versatile platforms for advancing nonlinear optics in the terahertz regime. By combining material engineering, device fabrication, and nonlinear spectroscopy, this work delivers a unified framework for probing and enhancing THz-driven light–matter interactions in 2D systems. The multi-strategy enhancement approaches for graphene, the discovery of novel nonlinear behavior in graphene oxide, and the implementation of spectral filtering and modeling tools all contribute to a powerful experimental and theoretical platform. This platform not only deepens our understanding of strong-field physics in low-dimensional materials, but also lays the groundwork for next-generation THz photonic technologies, including reconfigurable frequency converters, modulators, and integrated nonlinear devices.

List of Publications and Awards

Articles published in peer-reviewed journals

1. **A. Maleki**, M.B. Heindl, Y. Xin, R.W. Boyd, G. Herink, J.-M. Ménard, "Strategies to enhance THz harmonic generation combining multilayered, gated, and metamaterial-based architectures," *Light: Science & Application,* **14***,* 44 (2025). ***Featured on the cover of Light: Sci. Appl. and selected as an Editor's Highlight****.*
2. A. Jaber, M. Reitz, A. Singh, **A. Maleki,** Y. Xin, B.T. Sullivan, K. Dolgaleva, R.W. Boyd, C. Genes, and J.-M. Ménard, "Hybrid architectures for terahertz molecular polaritonics," *Nature Communications* **15**, 4427 (2024).
3. C. Zhang, E. K Yalavarthi, M. Giroux, W. Cui, M. Stephan, **A. Maleki**, A. Weck, J.-M. Ménard, R. St-Gelais, "High detectivity terahertz radiation sensing using frequency-noise-optimized nanomechanical resonators," *APL Photonics* **9**, 126105 (2024)
4. **A. Maleki**, A. Singh, A. Jaber, W. Cui, Y. Xin, B. T. Sullivan, R.W. Boyd, J.-M. Ménard, "Metamaterial-based octave-wide terahertz bandpass filters," *Photonics Research* **11**, 526 (2023).
5. L. Gingras, A. Jaber, **A. Maleki**, O. Reshef, R. Boyd, J.-M. Ménard et al. "Ultrafast modulation of the spectral filtering properties of THz metasurface," *Optics Express* **28,** 20296 (2020).

Manuscripts in Preparation

6. **A. Maleki,** L. Wang, I. Bargaoui, H. Heydarian, W. Cui, J-M. Guay, K. Dolgaleva, R.W. Boyd, T. Brabec, J.-M. Ménard, " Non-perturbative THz nonlinearities in graphene oxide resulting in even and odd harmonics," *Manuscript in preparation*, (2025)

Conference proceedings

All entries were oral presentations. The underlined author was the presenter.

1. **A. Maleki,** M.B. Heindl, Y. Xin, R.W. Boyd, G. Herink, J.-M. Ménard, "Enhanced THz nonlinearity in a multi-layer graphene device on a metasurface," *Photonics North* (2025)
2. **A. Maleki,** M.B. Heindl, Y. Xin, R.W. Boyd, G. Herink, J.-M. Ménard, "Enhanced THz third-harmonic generation in a graphene-metamaterial hybrid structure," *Advanced Photonics Congress* NpTh3C.3 (2024)
3. **A. Maleki**, A. Singh, A. Jaber, W. Cui, Y. Xin, B. T. Sullivan, R.W. Boyd, J.-M. Ménard, "Broadband THz bandpass filters based on multi-layered metasurfaces," *48th International Conference on Infrared, Millimeter, and Terahertz Waves (IRMMW-THz),* pp. 1-2 (2023)

4. A. Jaber, M. Reitz, A. Singh, **A. Maleki**, Y. Xin, B. Sullivan, K. Dolgaleva, R.W. Boyd, C. Genes, J-M. Ménard "Light-matter coupling between organic molecules and a THz metasurface," *48th International Conference on Infrared, Millimeter, and Terahertz Waves* (2023)
5. **A. Maleki,** A. Jaber, A. Singh, Y. Xin, J. M. Guay, O. Reshef, K. Dolgaleva, R. W. Boyd, B. Sullivan, J. M. Ménard, "Broadband bandpass THz filters with stacked metasurfaces," *OSA Advanced Photonics Congress*, NoM4C.4 (2021)
6. **A. Maleki,** A. Jaber, L. Gingras, O. Reshef, R. Boyd, J. M. Ménard, "FDTD analysis of a tunable THz plasmonic metasurface," *Frontier in optics and laser science, OSA*, FM7E.4 (2020).
7. A. Jaber, L. Gingras, **A. Maleki**, O. Reshef, R. Boyd, J. M. Ménard "Ultrafast Optical Control of a Terahertz Metasurface Filter," *OSA Advanced Photonics Congress*, NoM4C.1 (2020).

Awards and Honors

1. **Graduate Entrepreneurship Experience Program (GEEP)** – *Award Recipient*, University of Ottawa, 2025
2. **Desjardins Elevator Pitch Competition** – *First Place*, *Validation Category*, University of Ottawa, 2024
3. **Mitacs Globalink Research Award** – *Joint research program between the University of Ottawa and the University of Bayreuth (Germany)*, 2022
4. **Ontario Graduate Scholarship (OGS – International)** – *Award Recipient*, University of Ottawa, 2021–2022
5. **International Admission Scholarship** – *Faculty of Science*, University of Ottawa, 2019–2023

Statement of originality and collaborative contributions

To the best of his knowledge, the author affirms that the research presented in this thesis constitutes original work. The contributions from the author to each of the publications included in this thesis are detailed below.

Chapter 4 contains the paper entitled "Metamaterial-based octave-wide terahertz bandpass filters", which was published in *Photonics Research* in 2023. Ali Maleki performed the FDTD simulations, designed the spectral filters, and coordinated the fabrication of the metasurfaces with Yongbao Xin (Iridian Spectral Technology), who carried out the fabrication. Ali Maleki fabricated the stacked multilayer structures at the University of Ottawa Nanofabrication Facility. Ali Maleki, Avinash Singh, Ahmed Jaber, and Wei Cui prepared the THz setup for measurements. Ali Maleki collected and analyzed the data under the supervision of Jean-Michel Ménard and created the figures for the manuscript.

Chapter 5 contains the paper entitled "Strategies to enhance THz harmonic generation combining multilayered, gated, and metamaterial-based architectures", which was published in *Light: Science & Applications* in 2025. Ali Maleki, Moritz B. Heindl, Georg Herink, and Jean-Michel Ménard conceptualized the idea and designed the experiment. Ali Maleki completed the FDTD simulations for the metasurfaces and coordinated their fabrication with Yongbao Xin, who performed the fabrication. Ali Maleki engineered the gated and non-gated multilayer graphene samples and fabricated the spectral filters. Ali Maleki carried out the measurements with assistance from Moritz B. Heindl. Ali Maleki and Jean-Michel Ménard analyzed the experimental results. Robert W. Boyd, Georg Herink, and Jean-Michel Ménard supervised the project. All authors reviewed and contributed to the published manuscript.

Chapter 6 contains the manuscript entitled *"*Non-perturbative THz nonlinearities in graphene oxide resulting in even and odd harmonics*"*, which has been drafted but is not yet published. Ali Maleki performed the experiments with assistance from Wei Cui. Ilhem Bargaoui prepared the graphene oxide samples. Ali Maleki designed new THz spectral filters for this experiment and coordinated their fabrication with Jean-Michel Guay (Iridian Spectral Technology). Ali Maleki analyzed the data, prepared the figures, and drafted the manuscript with assistance from Hesam Heydarian, under the supervision of Jean-Michel Ménard. Ali Maleki, Jean-Michel Ménard, Lu Wang, and Thomas Brabec developed the theoretical model. Robert W. Boyd, Ksenia Dolgaleva, Thomas Brabec, and Jean-Michel Ménard supervised the experiments and the drafting of the manuscript.

Acknowledgements

Every journey has its quiet heroes, and this PhD has had many. It has been one of the most defining chapters of my life — a time of growth, challenge, and transformation. I am deeply grateful to all those who stood by me, guided me, and helped shape this path. This thesis would not exist without your support, wisdom, and belief in me.

First and foremost, I would like to thank my supervisor, Professor Jean-Michel Ménard, for his unwavering support, mentorship, and encouragement over these years. I have learned so much from you — not only in science and research, but in life. From the very first interview, you believed in me, supported my goals, and gave me the freedom and trust to pursue ambitious ideas. Whether it was performing experiments, attending conferences and workshops, traveling for collaborations, or participating in international summer schools, you consistently opened doors that shaped my growth in countless ways. You encouraged me to explore new directions, introduced me to amazing collaborators, and guided me in drafting papers, grants, and framing ideas. I am especially grateful for your support as I ventured into entrepreneurship and began building my startup alongside my academic work. Even when I had to dedicate time to this pursuit, you remained understanding and fully supportive — something I will always carry with me. I know I will continue to seek your advice in the years to come, and I am truly honored to have had the opportunity to work under your guidance. You were also a great source of emotional support during one of the most difficult times of my life — the passing of my mother. Your compassion during that period meant more to me than I can express.

To my wife, Mahsa Amin Salehi — thank you for being my unwavering source of love and support. From the days before I began this journey to marrying you during the third year of my PhD, you have been by my side through everything. Your patience, resilience, and constant encouragement have sustained me during the hardest and busiest moments. This achievement is as much yours as it is mine.
To my mother — my forever love — your absence is the deepest pain I carry. I wish with all my heart you could be here to see this moment. You were my greatest strength, and your memory lives with me in every step I take. To my father, my three sisters, and my brother — though we have been separated by distance, your love and support have never wavered. Thank you for everything you've sacrificed so I could follow this path.

Among my peers, I owe special thanks to Ahmed Jaber, who began this journey alongside me. From day one, your kindness, generosity, and constant collaboration have been a cornerstone of my experience. We've worked on so many projects together, and your presence always lifted the energy. I would also like to thank

Wei Cui and Nicolas Couture, who guided me when I first joined the THz group. You taught me the fundamentals of our experimental systems, and your mentorship during those early days helped me build a solid foundation. It's been wonderful to see you both succeed in your respective careers.

During the early years of my PhD, I had the pleasure of sharing an office — and many laughs — with Ilhem Bargaoui and Ranjana. Our discussions and fun moments went well beyond science. Even though you've moved on, our friendship has continued, and I'm grateful for that. To the other students and friends I've worked with — Aswin, Subhrojyoti, Eeswar, and others who have since moved on — thank you for the inspiration, collaboration, and camaraderie. A heartfelt thank-you to Hesam, whose help in recent months has been incredibly valuable — from your technical input to our swims and barbeques, I've truly appreciated your presence. To Angela Gamouras, thank you for your consistent support, generous advice, and openness — not only in research, but also in connecting me to opportunities and collaborators.

I am especially thankful to Moritz B. Heindl and Georg Herink from the University of Bayreuth, who hosted me in Germany for collaborative experiments. I was fortunate to receive a Mitacs Globalink Research Award that supported this work, and it a rewarding experience of my PhD. Moritz, your dedication — especially during those long nights in the lab — left a lasting impression.

To Professors Robert Boyd and Ksenia Dolgaleva — it has been an honor to collaborate with you throughout my PhD. Professor Boyd, taking your course and hearing you teach from your renowned textbook on nonlinear optics was a true highlight of my graduate studies.

I would also like to express my appreciation to those who supported my entrepreneurial journey during my PhD. Thank you to the eHub at the University of Ottawa and the Faculty of Science Innovation Office for your encouragement and resources. I was honored to receive the GEEP Award and to be awarded first place in the Desjardins Elevator Pitch Competition, which further motivated me to pursue my innovation goals.

To all the friends — including Hadi, Hossein, Arash, Mina(s), Sadegh, Mahsa(s), Sina — as well as the colleagues and lab members whose names I may not have mentioned, thank you. Whether in the lab, over coffee, or during late-night debugging sessions, your presence made this journey richer and more human.

Finally, to everyone who has been part of this chapter of my life: thank you. The lessons, friendships, and memories from this journey will stay with me — both in science and in life — as I take the next step.

Table of Contents

List of Figures

List of Tables

Chapter 1

Introduction

1.1 Terahertz nonlinear optics

The terahertz (THz) region of the electromagnetic spectrum, typically defined between 0.1 THz and 10 THz, has emerged as a rapidly evolving frontier in science and technology [1]. Situated between the microwave and infrared regions, THz radiation uniquely bridges high-speed electronics and long-wavelength photonics (Fig. 1.1). Historically referred to as the "terahertz gap" due to the absence of efficient sources and detectors, this spectral range has undergone a transformative evolution over the past two decades, driven by breakthroughs in solid-state electronics, optoelectronics, and nonlinear optical techniques [2,3].

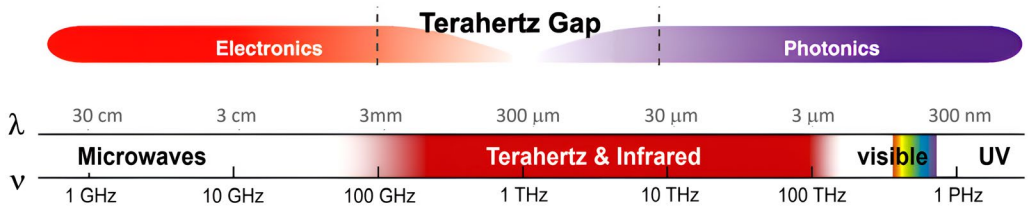

Figure 1.1 Electromagnetic spectrum indicating the terahertz (THz) range between 0.1 and 10 THz, plotted as a function of frequency (ν) and wavelength (λ). This region is commonly referred to as the transitional gap between infrared photonics and microwave electronics.

THz radiation offers several distinctive advantages. Its non-ionizing nature and ability to penetrate many non-metallic and non-polar materials make it ideal for applications in imaging, spectroscopy, communications, and security [4]. Unlike X-rays, THz waves pose minimal health risks while providing comparable penetrative capabilities, enabling non-destructive testing and biomedical imaging [5]. Moreover, THz waves are highly sensitive to molecular vibrations and rotational

transitions, allowing for precise chemical identification—positioning THz spectroscopy as a powerful tool in material science, biochemistry, and pharmaceutical analysis [1,5].

Nonlinear optics in the THz region has emerged as a promising field with diverse scientific and technological applications, including the development of advanced optical devices, imaging systems, and materials characterization platforms [6–8]. The interaction of intense THz fields with nonlinear media enables access to ultrafast carrier and phonon dynamics in solid-state systems [9,10]. One of the key processes in this context is high-harmonic generation (HHG), in which new photons are produced at integer multiples of the incident THz frequency, offering a route to broadband THz-to-optical frequency conversion [11,12]. These phenomena not only deepen our understanding of light–matter interactions under strong fields but also hold potential for ultrafast switching, frequency comb generation, and coherent control of electronic and lattice systems.

Efficient THz generation and detection typically rely on second-order and third-order nonlinear optical processes [13–15]. Optical rectification and difference frequency generation are widely used to produce broadband THz pulses by mixing femtosecond laser pulses in nonlinear crystals [16,17]. The introduction of tilted-pulse-front techniques has further improved phase matching and conversion efficiency, enabling high-field THz generation over wide bandwidths [16,18]. On the detection side, electro-optic sampling—based on the Pockels effect—provides a coherent, phase-resolved method for measuring time-domain THz waveforms with femtosecond resolution [16,19].

Despite substantial progress in THz nonlinear optics, challenges remain in improving efficiency, tunability, and integration of THz systems. Nonlinear generation processes often suffer from low conversion efficiency and stringent phase-matching requirements, while femtosecond laser systems remain costly and complex. Addressing these limitations will require new strategies in material design, device engineering, and nonlinear signal enhancement. These efforts are critical for advancing compact, scalable, and high-performance THz technologies capable of enabling the next generation of ultrafast photonic and electronic systems.

1.2 Metamaterials in THz photonics

Metamaterials—artificial structures composed of subwavelength elements—have emerged as transformative components in THz science [20,21]. Unlike conventional materials, their electromagnetic behavior is determined by geometry rather than composition, enabling control over wave propagation in ways not achievable with natural media [22]. Metamaterials can be engineered to exhibit unusual optical properties such as negative refractive index, near-unity absorption, and custom dispersion characteristics, all of which are critical for THz applications [23,24].

In the THz regime, where conventional materials often suffer from strong losses and limited bandwidth, metamaterials offer a powerful alternative for manipulating THz waves [25,26]. Their resonant elements confine electromagnetic energy to deep subwavelength volumes, leading to strong field localization and enhancement [27,28]. These properties are exploited in a wide range of THz components including lenses, modulators, polarizers, and particularly, spectral filters [29–31]. The ability to tailor the frequency response and polarization state of THz pulses enables precise spectral shaping, vital for both time-domain and frequency-domain spectroscopy [21,32].

One of the key strengths of metamaterials lies in their ability to enhance nonlinear optical effects [33,34]. Nonlinear processes such as HHG, optical rectification, and frequency mixing benefit significantly from the strong local fields and engineered phase-matching conditions that metamaterials provide [35,36]. For example, structures such as split-ring resonators (SRRs) and asymmetric unit cells have been shown to amplify THz fields by orders of magnitude, thus enabling efficient nonlinear conversion even in ultrathin samples [36,37].

This thesis leverages metamaterial architectures to enhance THz nonlinear processes through the design and fabrication of resonant metasurfaces. In particular, octave-wide THz bandpass filters based on bilayer metasurface designs [31] are developed, featuring tailored transmission profiles and sharp spectral roll-offs. To further improve filtering performance, a variety of multilayer spectral filters were designed and implemented throughout different stages of the experiments.

These filters provided strong attenuation outside the target band and high spectral purity of the driving field, which significantly enhanced the detection sensitivity for weak nonlinear signals.

1.3 Graphitic materials for THz nonlinear optics

Graphitic materials—including graphene, and its derivatives—have attracted growing attention in the field of nonlinear optics, particularly in the THz regime [38,39]. These two-dimensional (2D) carbon-based materials exhibit exceptional properties such as high carrier mobility, broadband optical absorption, mechanical flexibility, and strong light–matter interaction [40–43]. Graphene, consisting of a single atomic layer of sp^2-bonded carbon atoms arranged in a honeycomb lattice, possesses a linear band structure near the Dirac point and a zero bandgap, enabling ultrafast electronic and optical responses [44,45]. Its electronic properties are highly tunable through chemical doping, electrostatic gating, or substrate engineering, making it an ideal platform for optoelectronic and photonic devices [45,46].

In the context of THz nonlinear optics, graphene offers unique advantages. Its gapless and linear dispersion enables efficient carrier excitation under intense THz fields, resulting in pronounced nonlinear responses such as saturable absorption, optical Kerr effect, and high-harmonic generation (HHG) [38,47,48]. The ability to dynamically modulate its Fermi level through gating allows for real-time control over its nonlinear optical behavior, facilitating the development of adaptable and high-speed THz modulators and frequency converters [49,50].

Graphene oxide (GO), a chemically modified form of graphene containing oxygen functional groups, introduces additional functionality to the nonlinear optical landscape [51,52]. The presence of these functional groups breaks the lattice symmetry and opens an effective bandgap, which enables both centrosymmetric and non-centrosymmetric optical processes. As a result, GO exhibits enhanced third-order nonlinearities and has shown promising second-order responses such as second-harmonic generation, which are typically forbidden in pristine graphene [53–56]. Moreover, the degree of oxidation and reduction in GO can be tuned to tailor its electronic structure

and nonlinear susceptibility, making it a flexible material for THz applications where both symmetry breaking and high nonlinearity are desired.

Furthermore, the integration of these graphitic materials with THz metamaterials enables the creation of hybrid structures that combine the tunability of 2D systems with the field-enhancing capabilities of engineered resonators [36]. Such hybrid platforms provide a promising route toward compact, reconfigurable, and efficient THz nonlinear devices, and form a central focus of the investigations presented in this thesis.

In summary, the unique combination of strong nonlinearity, broadband tunability, and compatibility with integrated photonic platforms makes graphene and its derivatives compelling candidates for advancing THz nonlinear optics. However, challenges such as symmetry restrictions and strong absorption in pristine graphene motivate the exploration of functionalized variants like GO. The presence of oxygen functional groups not only introduces local symmetry breaking, but also reduces linear absorption, enabling thicker films and stronger nonlinear interaction. Moreover, the solution processability of GO and its compatibility with scalable device fabrication make it a flexible material platform. The following chapters will explore these concepts in greater depth through theoretical modeling, experimental characterization, and device-level implementation.

1.4 Problem statement and research objectives

The field of nonlinear THz optics has advanced significantly in recent years, with landmark studies demonstrating strong-field phenomena such as HHG, saturable absorption, and electrically tunable nonlinear responses in graphene and Dirac materials under intense THz excitation [36,38,49,57]. However, these experiments typically rely on large-scale accelerator-based THz sources, such as the TELBE facility, which can produce high-field, narrowband THz pulses with high repetition rate and excellent signal-to-noise ratio. Despite their exceptional performance, such sources are not readily accessible to the broader research community due to their infrastructural complexity and limited availability.

In contrast, table-top THz sources based on optical rectification are far more accessible and cost-effective, but they present several critical limitations for nonlinear optical experiments. These systems typically generate broadband THz pulses, which are suboptimal for studying frequency-specific nonlinearities like harmonic generation. Moreover, their coherent detection schemes often suffer from background noise and detection bandwidth limitations, complicating the extraction of weak nonlinear signals.

A further challenge lies in the low magnitude of THz-induced nonlinearities in ultrathin 2D materials, which limits their practical applicability in frequency conversion and other nonlinear THz photonic devices. While graphene exhibits strong THz nonlinearity, its high linear absorption imposes restrictions on light–matter interaction length, especially in multilayer configurations. This trade-off motivates the search for alternative or complementary materials that can sustain long interaction lengths while retaining strong nonlinear response.

This thesis addresses the above challenges through the following scientific and technical objectives:

1. To enable THz nonlinear experiments using accessible table-top THz sources by overcoming the limitations of their broadband spectrum and high noise. This is achieved by implementing custom-designed THz spectral filtering strategies, including high-pass and bandpass configurations, to isolate the pump frequency, suppress unwanted spectral components, and reduce background noise.
2. To design and fabricate advanced THz spectral filters based on plasmonic metasurface architectures, enabling strong stopband attenuation, sharp spectral roll-offs, and reproducible performance across a wide THz bandwidth. These filters are integrated before and after the nonlinear sample to optimize the spectral profile of both the pump and the generated signal.
3. To enhance the efficiency of nonlinear THz interactions in 2D materials through a combination of:

- Multilayer stacking to increase the effective interaction length
- Electrostatic gating to dynamically tune the carrier density and nonlinear susceptibility
- Metasurface-enhanced field confinement to locally boost the driving field amplitude

4. To investigate and establish graphene oxide (GO) as a viable alternative platform for nonlinear THz photonics. Unlike graphene, GO exhibits significantly lower linear THz absorption, enabling the use of thicker films and extended interaction volumes. This makes it an attractive material for practical implementation of THz nonlinear devices.

Together, these objectives define a comprehensive strategy for advancing THz nonlinear optics using scalable, accessible, and integrable material platforms and photonic structures.

1.5 Thesis outline

This thesis is organized into seven chapters, each addressing a critical aspect of THz nonlinear optics in graphitic materials:

Chapter 1 introduces the context and motivation for studying nonlinear THz interactions in low-dimensional materials. It provides an overview of the potential of graphitic systems and metamaterials in supporting and enhancing strong-field nonlinear optical phenomena in the THz frequency range.

Chapter 2 presents the theoretical framework underlying nonlinear THz optics. It includes the derivation of the nonlinear wave equation, descriptions of second- and third-order nonlinear polarizations, and mechanisms of optical rectification and tilted-pulse-front THz generation. Key concepts such as saturable absorption, carrier dynamics, and light–matter interaction models for graphene are also covered. Additionally, the chapter discusses the linear and nonlinear optical properties of graphene oxide and its reduced forms, highlighting their unique responses under THz excitation. This chapter forms the basis for interpreting the nonlinear effects studied experimentally in later chapters.

Chapter 3 outlines the experimental methodologies employed throughout the thesis. A high-field THz setup based on optical rectification using the tilted-pulse-front technique is described, including the laser source, nonlinear crystal, and THz beam path configuration. The fabrication of graphitic samples—CVD-grown graphene, multilayer architectures, and graphene oxide—is detailed, as is the design and fabrication of metamaterial-based spectral filters. Device integration steps, such as graphene transfer and gating using polymer electrolytes, are also presented.

Chapter 4 presents the design and implementation of octave-wide THz spectral filters based on bilayer plasmonic metasurfaces, previously published in *Photonics Research* [31]. The chapter includes FDTD simulations, fabrication steps, and experimental characterization of the filters. These devices enable spectral shaping and noise reduction, improving the sensitivity of THz harmonic measurements. Performance metrics such as transmission bandwidth, roll-off steepness, and fabrication repeatability are discussed.

Chapter 5 presents a comprehensive strategy for enhancing third-harmonic generation (THG) in graphene, as reported in *Light: Science & Applications* [47]. Three approaches are systematically explored: multilayer stacking to extend light–matter interaction, electrostatic gating to modulate carrier density, and plasmonic metasurface integration to locally enhance THz fields. These methods result in up to two orders of magnitude enhancement in THG efficiency. Modeling and experimental data reveal how nonlinear response scales with layer count and doping, and a hybrid architecture is proposed to maximize field confinement and tunability.

Chapter 6 investigates the nonlinear optical response of graphene oxide (GO), reduced graphene oxide (rGO), and highly reduced graphene oxide (hrGO) under intense THz excitation. Using a table-top high-field THz system, odd and even-like harmonics up to the 5^{th} order are observed, with even-like harmonic components diminishing as the material transitions from GO to hrGO. The roles of oxygen functional groups, film thickness, and reduction level are systematically explored. Power-dependent transmission measurements reveal a unique saturable absorption behavior in GO,

which is accurately modeled using a phenomenological two-level system. These findings position oxidized graphitic materials as tunable, symmetry-broken platforms for nonlinear THz photonics. Chapter 7 concludes the thesis by summarizing the key scientific contributions and technological innovations developed throughout the work. It highlights the progression from foundational theory and spectral filtering to multi-strategy THG enhancement and the discovery of new nonlinear regimes in functionalized 2D materials. The chapter also outlines future directions, including the integration of 2D materials with electronic THz sources, the exploration of new nonlinear processes in the THz regime, and the development of chip-scale, reconfigurable nonlinear photonic devices enabled by hybrid graphitic–metamaterial platforms.

Chapter 2

Theory

2.1 Fundamentals of THz nonlinear optics

Nonlinear optics explores the behavior of materials exposed to high-intensity electromagnetic fields, where the response of the medium becomes nonlinear with respect to the electric field. In the THz frequency regime, nonlinear phenomena such as high-harmonic generation (HHG), optical rectification, and nonlinear absorption are crucial to the generation, manipulation, and detection of THz waves. At low field intensities, the material response is governed by a linear relationship between the induced polarization $\tilde{P}(t)$ (dipole moment per unit volume) and the applied electric field $\tilde{E}(t)$, described by [12]:

$$\tilde{P}(t) = \varepsilon_0 \chi^{(1)} \tilde{E}(t), \tag{2.1.1}$$

Here, $\chi^{(1)}$ is the linear susceptibility of the medium and ε_0 is the vacuum permittivity. The tilde (~) denotes rapidly varying quantities in time. However, under intense excitation—such as with ultrafast or high-field THz pulses—the polarization becomes nonlinear, requiring higher-order contributions to be included. In such cases, the total polarization is expressed as a power series in the electric field:

$$\tilde{P}(t) = \varepsilon_0 \left[\chi^{(1)} \tilde{E}(t) + \chi^{(2)} \tilde{E}^2(t) + \chi^{(3)} \tilde{E}^3(t) + \cdots \right] \tag{2.1.2}$$

Each term in this expansion corresponds to a distinct order of material response:

- The first-order term, $\tilde{P}^{(1)}(t) = \varepsilon_0 \chi^{(1)} \tilde{E}(t),$ describes linear optical effects such as refraction and absorption.

- The second-order term, $\tilde{P}^{(2)}(t) = \varepsilon_0 \chi^{(2)} \tilde{E}^2(t)$, gives rise to second-order nonlinear processes, including second-harmonic generation (SHG), sum-frequency generation (SFG), difference-frequency generation (DFG), and optical rectification (OR). These effects can only occur in non-centrosymmetric media, meaning materials whose structure is not invariant under inversion through a point (i.e., they lack inversion symmetry), which allows second-order nonlinear responses.
- The third-order polarization $\tilde{P}^{(3)}(t) = \varepsilon_0 \chi^{(3)} \tilde{E}^3(t)$, governs phenomena such as third-harmonic generation (THG), the Kerr effect, self-phase modulation (SPM), and saturable absorption. Unlike second-order processes, third-order nonlinearity is present in all materials, including centrosymmetric materials like monolayer graphene.

The nonlinear susceptibilities $\chi^{(n)}$ are complex, frequency-dependent tensor quantities that depend on the electronic structure, crystal symmetry, and external conditions such as doping, temperature, or applied electric fields [12]. These nonlinear responses generate new frequency components do not present in the driving field and can significantly alter the spectral and temporal characteristics of propagating optical pulses.

In the THz regime (0.1 to 10 THz)—where photon energies typically lie between 0.4 and 40 meV—unique physical mechanisms emerge. These include intraband carrier dynamics, strong-field-driven transitions, carrier heating, and field-induced symmetry breaking [48]. This section establishes the theoretical foundation needed to understand such phenomena. The following subsections derive the nonlinear wave equation and describe how second- and third-order effects manifest in harmonic generation, especially in two-dimensional materials such as graphene.

2.1.1 Derivation of the nonlinear wave equation

To understand how nonlinear optical effects emerge and propagate in a medium, we begin with macroscopic Maxwell's equations in a non-magnetic medium [12]:

$$
\begin{aligned}
\nabla \times \vec{E}(\vec{r},t) &= -\frac{\partial \vec{B}(\vec{r},t)}{\partial t} && \text{(Faraday's law)} \\
\nabla \times \vec{H}(\vec{r},t) &= \vec{J}_f(\vec{r},t) + \frac{\partial \vec{D}(\vec{r},t)}{\partial t} && \text{(Ampere-Maxwell law)} \\
\nabla \cdot \vec{B}(\vec{r},t) &= 0 && \text{(Gauss's law for magnetism)} \\
\nabla \cdot \vec{D}(\vec{r},t) &= \rho_f(\vec{r},t) && \text{(Gauss's law)}
\end{aligned}
\tag{2.1.3}
$$

Where $\rho_f(\vec{r},t)$ represents the free charge density, and $\vec{J}_f(\vec{r},t)$ denotes the free current density. In the absence of free charges and currents ($\rho_f(\vec{r},t)=0$ and $\vec{J}_f(\vec{r},t)=0$), the medium's neutrality ensures that the fields can induce polarization, defined through the constitutive relations:

$$
\begin{aligned}
\vec{D}(\vec{r},t) &= \varepsilon_0 \vec{E}(\vec{r},t) + \vec{P}(\vec{r},t) \\
\vec{B}(\vec{r},t) &= \mu_0 \vec{H}(\vec{r},t)
\end{aligned}
\tag{2.1.4}
$$

Here, ε_0 and μ_0 denote the permittivity and permeability of free space, respectively. To derive wave equations, we start with Farady's law and take the curl of both sides:

$$
\nabla \times (\nabla \times \vec{E}(\vec{r},t)) = -\frac{\partial}{\partial t}(\nabla \times \vec{B}(\vec{r},t)) \tag{2.1.5}
$$

Using constitutive relation ($\vec{B}(\vec{r},t) = \mu_0 \vec{H}(\vec{r},t)$) and substituting Ampère–Maxwell law ($\nabla \times \vec{B} = \mu_0 \vec{J} + \mu_0 \frac{\partial \vec{D}}{\partial t}$) in dielectric ($\vec{J}=0$) into Eq. 2.1.5 we get:

$$
\nabla \times \left(\nabla \times \vec{E}(\vec{r},t) \right) = -\mu_0 \frac{\partial^2 \vec{D}(\vec{r},t)}{\partial t^2} \tag{2.1.6}
$$

Expanding $\vec{D}(\vec{r},t)$ using its constitutive relation (Eq. 2.1.4) and polarization into its linear $\vec{P}^{(1)}$ and nonlinear $\vec{P}^{NL}$ components, we write:

$$
\vec{D}(\vec{r},t) = \varepsilon_0 \vec{E}(\vec{r},t) + \vec{P}^{(1)}(\vec{r},t) + \vec{P}^{\mathrm{NL}}(\vec{r},t) \tag{2.1.7}
$$

The left-hand side of Eq. 2.1.6 simplifies using the vector identity:

$$
\nabla \times \left(\nabla \times \vec{E}(\vec{r},t) \right) = \nabla \left(\nabla \cdot \vec{E}(\vec{r},t) \right) - \nabla^2 \vec{E}(\vec{r},t) \approx -\nabla^2 \vec{E}(\vec{r},t) \tag{2.1.8}
$$

The resulting nonlinear optical wave equation becomes:

$$\nabla^2 \vec{E}(\vec{r},t) = \frac{1}{c^2}\frac{\partial^2}{\partial t^2}\left(\vec{E}(\vec{r},t) + \frac{1}{\varepsilon_0}\left(\vec{P}^{(1)}(\vec{r},t) + \vec{P}^{\mathrm{NL}}(\vec{r},t) \right) \right) \tag{2.1.9}$$

Noting the $\mu_0\varepsilon_0 = 1/c^2$, where c is the speed of light in vacuum, the contribution in nonlinear media leads to:

$$\nabla^2 \vec{E}(\vec{r},t) - \frac{1}{\epsilon_0 c^2}\frac{\partial^2}{\partial t^2}\vec{D}(\vec{r},t) = -\frac{1}{\varepsilon_0 c^2}\frac{\partial^2}{\partial t^2}\vec{P}^{\mathrm{NL}}(\vec{r},t) \tag{2.1.10}$$

For the case of a lossless, dispersionless medium, the displacement relation reduces a simple form

$$\vec{D}(t) = \varepsilon_0 \varepsilon^{(1)} \cdot \vec{E}(t) \tag{2.1.11}$$

Where $\varepsilon^{(1)}$ is the frequency-independent dielectric tensor. While in the case of a dispersive medium, each frequency component of the field should be considered. To analyze the nonlinear response in this medium, the electric field and polarization can be decomposed into their frequency components:

$$\vec{E}(\vec{r},t) = \sum_n \vec{E}_n(\vec{r}) e^{-i\omega_n t} + \text{c.c.}, \tag{2.1.12}$$

$$\vec{P}^{\mathrm{NL}}(\vec{r},t) = \sum_n \vec{P}_n^{\mathrm{NL}}(\vec{r}) e^{-i\omega_n t} + \text{c.c.}, \tag{2.1.13}$$

c.c. is the complex conjugate term. By considering the general form of dissipative medium, the dielectric tensor $\varepsilon^{(1)}$ will be a complex quantity. Substituting these expressions into Eq. 2.1.10 results in the wave equation in the frequency domain:

$$\nabla^2 \vec{E}_n(\vec{r}) + \frac{\omega_n^2 \varepsilon^{(1)}(\omega_n)}{c^2} \cdot \vec{E}_n(\vec{r}) = -\frac{\omega_n^2}{\epsilon_0 c^2}\vec{P}_n^{\mathrm{NL}}(\vec{r}) \tag{2.1.14}$$

This equation, often referred to as the nonlinear Helmholtz equation, forms the basis for understanding wave propagation and frequency generation in nonlinear optical media. It highlights that nonlinear polarization functions as a source term that radiates new frequency components. In centrosymmetric materials such as pristine monolayer graphene, the second-order susceptibility $\chi^{(2)}$

vanishes under the electric-dipole approximation, making third-order effects governed by $\chi^{(3)}$ the dominant mechanism—most notably THG. In contrast, materials like graphene oxide, which exhibit local inversion symmetry breaking due to chemical functionalization, can support both even- and odd-harmonic generation. These nonlinear phenomena are further explored through theoretical modeling and experimental investigations in later chapters.

2.1.2 Second-order nonlinear polarization

To analyze second order nonlinear interactions involving two distinct frequencies ω_1 and ω_2, we consider an electric field of the form:

$$\tilde{E}(\vec{r},t) = \vec{E}_1(\vec{r})e^{-i\omega_1 t} + \vec{E}_2(\vec{r})e^{-i\omega_2 t} + \text{c.c.} \tag{2.1.15}$$

The nonlinear polarization at second order, as dictated by the susceptibility tensor $\chi^{(2)}$ can be written:

$$\tilde{P}_i^{(2)}(\vec{r},t) = \varepsilon_0 \sum_{jk} \chi_{ijk}^{(2)} \vec{E}_j(\vec{r},t)\vec{E}_k(\vec{r},t) \tag{2.1.16}$$

Substituting the electric field and expanding the product $\vec{E}_j(\omega_1)\vec{E}_k(\omega_2)$, we obtain several nonlinear polarization components corresponding to different physical processes. In what follows, we denote ω_3 as the frequency of the generated nonlinear polarization term, which results from the interaction of two input frequencies ω_1 and ω_2 . The exact form of ω_3 depends on the specific nonlinear process under consideration as detailed below:

1. Second-harmonic generation (SHG):

$$P_i^{(2)}(2\omega) = \varepsilon_0 \sum_{jk} \chi_{ijk}^{(2)}(2\omega;\omega,\omega)E_j(\omega)E_k(\omega) \tag{2.1.17}$$

Where $\omega_1 = \omega_2 = \omega \Rightarrow \omega_3 = 2\omega$. This term represents the basis for SHG, where two photons at the same frequency (ω) combine to produce a single photon at twice the frequency (2ω).

2. Sum-Frequency Generation (SFG):

$$P_i^{(2)}(\omega_1+\omega_2)=\varepsilon_0\sum_{jk}\chi_{ijk}^{(2)}(\omega_1+\omega_2;\omega_1,\omega_2)E_j(\omega_1)E_k(\omega_2) \tag{2.1.18}$$

Here, $\omega_3=\omega_1+\omega_2$. This term describes the generation of a photon whose frequency is the sum of two distinct input frequencies.

3. Difference-Frequency Generation (DFG):

$$P_i^{(2)}(|\omega_1-\omega_2|)=\varepsilon_0\sum_{jk}\chi_{ijk}^{(2)}(|\omega_1-\omega_2|;\omega_1,-\omega_2)E_j(\omega_1)E_k^*(\omega_2) \tag{2.1.19}$$

Where $\omega_3=|\omega_1-\omega_2|$. This term represents difference-frequency generation, where the resulting photon has a frequency equal to the difference between the two input frequencies. When $\omega_1=\omega_2$, the DFG process results in a DC polarization component, which gives rise to optical rectification, crucial for THz generation.

Figure 2.1 schematically illustrates the main second-order nonlinear processes: SHG, SFG, and DFG, along with their energy-level diagrams.

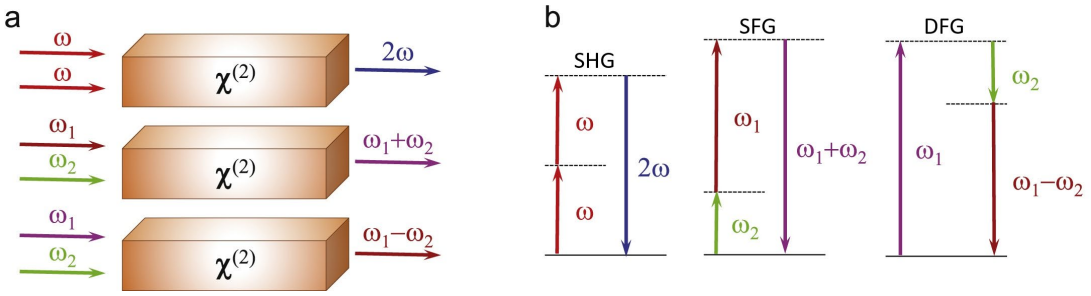

Figure 2.1 Second-order nonlinear processes in a $\chi^{(2)}$ medium. **a** Physical depiction of second-harmonic generation (SHG), sum-frequency generation (SFG), and difference-frequency generation (DFG) resulting from interaction of optical fields with a $\chi^{(2)}$ material. **b** Energy-level diagrams illustrating photon conversion pathways: SHG arises from two photons at ω; SFG from $\omega_1+\omega_2$; and DFG (or optical rectification when $\omega_1=\omega_2$) yields an output at $\omega_1-\omega_2$. Figure adapted from [58].

2.1.2.1 Terahertz generation via optical rectification

Optical rectification (OR) is a second-order nonlinear optical process responsible for the generation of low-frequency electromagnetic waves when an intense ultrafast near-infrared (NIR) pulse

interacts with a $\chi^{(2)}$ nonlinear medium. The underlying mechanism is DFG, where various frequency components within the broadband spectrum of a single femtosecond pulse mix to produce a new component in the THz range (see Fig. 2.2).

Starting from the second-order nonlinear polarization associated with DFG (see Eq. (2.1.19)), we consider only the components that contribute to THz emission oscillating at frequency $\Omega = \omega_1 - \omega_2$. By substituting this polarization into the nonlinear wave equation (Eq. (2.1.14)), we obtain the wave equation governing THz generation via OR:

$$\nabla^2 \vec{E}_\Omega(\vec{r}) + \frac{\Omega^2 \varepsilon_r(\Omega)}{c^2} \cdot \vec{E}_\Omega(\vec{r}) = -\frac{\Omega^2}{\varepsilon_0 c^2} \vec{P}_\Omega^{(2)}(\vec{r}) \tag{2.1.20}$$

Assuming the THz field propagates along the z-axis and is time-harmonic, we express the electric field as:

$$\vec{E}_\Omega(z) = \vec{A}_\Omega(z) e^{i(k_\Omega z - \Omega t)} + c.c. \tag{2.1.21}$$

where $k_\Omega = \frac{n_\Omega \Omega}{c}, n_\Omega^2 = \varepsilon^{(1)}(\Omega)$. We plug it into Eq. 2.1.20. To simplify the second derivative term, we apply the slowly varying envelope approximation**.** This approximation assumes that the spatial variation of the envelope $\vec{A}_\Omega(z)$ is much slower than the oscillation due to the carrier wave, i.e.,

$$\left| \frac{d^2 \vec{A}_\Omega}{dz^2} \right| \ll \left| k_\Omega \frac{d\vec{A}_\Omega}{dz} \right| \tag{2.1.22}$$

Under this condition, the second derivative of the total field becomes:

$$\frac{d^2 \vec{E}_\Omega}{dz^2} + k_\Omega^2 \vec{E}_\Omega \approx 2ik_\Omega \frac{d\vec{A}_\Omega}{dz} e^{i(k_\Omega z - \Omega t)} \tag{2.1.23}$$

Substituting Eq. 2.1.23 into Eq. 2.1.20, we get:

$$\frac{d\vec{A}_\Omega}{dz} = \frac{i\Omega^2}{2k_\Omega c^2 \varepsilon_0} \vec{P}_\Omega^{(2)}(z) e^{i\Delta k z} \tag{2.1.24}$$

Where $\Delta k = k(\omega_1) - k(\omega_2) - k_\Omega$. This equation illustrates how the amplitude of the THz field evolves along the nonlinear medium. Integration over the crystal length L yields:

$$\vec{A}_\Omega(L) = \frac{i\Omega^2}{2k_\Omega c^2 \varepsilon_0} \int_0^L \vec{P}_\Omega^{(2)}(z) e^{i\Delta k z} dz \tag{2.1.25}$$

Assuming constant $\vec{P}_\Omega^{(2)}$ over the interaction length, this evaluates to:

$$\vec{A}_\Omega(L) = \frac{i\Omega^2 \vec{P}_\Omega^{(2)}}{2k_\Omega c^2 \varepsilon_0} \cdot \frac{e^{i\Delta k L} - 1}{i\Delta k} = \frac{\Omega^2 \vec{P}_\Omega^{(2)}}{2k_\Omega c^2 \varepsilon_0} \cdot \mathrm{sinc}\left(\frac{\Delta k L}{2}\right) e^{i\frac{\Delta k L}{2}} \tag{2.1.26}$$

The intensity of the generated THz field becomes:

$$I_\Omega \propto |\vec{A}_\Omega(L)|^2 \propto L^2 \mathrm{sinc}^2\left(\frac{\Delta k L}{2}\right) \tag{2.1.27}$$

This equation shows that the generation efficiency is maximized when $\Delta k = 0$, leading to the condition for perfect phase matching.

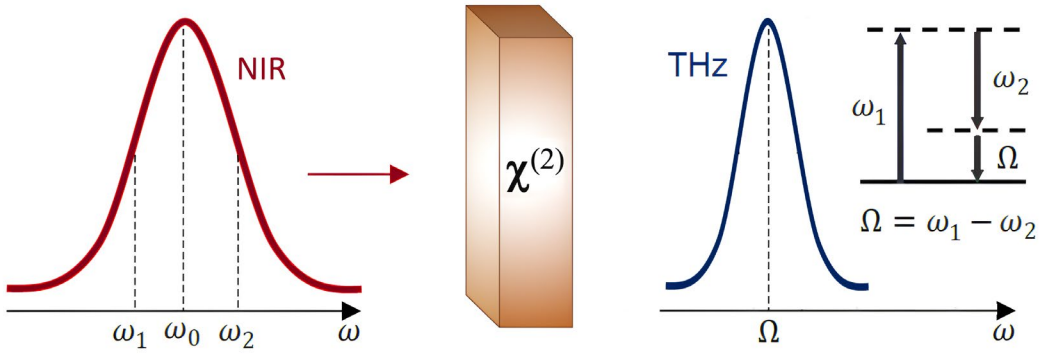

Figure 2.2 Schematic representation of THz generation through optical rectification, along with the corresponding energy-level diagram in a $\chi^{(2)}$ nonlinear medium.

2.1.2.2 Phase-matching condition

Phase matching plays a critical role in all nonlinear frequency conversion processes, including SFG, DFG, HHG, and THz generation via optical rectification. Efficient frequency conversion relies on the constructive interference of the newly generated waves as they propagate through the nonlinear medium. This constructive interference is only sustained when the generated field at each point

remains in phase with that generated at other points—a condition quantified by the phase mismatch Δk. When $\Delta k \neq 0$, destructive interference limits the effective interaction length, thereby reducing conversion efficiency. Minimizing Δk or ideally achieving $\Delta k = 0$, is therefore essential for maximizing the output in any nonlinear process [12].

In the context of optical rectification using a broadband ultrafast pulse, the generation occurs through difference-frequency generation, where $\omega_1 = \omega_0 + \delta\omega$ and $\omega_2 = \omega_0 - \delta\omega$, such that, $\Omega = \omega_1 - \omega_2 = 2\delta\omega$. Expanding the wavevectors using a Taylor series around the central frequency ω_0, we write:

$$k(\omega_1) \approx k(\omega_0) + \delta\omega\left(\frac{dk}{d\omega}\Big|_{\omega_0}\right) \tag{2.1.28}$$

$$k(\omega_2) \approx k(\omega_0) - \delta\omega\left(\frac{dk}{d\omega}\Big|_{\omega_0}\right) \tag{2.1.29}$$

Adding and subtracting, we find:

$$k(\omega_1) - k(\omega_2) = 2\delta\omega\left(\frac{dk}{d\omega}\Big|_{\omega_0}\right) = \Omega\left(\frac{dk}{d\omega}\Big|_{\omega_0}\right) \tag{2.1.30}$$

Substituting into $\Delta k = k(\omega_1) - k(\omega_2) - k_\Omega$

$$\Delta k \approx \Omega\left(\frac{dk}{d\omega}\Big|_{\omega_0} - \frac{1}{v_p(\Omega)}\right) \tag{2.1.31}$$

Using the definition $\frac{dk}{d\omega} = \frac{1}{v_g(\omega_0)}$, where v_g is the group velocity of the NIR pulse, and $v_p(\Omega) = \frac{c}{n(\Omega)}$ is the phase velocity of the THz wave, we obtain the phase-matching condition:

$$\frac{1}{v_g(\omega_0)} = \frac{1}{v_p(\Omega)} \quad \Rightarrow \quad n_g(\omega_0) = n(\Omega) \tag{2.1.32}$$

This result shows that efficient THz generation through optical rectification requires the group index of the NIR pulse to match the phase index of the THz radiation.

2.1.2.3 Tilted pulse front technique

In most nonlinear crystals used for THz generation, natural phase matching is not achieved because the group index of the NIR pulse ($n_g(\omega_0)$) does not match the refractive index of the THz wave ($n(\Omega)$). To overcome this, the tilted pulse front (TPF) technique [16,18] is employed to artificially control the projection of the group velocity along the THz propagation axis. The idea behind this method is to tilt the intensity front of the NIR pulse at an angle γ with respect to the phase front. This tilt modifies the axial component of the group velocity to match the phase velocity of the THz field (see Fig. 2.3a):

$$\cos(\gamma) = \frac{v_{THz}}{v_{NIR}} \tag{2.1.33}$$

Thus, the required pulse front tilt angle is:

$$\gamma = \cos^{-1}\left(\frac{n_g(\omega_{NIR})}{n_p(\Omega)}\right) \tag{2.1.34}$$

This tilt is typically introduced by using a diffraction grating, which imparts angular dispersion to the NIR pulse. An imaging system (such as a lens pair or cylindrical telescope) is then used to project this angular dispersion onto the nonlinear crystal with minimal distortion and precise magnification.

Figure 2.3b shows a schematic of the tilted pulse front configuration applied to a $LiNbO_3$ crystal for THz generation. In the configuration, a diffraction grating introduces angular dispersion to a femtosecond NIR pump pulse with finite spatial width. Each point across the beam footprint on the grating is diffracted at a wavelength-dependent angle, corresponding to the spectral components $\lambda_0 \pm \Delta\lambda$. This angular dispersion results in a tilted pulse front, where different parts of the beam arrive at different positions across the transverse profile. The first cylindrical lens (L1), placed one focal length (f_1) from the grating, causes the dispersed rays to begin converging. The second cylindrical lens (L2), placed a distance $2f_1+f_2$ from the grating, reconstructs a real image of the grating — and thus the tilted intensity front — at its back focal plane. Only at this plane all spectral components

of NIR beam spatially recombine to form a well-focused beam with the designed tilt angle. The $LiNbO_3$ crystal is positioned at this exact location to receive the fully reconstructed tilted pulse front, ensuring optimal phase matching between the pump and THz waves. Misplacing the crystal from this plane results in a distorted beam geometry and reduced THz generation efficiency.

The tilted pulse front technique can be conceptually linked to Cherenkov radiation [59,60], where a wave is emitted at a characteristic angle due to a velocity mismatch. In the context of THz generation, when the group velocity of the NIR pulse exceeds the phase velocity of the THz wave, the emission occurs at the so-called Cherenkov angle θ_C. In the tilted pulse front scheme, this emission angle is geometrically imposed by the tilt angle γ, such that $\theta_C=\gamma$. This correspondence provides a useful physical interpretation: the THz wave is emitted normal to the tilted intensity front, just as in Cherenkov-like phase matching.

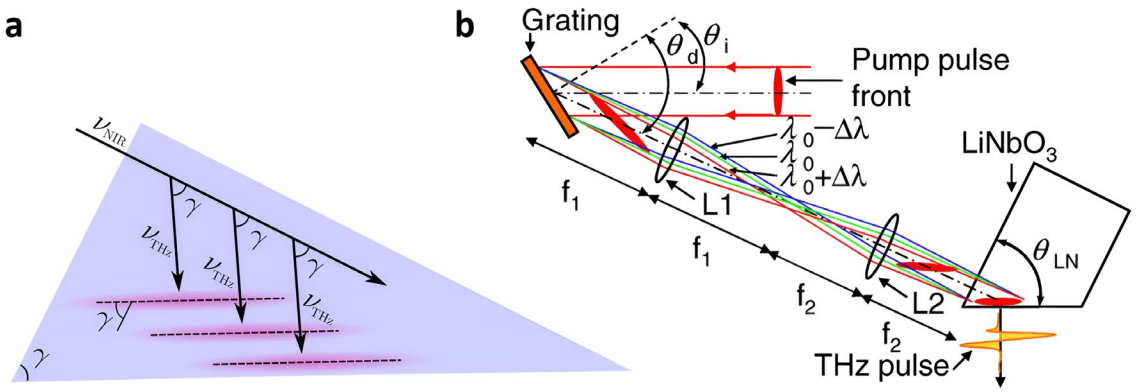

Figure 2.3 Schematic representation of tilted pulse front technique for THz generation. **a** The NIR pump pulse propagates into the nonlinear crystal, while the pulse front is tilted by an angle γ. This configuration ensures that the intensity fronts (dashed lines) intersect the THz emission direction at the correct phase-matching geometry. Efficient THz generation requires the axial projection of the NIR group velocity to match the THz phase velocity: $v_{NIR}\cos(\gamma)=v_{THz}$ **b** Ray optics construction of the pulse front tilt based on the grating geometry. The setup includes a diffraction grating and two cylindrical lenses (L1 and L2) arranged in a 4f configuration with focal lengths f_1 and f_2, respectively. The grating introduces angular dispersion to the femtosecond pump pulse, creating a tilted pulse front. The 4f-lens system images this tilted pulse front onto the $LiNbO_3$ crystal at an optimized angle $\theta_{LN}=\gamma$, matched to the phase velocity of THz waves. Efficient THz

generation via optical rectification is achieved when the image of them is precisely formed at the crystal surface, which is placed at the focal plane of lens L2. Figure adapted from [61,62].

2.1.3 Third-order nonlinear polarization

While second-order nonlinear effects require a non-centrosymmetric medium, third-order processes are allowed in all materials and become particularly important in centrosymmetric media such as graphene. The third-order nonlinear polarization arises from the third-order susceptibility tensor and is responsible for phenomena such as third-harmonic generation (THG), four-wave mixing (FWM), and saturable absorption. The third-order nonlinear polarization vector is expressed as [12]:

$$P_i^{(3)}(\omega_m) = \varepsilon_0 \sum_{jkl} \sum_{\omega_n,\omega_p,\omega_q} \chi_{ijkl}^{(3)}(\omega_m;\omega_n,\omega_p,\omega_q) E_j(\omega_n) E_k(\omega_p) E_l(\omega_q) \tag{2.1.35}$$

For THG, where three photons of frequency combine to generate one photon at 3ω, the polarization reduces to:

$$P_i^{(3)}(3\omega) = \varepsilon_0 \sum_{jkl} \chi_{ijkl}^{(3)}(3\omega;\omega,\omega,\omega) E_j(\omega) E_k(\omega) E_l(\omega) \tag{2.1.36}$$

In isotropic or scalar approximations (assuming polarization components are aligned), this becomes:

$$\vec{P}^{(3)}(3\omega) = \varepsilon_0 \chi^{(3)}(3\omega;\omega,\omega,\omega) \vec{E}(\omega)^3 \tag{2.1.37}$$

This polarization serves as the source term in the wave equation at frequency 3ω, leading to THG emission. For higher-order odd harmonics (e.g., 5th, 7th, etc.), the generalized form of the nonlinear polarization is:

$$P_i^{(n)}(n\omega) = \varepsilon_0 \sum_{j_1 j_2 \cdots j_n} \chi_{ij_1 j_2 \ldots j_n}^{(n)} E_{j_1}(\omega) E_{j_2}(\omega) \ldots E_{j_n}(\omega) \tag{2.1.38}$$

and the generated harmonic field scales as:

$$\vec{E}(n\omega) \propto \chi^{(n)} \vec{E}^n(\omega) \tag{2.1.39}$$

As a concrete example, in the work by Hafez et al. (*Nature* 2018) [38], the nonlinear response of monolayer graphene under strong-field THz excitation was studied, and effective values of the nonlinear susceptibilities were extracted:

$$\chi^{(3)} \approx 10^{-9}\, m^2 / V^2$$
$$\chi^{(5)} \approx 10^{-22}\, m^4 / V^4$$
$$\chi^{(7)} \approx 10^{-38}\, m^6 / V^6$$

These remarkably large nonlinearities are attributed to the massless Dirac fermion dispersion of graphene and the absence of an energy gap, which enable efficient generation of high-order harmonics even at low photon energies in the THz regime. These results provide valuable insight into the ultrafast and highly nonlinear optical behavior of graphene, motivating its use in THz photonic applications and strong-field light–matter interaction studies.

2.1.3.1 Saturable absorption and two-level system dynamics

Saturable absorption is a nonlinear optical phenomenon in which a material's absorption decreases with increasing light intensity. This effect is commonly used in passive mode-locking and optical switching. In the frequency-domain picture, saturable absorption is directly associated with the imaginary part of the third-order nonlinear susceptibility, $\mathrm{Im}[\chi^{(3)}]$, which governs intensity-dependent absorption. For materials exhibiting two-photon absorption, the imaginary part of $\chi^{(3)}$ is positive ($\mathrm{Im}[\chi^{(3)}]>0$); resulting in increased absorption as intensities increase. In contrast, for saturable absorbers, $\mathrm{Im}[\chi^{(3)}]<0$, indicating a decrease in absorption as intensity increases.

A phenomenological model of nonlinear absorption expands the absorption coefficient as a function of optical intensity [12]:

$$\alpha(I) = \alpha_0 + \beta I \tag{2.1.40}$$

Where α_0 is the linear absorption coefficient, and β is a nonlinear absorption coefficient. This expression captures weakly nonlinear behavior but does not account for full saturation. A more accurate model, particularly under strong excitation, is given by [12]:

$$\alpha(I) = \frac{\alpha_0}{1 + I / I_{\text{sat}}} \tag{2.1.41}$$

where I_{sat} is the saturation intensity, defined as the intensity at which the absorption drops to half its low-intensity value. From the density matrix formalism, the absorption is governed by the imaginary part of the coherence term ρ_{01}, which in turn leads to the polarization $\vec{P} = N\varepsilon_0 \vec{\chi} \vec{E}$. Where N is the number density of atoms, and ε_0 is the vacuum permittivity. In general, the electric susceptibility $\vec{\chi}$ is a second-rank tensor that relates the macroscopic polarization to the electric field. In the context of the two-level atom model, the polarization is microscopically governed by the ρ_{10} of the density matrix and the transition dipole moment $\vec{r}_{01}$, leading to the expression:

$$\vec{P} \propto \rho_{10} \vec{r}_{01} \tag{2.1.42}$$

Solving the steady-state two-level equations gives an expression for $\text{Im}[\chi]$ of the form [12]:

$$\text{Im}[\chi] \propto \frac{1}{\Delta^2 + \left(\frac{1}{T_2}\right)^2 + \Omega^2 T_1 / T_2} \tag{2.1.43}$$

where Δ is the detuning, T_1 and T_2 are the population decay and dephasing times, respectively, and Ω is the Rabi frequency, which is proportional to the electric field amplitude $\left|\vec{E}\right|$. This model shows how the absorption decreases with increasing field strength due to saturation of population inversion.

2.2 Metamaterials

2.2.1 Metamaterials and metasurfaces in the THz regime

Metamaterials are artificially structured media designed to exhibit tailored electromagnetic responses arising from their geometry rather than intrinsic chemical composition [63]. By engineering the arrangement of subwavelength building blocks—known as meta-atoms—metamaterials enable effective control over the electric permittivity $\varepsilon(\omega)$ and magnetic permeability $\mu(\omega)$, leading to a broad range of exotic optical phenomena. These include negative refractive index $n(\omega)$, near-zero index behavior, and superlensing [64]. The refractive index of a medium is related to these parameters through:

$$n(\omega) = \sqrt{(\varepsilon(\omega)\mu(\omega))} \tag{2.2.1}$$

When either $\varepsilon(\omega)$ or $\mu(\omega)$ becomes negative, the medium can exhibit unusual dispersion, backward wave propagation, and reversed Snell's law, as first proposed by Veselago in 1968 [65]. The first experimental demonstration of a negative-index metamaterial was achieved in 2000 by Smith et al. using split-ring resonators and wire structures at microwave frequencies [66].

A traditional metamaterial is generally a three-dimensional (3D) structure composed of volumetric arrangements of resonant unit cells that collectively shape the bulk electromagnetic response. In contrast, metasurfaces are two-dimensional (2D) analogs of metamaterials composed of planar arrays of resonant elements. While metamaterials affect the propagation of waves throughout a volume, metasurfaces impose phase, amplitude, or polarization transformations at an interface. Metasurfaces provide several advantages, including reduced thickness, ease of fabrication, and lower losses due to their minimal interaction volume [63].

Plasmonic metasurfaces are engineered structures composed of high-conductivity metals designed to support strong field localization through geometry-induced resonances, such as in wire grids, split-ring resonators, or slot arrays [37,67,68]. While they mimic plasmonic behavior, especially at THz frequencies, the underlying mechanism relies on current-driven resonances rather than true

plasmon modes [26,69]. Their effectiveness in the THz regime is amplified by the low loss of metals in this frequency range—where interband transitions are negligible and metals behave nearly as perfect conductors. Additionally, because many natural materials lack resonant responses in this band, these structures enable enhanced spectral selectivity, efficient polarization control, and tunable filtering using compact and integrable device geometries [21,70].

Metasurfaces, are especially advantageous for THz applications due to their ultrathin form factor and compatibility with standard microfabrication techniques. These 2D metastructures can manipulate the phase, amplitude, and polarization of transmitted or reflected THz waves through precisely patterned subwavelength elements [26,31]. Unlike conventional multilayer dielectric filters that depend on Fabry–Pérot interference, metasurfaces achieve spectral control through resonant surface currents in a single patterned layer, providing compact and efficient alternatives for spectral filtering and beam shaping [21,70].

2.2.2 Surface plasmon polaritons

The interaction of electromagnetic waves with metals at subwavelength scales leads to the emergence of surface plasmons—collective charge oscillations at the interface between a metal and a dielectric. The optical response of metals in this regime is governed primarily by their free electron gas behavior, which is well described by the Drude model [64]:

$$\varepsilon(\omega) = \varepsilon_{\infty} - \frac{\omega_p^2}{\omega^2 + i\gamma\omega} \tag{2.2.2}$$

Where $\omega_p = \sqrt{\frac{Ne^2}{\varepsilon_0 m^*}}$ is the plasma frequency, m^* is the effective mass of the electron, γ is the damping rate due to electron scattering, and ε_{∞} accounts for contributions from bound electrons and interband transitions, representing the high-frequency limit of the material's dielectric response. This leads to a complex dielectric function, allowing surface-bound modes called surface plasmon polaritons (SPPs) to exist at the metal–dielectric interface. SPPs are evanescent transverse

magnetic waves that propagate along the interface and decay exponentially perpendicular to it. these modes are supported when the real part of the metal's permittivity satisfies $\mathrm{Re}[\varepsilon_2] < -\varepsilon_1$, where ε_1 is the permittivity of the dielectric. The dispersion relation for SPPs at a flat metal–dielectric interface is given by [64]:

$$k_{SP} = k_0 \sqrt{\frac{\varepsilon_1 \varepsilon_2}{\varepsilon_1 + \varepsilon_2}} \tag{2.2.3}$$

Where $k_0 = \omega / c$ is the free-space wavevector. The field profile associated with this dispersion relation is characterized by exponential decay into both media, resulting in tight confinement near the interface and enhanced light–matter interaction. This is illustrated schematically in Fig. 2.4.

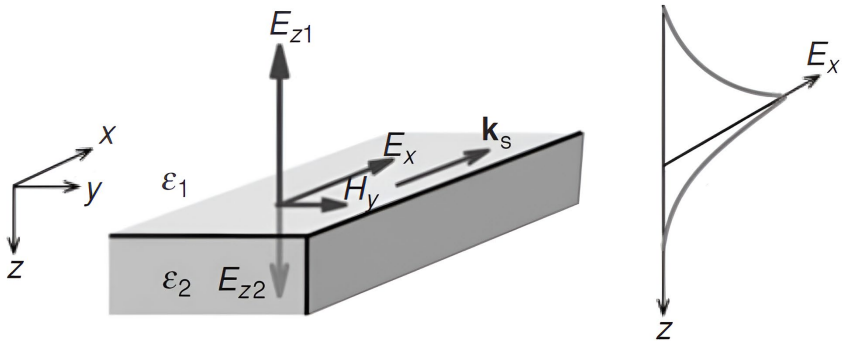

Figure 2.4 Schematic for the illustration of the interface between two media characterized by dielectric functions ε_1 and ε_2, where the x-component of the electric field E_x exhibits exponential decay in both directions along the z-axis from the interface at $z=0$. The wave vector k_s corresponds to the propagation of the surface plasmon polariton along the interface. The field is strongly localized near the interface, making SPPs ideal for enhancing light-matter interactions. Figure adapted from [64].

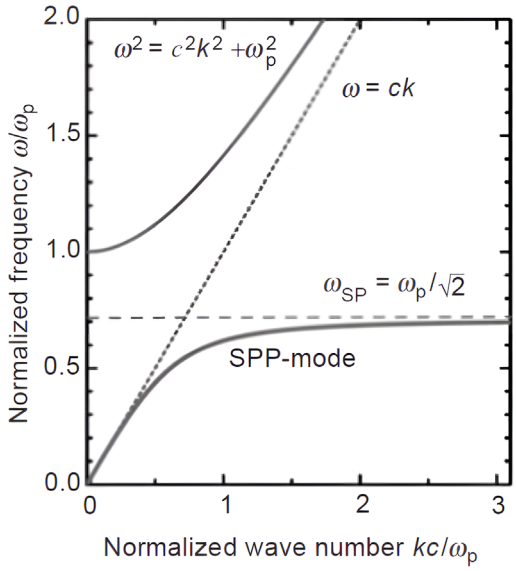

Figure 2.5 Dispersion relation of surface plasmon polaritons (SPPs) at a vacuum-metal interface for three representative cases: an ideal free-electron plasma, a silver surface, and a magnesium surface. The straight dotted line represents the dispersion of electromagnetic waves in vacuum $\omega=ck$ (light cone). The SPP dispersion curve begins at the light line and significantly deviates as frequency increases, approaching the asymptotic surface plasmon frequency $\omega_{SP} = \omega_p / \sqrt{2}$. For $\omega > \omega_p$, wave propagation is again allowed with dispersion given by $\omega^2=c^2k^2+\omega_p^2$, while in the intermediate range $\omega_p/\sqrt{2} < \omega < \omega_p$, no propagating solution exists. This illustrates the forbidden frequency band and the confinement nature of SPPs at subwavelength scales. Figure adapted from [64].

This dispersion relation lies to the right of the light line ($k_{SP} > \omega / c$), meaning that direct excitation from free space light is forbidden due to momentum mismatch. Therefore, external coupling mechanisms such as prism (Kretschmann/Raether configurations) or grating structures are required to excite SPPs [68]. The asymptotic frequency of the SPP mode for a metal–air interface in the limit $\gamma \to 0$ and for air-metal interfaces ($\varepsilon_1 = 1$) simplifies to [64]:

$$\omega_{SP} = \frac{\omega_p}{\sqrt{1+\varepsilon_1}} = \frac{\omega_p}{\sqrt{2}} \tag{2.2.4}$$

This frequency represents the upper limit of the SPP dispersion curve. As shown in Fig. 2.5, the SPP mode initially tracks the light line at low frequencies and gradually deviates as it asymptotically approaches ω_{SPP}, highlighting both the field confinement and the existence of a forbidden band where no SPP propagation occurs.

Understanding these dispersion characteristics is critical for designing THz metasurfaces based on plasmonic resonators, as they define the resonance condition, field confinement, and interaction strength with THz radiation.

2.2.3 Localized surface plasmon resonance

In contrast to surface plasmon polaritons, which propagate along extended metal-dielectric interfaces, localized surface plasmons (LSPs) are confined resonances that occur in subwavelength metallic nanostructures, such as nanospheres, nanorods, or nanocubes [63]. These resonances result from the collective oscillation of conduction electrons in response to an incident electromagnetic field, leading to localized enhancements of the electric field near the nanoparticle surface.

Under the quasistatic approximation—which applies when the particle radius R is much smaller than the incident wavelength λ—the polarizability α of a spherical metallic nanoparticle embedded in a dielectric medium with permittivity ε_{out} is given by [64]:

$$\alpha = 4\pi R^3 \frac{\varepsilon(\omega) - \varepsilon_{out}}{\varepsilon(\omega) + 2\varepsilon_{out}} \tag{2.2.5}$$

The resonance condition occurs when $\mathrm{Re}[\varepsilon(\omega)] = -2\varepsilon_{out}$. This is known as the Fröhlich condition and defines the localized surface plasmon resonance (LSPR) frequency. At this condition, the induced dipole moment is maximized, resulting in strong local field enhancement (see Fig. 2.6).

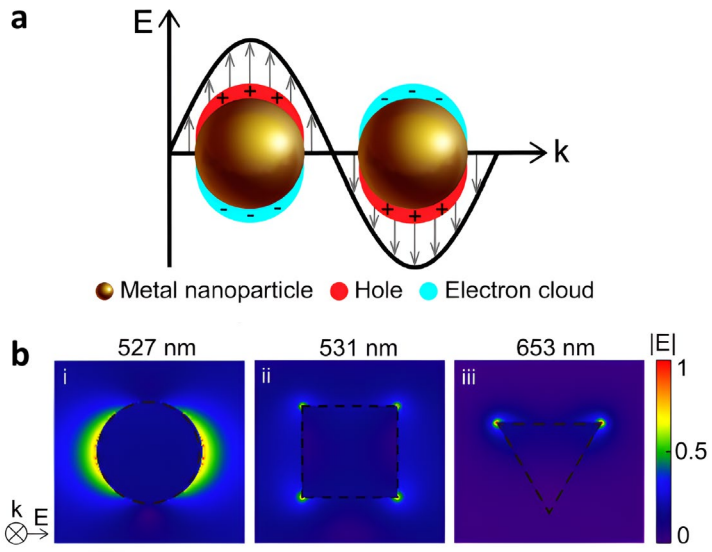

Figure 2.6 Localized surface plasmon resonance (LSPR) in plasmonic nanoparticles. **a** Schematic illustration of the collective oscillation of conduction electrons in response to an incident electric field in nanoparticles significantly smaller than the excitation wavelength. The induced dipole oscillates in the direction opposite to the electric field. **b** Finite-difference time-domain (FDTD) simulations showing the on-resonance normalized electric field magnitude (|E|) for three nanoparticle geometries: (i) nanosphere, (ii) nanocube, and (iii) nanotriangle. Strong field localization is observed, particularly near sharp corners and tips, with rapid spatial decay away from the nanoparticle surface. Figure adapted from [71].

The magnitude and distribution of the field enhancement depend heavily on the nanoparticle geometry and its surrounding medium. Nanostructures with sharp edges or tips, such as nanotriangles, produce even higher localized intensities, which can reach enhancement factors up to 10^4. These field hotspots make LSPRs highly useful in nonlinear optics and sensing applications, particularly at THz and infrared frequencies.

It is important to note that the quasistatic approximation becomes less accurate as the nanoparticle size increases relative to the incident wavelength. In such cases, retardation effects must be considered, which lead to a redshift of the LSPR frequency and broaden the resonance due to radiative damping. These size-dependent effects play a critical role in determining the actual field enhancement and spatial distribution of localized modes, particularly in the THz regime where the

particle dimensions may no longer be negligible. Furthermore, the dielectric function $\varepsilon(\omega)$ of the plasmonic material significantly influences the resonance condition and loss characteristics. For example, noble metals like silver and gold offer sharp and strong resonances in the visible and NIR regimes due to their negative real permittivity and relatively low damping. The balance between the real and imaginary parts of $\varepsilon(\omega)$ defines the resonance sharpness, field confinement, and losses, making material selection a critical factor in LSPR design [63].

In the THz regime, due to the long wavelengths and relatively low photon energies, metals behave as nearly perfect electric conductors. Nevertheless, structured metals still support geometrically induced resonances analogous to plasmonic behavior. In practice, slot arrays, dipolar resonators, or complementary split-ring resonators can produce strong field confinement and resonant effects due to circulating surface currents. By tailoring geometry, environmental permittivity, and material properties, LSPRs can be precisely engineered for advanced applications in THz filtering, nonlinear optics, and sensing platforms [21,26,34].

2.3 Graphene

2.3.1 Band structure and electronic properties

Graphene is a monolayer of carbon atoms arranged in a two-dimensional hexagonal (honeycomb) lattice, as illustrated in Fig. 2.7. Each carbon atom in the lattice is covalently bonded to three nearest neighbors via strong σ bonds, which are formed through the sp^2 hybridization of its valence orbitals: $2s$, $2p_x$, and $2p_y$ [45,72], as shown in Fig. 2.7b. These σ-bonds are responsible for the exceptional mechanical strength of graphene. The fourth valence electron occupies the out-of-plane $2p_z$ orbital, forming delocalized π-bonds by overlapping with adjacent $2p_z$ orbitals. These π-bonds facilitate electrical conduction in graphene, distinguishing it from other materials where all valence electrons are involved in in-plane bonding.

Graphene's exceptional electronic behavior originates from its bipartite lattice structure, which can be viewed as two interpenetrating triangular sublattices, labeled A and B. The primitive lattice

vectors of the Bravais lattice define the periodicity, with a lattice constant of $a=|a_1|=|a_2|=0.246$ nm related to the carbon–carbon bond length $a_{cc}=0.142$ nm by $a=\sqrt{3}a_{cc}$ [45,72].

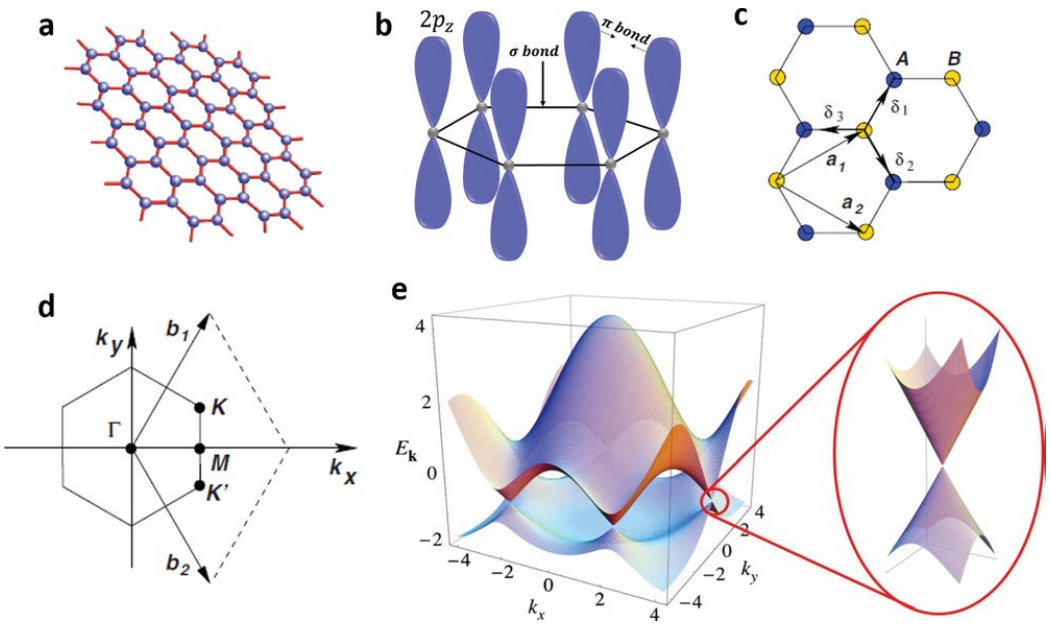

Figure 2.7 Graphene lattice and band structure: **a** Two-dimensional hexagonal honeycomb lattice of graphene, **b** sp^2 bonding between carbon atoms forming strong in-plane σ bonds, along with delocalized out-of-plane π bonds formed by overlapping $2p_z$ orbitals, **c** bipartite structure composed of sublattices *A* and *B*, **d** first Brillouin zone with two inequivalent sets of Dirac points. and **e** the energy–momentum dispersion obtained from the tight-binding model, showing the gapless band structure. Figure adapted from [45,73].

In reciprocal space, the first Brillouin zone of graphene is a hexagon with six high-symmetry corner points known as Dirac points. These Dirac points are grouped into two inequivalent sets, *K*-points, reflecting the underlying *A* and *B* sublattices (Fig. 2.7d). At these points, the valence and conduction bands touch, resulting in a gapless linear dispersion — a hallmark of graphene's electronic structure (Fig.2.7e). This band structure was first derived by Wallace in 1947 [74] using the tight-binding approximation, which captures the cosine-like energy bands that appear in energy–momentum space [72].

$$\epsilon(k_x, k_y) = \pm\gamma_0 \left[1 + 4\cos\left(\frac{\sqrt{3}k_x a}{2}\right)\cos\left(\frac{k_y a}{2}\right) + 4\cos^2\left(\frac{k_y a}{2}\right) \right]^{1/2}, \quad (2.3.1)$$

where $\gamma_0 \approx 2.8\,\text{eV}$ is the nearest-neighbor hopping energy, and k_x, k_y are components of the wavevector. The + and − signs represent the conduction and valence bands, respectively, which touch at the Dirac points where E=0. Near these Dirac points (K and K') in the Brillouin zone, where $|ka| \ll 1$, the energy dispersion becomes linear, giving rise to massless Dirac fermion behavior — a unique feature of graphene [72]:

$$\epsilon_{\pm}(k) = \pm\hbar v_F \,|\, k \,|, \quad (2.3.2)$$

Where, $v_F = \frac{\sqrt{3}}{2}\frac{\gamma_0 a}{\hbar} \approx 10^6\,\text{m/s},$ is the Fermi velocity. This linear energy–momentum relation, valid for energies up to approximately 1.5 eV from the Dirac points, is responsible for many of graphene's unique electronic and optical properties. It leads to the massless Dirac fermion behavior that distinguishes graphene from conventional semiconductors.

2.3.1.1 Density of states

The density of states $D(\epsilon)$ within the linear dispersion regime is proportional to the absolute value of the energy [74]:

$$D(\epsilon) = \frac{2}{\pi\hbar^2 v_F^2} \,|\, \epsilon \,| \quad (2.3.3)$$

This results in a vanishing DOS at the Dirac point (ϵ=0), $D(\epsilon)$=0), highlighting the semi-metallic nature of graphene and the absence of a bandgap.

2.3.1.2 Fermi energy and carrier density

The Fermi energy E_F in graphene is directly related to the carrier density, n_c, by [38]:

$$E_F = \hbar v_F \sqrt{\pi n_c}. \quad (2.3.4)$$

For a typical carrier density of $n_c = 10^{12}$ cm^{-2}, the Fermi energy is approximately $E_F \approx 0.12$ eV.

Graphene's massless charge carriers with linear dispersion behave fundamentally differently from the massive carriers in traditional semiconductors. The lack of a bandgap prevents electrostatic confinement of electrons, which contributes to graphene's unique transport and optical characteristics, setting it apart from gapped two-dimensional materials such as transition metal dichalcogenides [75].

2.3.1.3 Bandgap tuning

While pristine graphene is gapless, a bandgap can be introduced through various methods. For example, in bilayer graphene, applying a perpendicular external electric field can open a tunable bandgap [76]. Alternatively, chemical functionalization—such as hydrogenation or oxidation—can break sublattice symmetry and induce a gap [77,78]. These tunable electronic properties make graphene a highly versatile platform for THz photonics and optoelectronic applications, where both adjustable conductivity and controllable nonlinearities are critical advantages.

2.3.2 Optical conductivity of graphene

2.3.2.1 Linear light–matter interaction in graphene

Graphene's unique optical and electronic properties arise predominantly from its two-dimensional honeycomb lattice structure, which exhibits massless Dirac fermions. The linear band dispersion near the Dirac points leads to an extraordinary interaction of graphene with electromagnetic fields, notably in the THz frequency regime. When graphene is illuminated by electromagnetic radiation, electrons in graphene respond through both interband and intraband transitions. In the linear optical regime, these processes are governed by the optical conductivity $\sigma(\omega)$, which describes the current induced by an electric field at frequency ω. The relationship is given by:

$$\vec{J}(\omega) = \sigma(\omega)\vec{E}(\omega) \tag{2.3.5}$$

The total optical conductivity can be expressed as the sum of two components:

$$\sigma(\omega) = \sigma_{\text{intra}}(\omega) + \sigma_{\text{inter}}(\omega) \tag{2.3.6}$$

Here, $\sigma_{intra}(\omega)$ represents intraband (Drude-like) conductivity, while $\sigma_{inter}(\omega)$ represents interband transitions [79,80]. The dominance of each mechanism depends on the photon energy $\hbar\omega$ and the Fermi energy E_F.

2.3.2.2 Interband conductivity

The interaction of graphene with light depends on the photon energy $\hbar\omega$ and the Fermi energy E_F. When $\hbar\omega > 2E_F$, graphene undergoes interband transitions, where electron-hole pairs are generated, similar to photoexcitation in conventional semiconductors (Fig. 2.8a). This process was initially studied in detail by [81]. In this regime, graphene exhibits a unique and universal absorption coefficient that is independent of frequency and is given by $A = \pi\alpha \approx 2.3\%$. Where $\alpha = \frac{1}{4\pi\epsilon_0}\frac{e^2}{\hbar c} = \frac{1}{137}$ is the fine structure constant. This results in a universal optical conductivity for graphene, $\sigma_0 = e^2 / 4\hbar$.

This universal absorption arises from the linear energy-momentum relationship in graphene's band structure, which contrasts sharply with the nonlinear band dispersion in other materials. However, for photon energies outside the linear band regime ($\hbar\omega$ < 0.5 eV or $\hbar\omega$ > 2 eV), deviations from this universal absorption occur due to nonlinearity. The more general, frequency-dependent expression for interband conductivity at finite temperature is given by [80,82]:

$$\sigma_{inter}(\omega) = \frac{e^2}{8\hbar}\left[\tanh\left(\frac{\hbar\omega + 2E_F}{4k_B T_e}\right) + \tanh\left(\frac{\hbar\omega - 2E_F}{4k_B T_e}\right)\right] \tag{2.3.7}$$

where k_B is the Boltzmann constant, and T_e is the electron temperature. In the high-frequency limit ($\hbar\omega \gg 2E_F$), this expression reduces to the universal conductivity $\sigma_0 = e^2 / 4\hbar$

2.3.2.3 Intraband conductivity

When the photon energy satisfies $\hbar\omega < 2E_F$, interband transitions are blocked due to the Pauli exclusion principle, and intraband transitions dominate the optical response (Fig. 2.8b). In this

regime, electrons absorb THz radiation by transitioning between energy states within the same band. The frequency-dependent intraband conductivity can be derived from the semiclassical Boltzmann transport equation [44,80,83] and is expressed as:

$$\tilde{\sigma}_{\text{intra}}(\omega) = -\frac{e^2 v_F^2}{2}\int_0^{\infty}\left(\frac{\partial f_{\text{FD}}(\epsilon,\mu,T_e)}{\partial\epsilon}\right)D(\epsilon)\frac{\tau(\epsilon)}{1-i\omega\tau(\epsilon)}d\epsilon \tag{2.3.8}$$

Where, $\tau(\epsilon)$ is the electron momentum scattering time, $f_{FD}(\epsilon, \mu, T_e)$ is the Fermi-Dirac distribution function, and $D(\epsilon)$ is the density of states. In low-temperature conditions ($T_e \ll E_F / k_B$) and the electron scattering time at the Fermi energy, $\tau = \tau(E_F)$, the intraband conductivity simplifies to the Drude-type model [80,81]:

$$\tilde{\sigma}_{\text{intra}}(\omega) = \frac{2e^2\tau}{\pi\hbar^2(1-i\omega\tau)}k_B T_e \ln\left[2\cosh\left(\frac{E_F}{2k_B T_e}\right)\right] \tag{2.3.9}$$

This Drude-like behavior explains graphene's strong absorption and high carrier mobility in the THz and mid-infrared spectral regions. The interplay of intraband and interband processes significantly influences the THz response of graphene. For photon energies below $2E_F$, the interband transitions are typically suppressed due to Pauli blocking, leaving intraband transitions as dominant. Conversely, at higher frequencies (or when the Fermi energy is low), interband processes become more significant. This transition between regimes is illustrated schematically in Fig. 2.8.

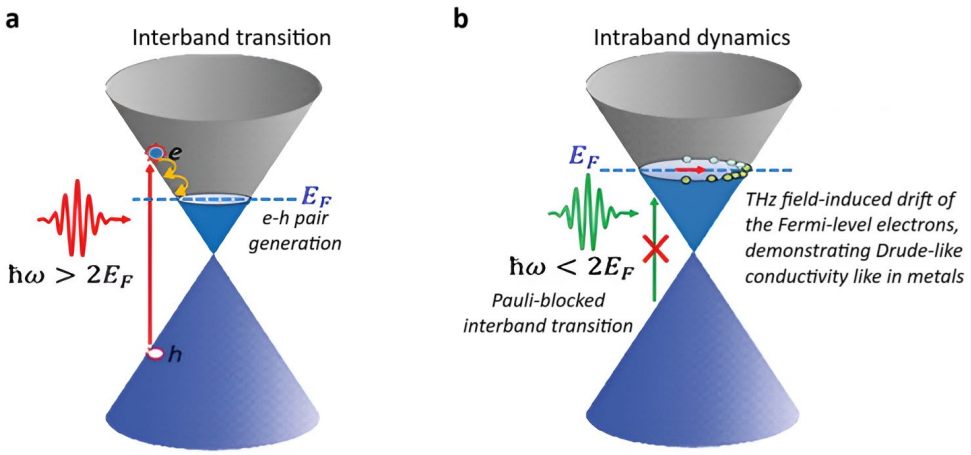

Figure 2.8 Schematic of graphene's band structure illustrating two regimes of light–matter interaction. **a** Interband transitions occur when the photon energy exceeds twice the Fermi energy $\hbar\omega > 2E_F$, resulting in electron–hole pair generation. These photoexcited carriers subsequently undergo energy and momentum redistribution via electron–electron scattering. **b** Intraband transitions dominate when $\hbar\omega < 2E_F$ giving rise to Drude-like intraband conductivity characteristic of free-carrier absorption. Figure adapted from [48]

2.3.3 THz excitation of graphene

At room temperature ($T_e = 300$ K), the photon energy in the THz range (e.g., 1 THz corresponding to 4.1 meV) is much smaller than the thermal energy ($k_B T_e = 26$ meV). This results in effective Pauli blocking of interband transitions, leaving intraband transitions to dominate. For intrinsic graphene with $E_F \approx 0$, the conduction and valence bands are thermally populated almost equally, leading to negligible interband transitions at room temperature. In large-scale samples, charge puddles create local doping variations, further complicating interband transitions [84]. Most single-layer graphene samples exhibit unintended doping due to preparation and environmental effects. Common causes include:

1. Chemical Vapor Deposition (CVD): Residual PMMA used in the transfer process induces hole-doping.
2. Epitaxial Graphene on SiC: Charge transfer from the substrate results in electron-doping.

3. Environmental Interactions: Water and oxygen molecules trapped between the graphene and substrate further contribute to doping.

Such doping shifts the Fermi energy, altering the interaction of graphene with light, particularly in the THz frequency range.

In typical CVD-grown graphene samples, the Fermi energy E_F lies in the range of approximately 50 meV to 260 meV, depending on fabrication conditions and substrate-induced doping. This doping level critically affects whether THz excitation drives intraband or interband transitions. Moreover, E_F can be dynamically tuned using electrostatic gating. Applying gate voltages within a range of ±2 V can shift the Fermi energy by more than 200 meV, offering a versatile method to control the carrier density and nonlinear optical response of graphene *in situ* [49].

2.3.3.1 THz transmittance

The transmittance of THz radiation through a graphene layer on a substrate can be described using the Tinkham equation [85], which accounts for the interaction of the THz electric field with the graphene's complex optical conductivity and the substrate's refractive index. The transmittance is expressed as [85]:

$$\tilde{T}(\omega) = \frac{\tilde{E}_s(\omega)}{\tilde{E}_{\text{ref}}(\omega)} = \frac{n_s + 1}{n_s + 1 + Z_0\tilde{\sigma}(\omega)} \tag{2.3.10}$$

Where, $\tilde{T}(\omega)$ is the frequency-dependent transmittance, $\tilde{E}_s(\omega)$ and $\tilde{E}_{ref}(\omega)$ are the THz electric field amplitude transmitted through the substrate with the graphene layer, and bare substrate (reference), respectively. n_s is the refractive index of the substrate, Z_0=377 Ω is the impedance of free space, and $\tilde{\sigma}(\omega)$ is the complex optical conductivity of graphene, encompassing both interband and intraband contributions. This equation effectively relates the measured transmittance to the material properties of graphene and the substrate. The term $Z_0\tilde{\sigma}(\omega)$ reflects the interaction between

the graphene conductivity and the impedance of free space, while n_s+1 accounts for the influence of the substrate on the THz wave propagation.

The Tinkham equation [85] is particularly useful for analyzing experimental data, as it provides a direct means to extract the optical conductivity of graphene from transmittance measurements. This is critical for understanding the interaction of THz radiation with graphene, including its electronic properties and light-matter interactions.

2.3.4 Terahertz nonlinear interactions in graphene

2.3.4.1 Overview of THz nonlinear optical effects in graphene

Graphene's gapless band structure and ultrafast carrier dynamics make it an exceptional platform for exploring nonlinear optical phenomena in the THz regime. Unlike conventional semiconductors with parabolic bands and bound electronic states, graphene supports strong field-driven intraband dynamics due to its linear dispersion near the Dirac points and massless Dirac fermion behavior [48].

In the THz frequency range, nonlinear optical interactions in graphene give rise to phenomena such as HHG, where integer multiples of the incident frequency are emitted [38]. The underlying mechanisms depend strongly on the excitation regime, which is governed by photon energy relative to the Fermi energy E_F , as well as the carrier scattering dynamics.

At photon energies $\hbar\omega < 2E_F$, Pauli blocking inhibits interband transitions, and the response is dominated by intraband (Drude-like) conduction [79,80]. Under intense THz fields, these free carriers gain energy from the field and redistribute it via rapid electron–electron scattering, leading to significant carrier heating. Due to graphene's low electronic heat capacity, the electron temperature can rise to over 1000 K even at field strengths as low as 20 kV/cm [38,48]. This modifies the Fermi–Dirac distribution and reduces the conductivity, producing transient absorption

bleaching and an intensity-dependent nonlinear response. The resulting conductivity change—on ultrafast timescales—underlies a thermodynamic nonlinearity that drives the generation of odd harmonics in transmitted or reflected THz signals [38,48].

The nature of graphene's nonlinear response is further influenced by the underlying carrier transport regime. In the diffusive regime, which dominates on picosecond timescales, nonlinearities primarily arise from hot-carrier effects, where energy absorbed via intraband transitions is rapidly redistributed through electron–electron scattering. This leads to significant carrier heating and modification of the optical conductivity. In contrast, in the ballistic regime, where carriers move coherently on sub-picosecond timescales without scattering, the nonlinear response can become even more pronounced. Under such conditions, electrons can experience field-driven acceleration across the Brillouin zone, giving rise to Bloch oscillations as they approach the zone boundaries and reflect periodically. These coherent dynamics are highly efficient at generating high-order harmonics. Overall, the strong THz nonlinearity of graphene arises from the interplay between its gapless energy dispersion, ultrafast hot-electron dynamics, and efficient intraband heating, positioning it as a compelling platform for nonlinear THz photonics and applications such as high-harmonic generation, optical switching, and compact THz modulators [48].

2.3.4.2 Thermodynamic model of nonlinearity in graphene

A comprehensive understanding of the nonlinear THz response in graphene is provided by a thermodynamic model describing how the intraband optical conductivity evolves as a function of electronic temperature T_e. This model captures the dynamic modulation of conductivity that results from high-field, multi-cycle THz excitation, where each cycle drives intraband currents that deposit energy into the electronic system via Drude absorption. Due to graphene's low electronic heat capacity, this absorption causes T_e to rise rapidly, often exceeding 1000 K even at moderate peak fields of 20–30 kV/cm. The resulting carrier heating broadens the Fermi–Dirac distribution, reducing conductivity as T_e increases [38,44,48]. Within tens of femtoseconds (~10–100 fs),

electron–electron interactions redistribute the absorbed energy, establishing a quasi-equilibrium hot electron population. This hot-carrier-driven reduction in conductivity underlies the thermodynamic nonlinearity modeled in Eq. (2.2.9).

As this thermal broadening reduces the slope of the distribution near the Fermi level, the intraband conductivity drops, leading to a transient suppression of THz absorption, known as bleaching. Because the pulse contains multiple cycles, this process repeats with each cycle: the carriers continue absorbing energy, while simultaneously beginning to cool through optical phonon emission. However, the cooling rate is slower than the heating rate—primarily due to a combination of energy dissipation mechanisms including electron–phonon scattering, supercollision cooling via disorder-assisted processes, and coupling to substrate phonons [48]. Although ultrafast processes such as electron–electron scattering and initial optical phonon emission occur within tens to hundreds of femtoseconds, these mechanisms primarily govern early-stage carrier redistribution and partial energy loss, rather than full energy dissipation to the lattice. The overall carrier cooling is limited by the slow decay of the generated hot optical phonons, which have lifetimes of 1–3 ps and only weakly couple to acoustic phonons, making energy transfer to the lattice inefficient. This phonon-limited relaxation creates a bottleneck in energy transfer from the electronic system to the lattice, consistent with previous THz pump–probe measurements in graphene [48]. As a result, the total carrier cooling time remains in the picosecond range, well beyond the initial ultrafast scattering events.

Among these scattering mechanisms, emission of optical phonons near the Γ and K points plays a dominant role in transferring energy from the electronic system to the lattice. This process unfolds over a timescale of 0.1–1 ps, resulting in a net accumulation of heat within the electronic system during the pulse. This leads to a temporally asymmetric evolution of the conductivity, where each subsequent THz cycle interacts with a hotter electron distribution than the previous one. This heating–cooling cycle within the pulse envelope is central to the thermodynamic model.

The cumulative heat deposited into the electron system is represented by $\Delta Q(t)$, which plays a pivotal role in the thermodynamic model by capturing the energy buildup within the electronic system over time. It reflects how the sequential absorption of energy during each THz field cycle leads to conductivity suppression. As $\Delta Q(t)$ increases, it governs the modulation of the electron temperature and dynamically alters the conductivity profile, which in turn shapes the nonlinear optical response and facilitates harmonic generation. While not presented in an explicit analytical form, $\Delta Q(t)$ is extracted through numerical modeling and corresponds to the results shown in Fig. 2.9c, based on the driving field shown in Fig. 2.9b. The calculation of $\Delta Q(t)$ incorporates the evolving intraband conductivity $\sigma(T_e)$, which depends on the Fermi–Dirac distribution and energy-dependent scattering, as well as the time-dependent input and output electric fields. A phenomenological cooling function is used to account for carrier energy relaxation, enabling the model to capture the cumulative thermal effects induced by the pulse. The time-domain asymmetry in electronic heating and cooling, and its impact on the temporal evolution of conductivity and absorbance as discussed in [38,44] is illustrated in Fig.2.9, which visualizes how different peak field strengths modulate the internal energy accumulation and nonlinear optical response of graphene.

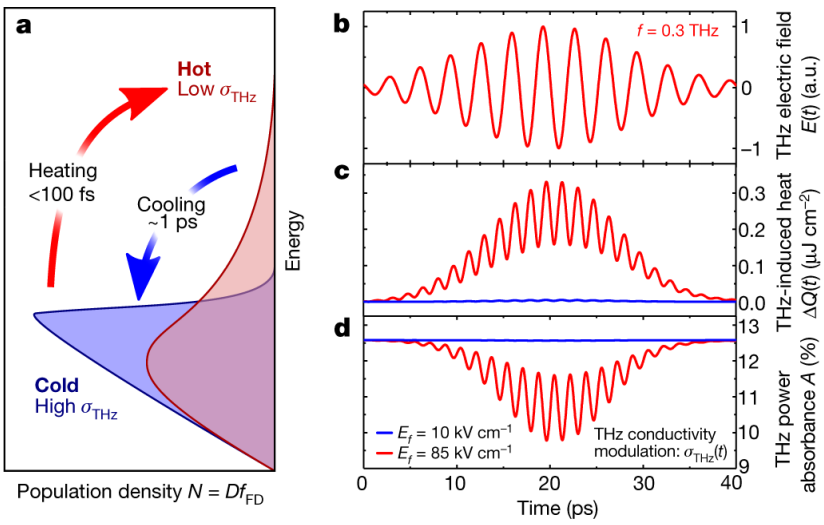

Figure 2.9 a Temporal asymmetry between electron heating and cooling dynamics in graphene under strong-field THz excitation. The non-equilibrium energy exchange processes lead to a temporal accumulation of electronic heat $\Delta Q(t)$. **b** Application of a THz driving pulse at 0.3 THz induces these thermal dynamics. **c** The resulting $\Delta Q(t)$ shows a pronounced asymmetry depending on the field strength, with blue and red curves corresponding to peak fields of 10 kV/cm and 85 kV/cm, respectively. **d** This thermal modulation manifests as a time-dependent reduction in THz absorbance and conductivity. At low field strength, graphene remains in the linear regime with negligible modification of optical properties, while higher fields produce strong nonlinear responses due to significant carrier heating. Figure adapted from [38].

2.3.4.3 Ultrafast carrier dynamics in graphene

Understanding the nonlinear THz response in graphene requires a detailed consideration of ultrafast carrier dynamics. The optical nonlinearity arises not only from the field-induced redistribution of carriers but also from how rapidly these carriers can exchange energy and momentum with each other and with the lattice. Table 2.1 summarizes the key timescales governing these dynamics [48]. These timescales dictate the window over which THz-induced nonlinear phenomena—such as saturation, harmonic generation, and refractive index modulation—can occur. They are particularly critical for understanding the thermodynamic model of conductivity, where the heating–cooling asymmetry plays a defining role in determining the field-dependent response of the material.

Table 1 Characteristic carrier dynamics timescales in graphene relevant to THz nonlinear optics

Process	Timescale	Description
Electron–electron scattering	10–100 fs	thermalization via Coulomb interactions; establishes hot Fermi–Dirac distribution.
Electron–SCOP* scattering	10–100 fs	cooling via strongly coupled optical phonons.
Electron–phonon scattering	~1 ps	energy transfer to the lattice through phonon emission (Γ and K points).
Total carrier cooling time	1–3 ps	full thermal relaxation to ambient lattice temperature.
Effective carrier lifetime	<1 to few ps	depends on doping/gating; affects nonlinear response duration.

*SCOP = strongly coupled optical phonons.

2.3.4.4 Saturable absorption and nonlinear refractive index

A fundamental nonlinear mechanism in graphene arises from saturable absorption (SA) [86,87], in which the material's absorption decreases with increasing incident field intensity [38,44]. This behavior is particularly prominent in the THz regime, where intraband transitions dominate and carrier heating significantly alters the material's conductivity. Under low-field conditions, graphene behaves as a lossy medium with strong Drude-like absorption. As the THz field strength increases, carriers gain energy and rapidly heat due to graphene's low electronic heat capacity. This leads to a redistribution of the Fermi–Dirac distribution, which reduces intraband conductivity and causes the absorption to bleach — i.e., saturate. At field strengths exceeding 20 kV/cm, this bleaching becomes significant. The effect is dynamic and reversible, governed by rapid carrier heating and subsequent cooling, and plays a key role in enabling high-harmonic generation.

The phenomenon was directly observed through experimental measurements of THz transmission, as reported by Hafez et al. [38], and is modeled using a thermodynamic framework. Figure 2.10a presents the measured power absorption and extracted electronic temperatures, which exceed 1000 K at high fields, confirming the role of hot-carrier dynamics in driving nonlinear optical behavior.

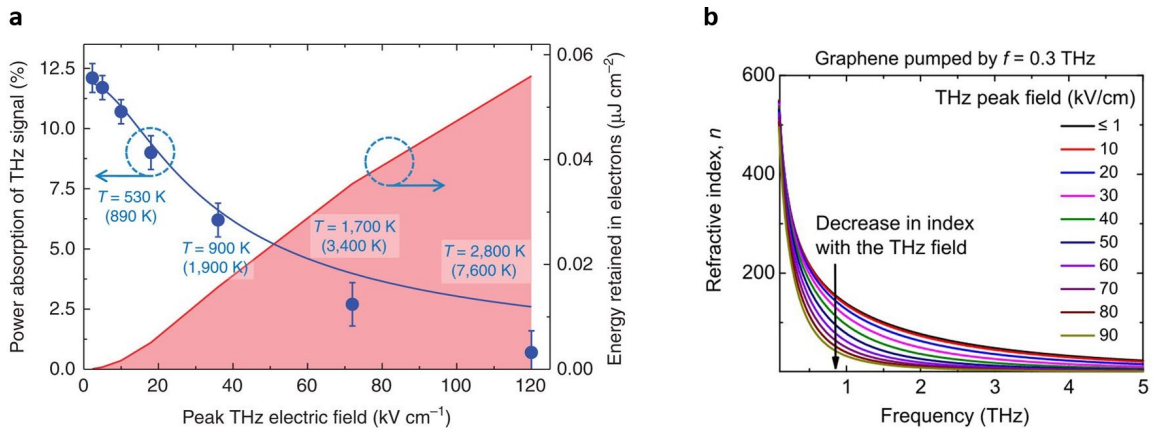

Figure 2.10 a Field-dependent power absorption of graphene and corresponding electronic heating. Blue data points show the measured integrated power absorption as a function of the peak THz field, while the blue solid curve represents predictions from the time-dependent thermodynamic model. The red-shaded area illustrates the retained energy in the electronic system as calculated by the model. Average and peak electron temperatures corresponding to selected THz field amplitudes are annotated. Error bars represent standard deviations of repeated measurements. Adapted from [44]. **b** Real part of the THz refractive index of a monolayer graphene film plotted as a function of frequency under different peak electric field strengths of the 0.3 THz pump. The data clearly reveal a monotonic reduction in refractive index with both increasing frequency and field amplitude, indicating the field-induced optical nonlinearity of graphene. Adapted from [38].

The nonlinear refractive index is derived from the field-dependent conductivity [88,89] via:

$$\varepsilon(\omega) = \varepsilon_{\infty} + \frac{i\sigma(\omega)}{\varepsilon_0 \omega d} \tag{2.3.11}$$

$$n(\omega) = Re\left\{\sqrt{\varepsilon(\omega)}\right\} \tag{2.3.12}$$

where $d = 0.3$ nm is the monolayer graphene thickness. As conductivity decreases with heating, the real part of the refractive index decreases, mimics Kerr-type nonlinearities [12,90]. This field-dependent reduction in refractive index is illustrated in Figure 2.10b, where increasing THz pump strength leads to a clear, monotonic decline in refractive index across the measured frequency range.

2.4 Graphene oxide

2.4.1 Structure, synthesis, and fabrication

Graphene oxide (GO) is a chemically derived form of graphene obtained by oxidizing graphite using strong oxidizing agents such as potassium permanganate ($KMnO_4$) and sulfuric acid (H_2SO_4) [91,92]. A common synthesis approach is the modified Hummers' method, where graphite layers undergo intercalation and oxidation to form graphite oxide. Subsequent exfoliation processes involving debonding of graphite oxide yield graphene oxide, a two-dimensional, single-layer derivative enriched with various oxygen-containing functional groups. These groups, primarily hydroxyl (-OH), epoxy (C–O–C), carbonyl (C=O), and carboxylic acid (-COOH), are covalently bonded to the basal plane and edges of the graphene sheets [92,93]. As a result, GO exhibits a unique amorphous-like structure with a heterogeneous mixture of sp^2 and sp^3 hybridizations, significantly differentiating it from pristine graphene, which is composed entirely of sp^2-hybridized carbon atoms arranged in a regular hexagonal lattice [52,94] (Fig. 2.11b).

Reduced graphene oxide (rGO) is synthesized by partially removing these oxygen-containing functional groups from GO through chemical, thermal, electrochemical, or photothermal reduction methods. This reduction minimizes oxygen functionalities, restores sp^2 carbon domains, and significantly enhances electrical conductivity [94]. However, rGO typically retains residual functional groups and structural defects, distinguishing it structurally and optically from pristine graphene (Fig. 2.11c). Highly reduced graphene oxide (hrGO) represents the most extensively reduced variant, closely approaching the properties of pristine graphene. This material features minimal oxygen functionalities, a substantially increased fraction of sp^2 carbon, and markedly improved electrical conductivity and optical performance, rendering it particularly attractive for advanced optoelectronic and photonic applications [52,94] (Fig. 2.11d).

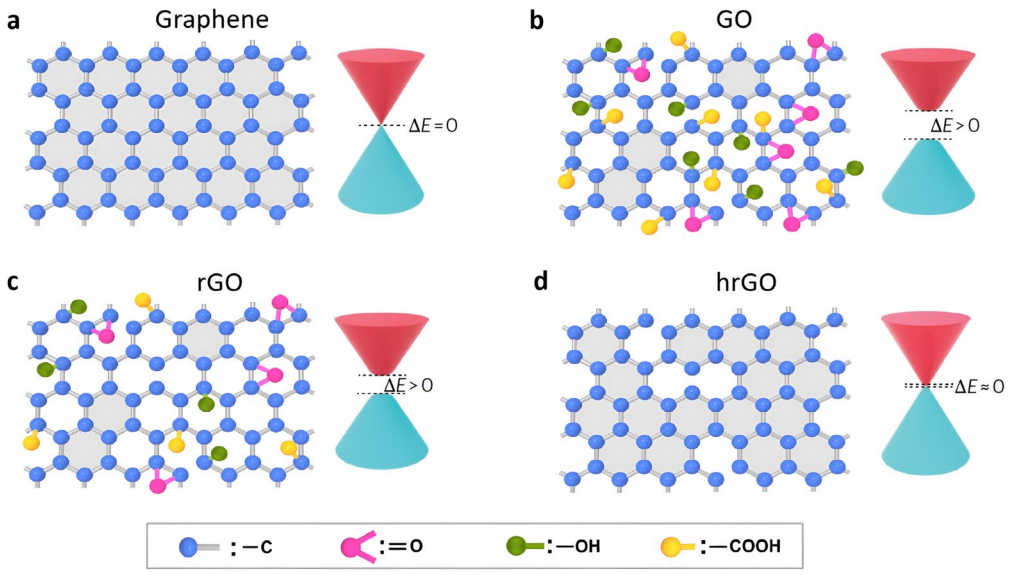

Figure 2.11 Schematics of atomic structures of **a** graphene, **b** graphene oxide (GO), **c** reduced graphene oxide (rGO), and **d** highly reduced graphene oxide (hrGO). Figure adapted from [51]

GO and its reduced forms can be fabricated into films or coatings through several practical methods, each offering specific advantages and applicability [52] (see Fig. 2.12):

- Drop casting: involves depositing droplets of GO solution onto a substrate and allowing it to dry, forming a relatively thick, uniform film.
- Spray coating: utilizes a nozzle to aerosolize GO solution, uniformly spraying a fine mist onto substrates, suitable for large-area and irregularly shaped surfaces. This is the process we use in our sample fabrication.
- Spin coating: employs a rotating substrate onto which GO solution is dispensed; the centrifugal force spreads the solution uniformly, creating smooth and thin films.
- Filtration method: relies on vacuum filtration to separate GO flakes from a suspension, depositing them onto filtration membranes that are subsequently transferred onto flexible or rigid substrates.

- Doctor Blade method: involves moving a sharp blade at a fixed distance above a substrate, uniformly spreading GO slurry into a wet film, which is then dried to yield uniform, scalable films suitable for flexible and large-area applications.

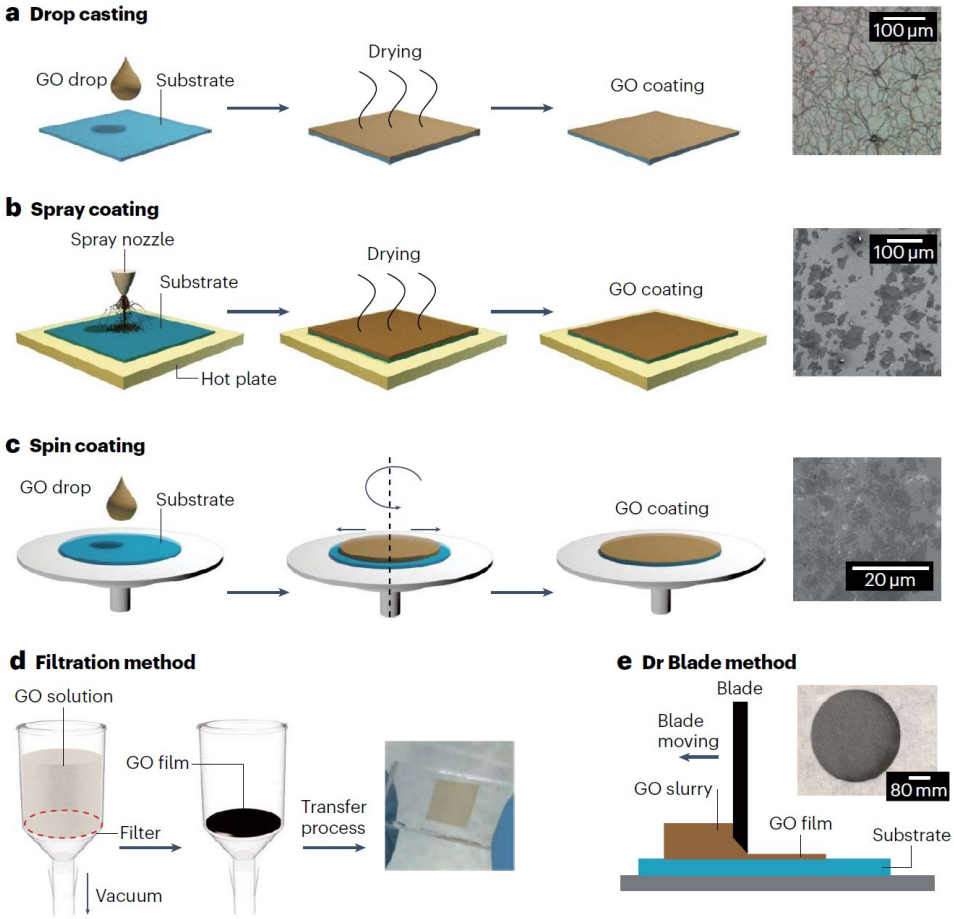

Figure 2.12 Fabrication methods for graphene oxide films. **a** Drop casting method. Inset: transmission optical microscope image of the GO film. **b** Spray coating method. Inset: SEM image of spray-coated GO flakes. **c** Spin coating method. Inset: SEM image of spin-coated GO film. **d** Filtration method. Inset: photograph of GO film on a flexible substrate. **e** Doctor Blade method. Inset: photograph of a free-standing GO film. Figure adapted from [52].

These fabrication techniques are crucial for integrating GO-based materials into various photonic, electronic, and optoelectronic device architectures, enabling the manipulation and enhancement of their functional properties for targeted applications.

2.4.2 Linear optical properties of GO

GO, rGO, and hrGO exhibit distinctly different linear optical characteristics due to their varying degrees of oxidation and structural modifications. GO typically has a refractive index of approximately 1.97 in the NIR region, and its extinction coefficient ranges from 0.005 to 0.01, indicative of relatively low optical absorption. The presence of oxygen-containing groups significantly influences its electronic band structure, imparting a wide optical bandgap ranging between 2.1 and 3.6 eV, which enables its use in optoelectronic devices and transparent conductive coatings [91,94,95].

Upon reduction to rGO, optical properties shift notably. The refractive index of rGO increases moderately, accompanied by a significant rise in optical absorption across visible and NIR regions. This transition reflects changes in electronic structure due to partial removal of oxygen-containing functionalities, which narrows the optical bandgap. Highly hrGO demonstrates further enhancement in optical absorption and a substantial increase in refractive index, approaching around 2.7, indicative of extensive removal of oxygen functionalities and restoration of sp^2 hybridized carbon domains [51]. Figure 2.13 compares refractive index of the graphitic materials.

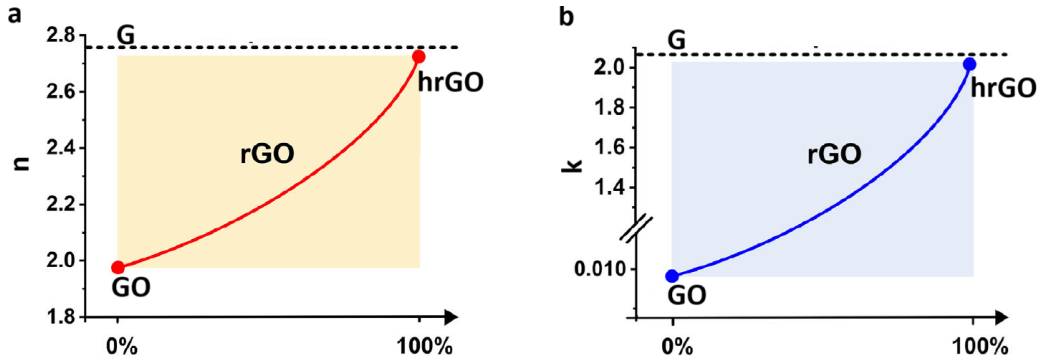

Fig. 2.13. Linear optical properties of graphitic materials. **a** refractive index (n) and **b** extinction coefficient (k) of graphene (G), rGO and hrGO. Figure adapted from [51]

In the THz regime, these properties translate into intriguing behaviors. Reduced GO films exhibit broadband THz absorption [40] and high conductivity (~900 S/cm) [96], which can be fine-tuned

through reduction levels, film thickness, and optical pumping [41]. Optically pumped GO displays increased photoinduced conductivity along with a peculiar non-Drude relaxation behavior [97], unlike PG and highly reduced GO (hrGO). The ultrafast relaxation dynamics in hrGO are primarily governed by carrier–carrier scattering and carrier–phonon coupling. These features have motivated the use of GO and its derivatives in THz devices, including absorbers [40], anti-reflection coatings [98], and sensors [99].

2.4.3 Nonlinear optical properties of GO

The nonlinear optical properties of GO-based materials are remarkable and extensively studied due to their significant potential in photonic and optoelectronic applications [51]. GO exhibits substantial third-order nonlinearities characterized by a high Kerr nonlinear coefficient (n_2), generally in the range of 1.5–4.5 × 10^{-14} m^2/W [53,54]. Such pronounced nonlinearity originates primarily from the oxygen-containing functional groups and localized electronic states within the GO structure. GO also exhibits strong saturable absorption, quantified by a nonlinear absorption coefficient (β) approximately ~ -6 × 10^{-8} m/W [53,54]. This saturable absorption is mainly due to ground-state bleaching in sp^2 carbon domains, making GO an attractive candidate for ultrafast photonic devices such as mode-locked lasers and ultrafast optical switches [100,101]. Upon further reduction, rGO and hrGO show even stronger nonlinear optical responses due to increased conductivity, fewer oxygen groups, and enhanced electronic delocalization. The resulting nonlinear refractive indices and saturable absorption characteristics are significantly enhanced, facilitating their applications in high-power and ultrafast nonlinear optics. A wide range of nonlinear optical processes—such as self-phase modulation [102], four-wave mixing [55], multiphoton absorption and luminescence [56,103] —have been demonstrated in GO and its reduced forms.

Chapter 3

Experimental Details

In this chapter, we describe the experimental methods, sample preparation procedures, and technical implementations used to conduct the measurements presented in Chapters 4–6. We begin with a detailed overview of the experimental setup used to generate intense THz fields. Subsequently, we discuss the fabrication of graphitic samples, including the transfer and gating of CVD graphene, as well as the preparation and functionalization of graphene oxide samples. The chapter concludes with the design and fabrication of plasmonic metasurfaces, which were developed using finite-difference time-domain (FDTD) simulations and fabricated via photolithographic techniques.

3.1 High-field THz setup

Intense THz pulses were generated through optical rectification in a lithium niobate ($LiNbO_3$) crystal using the tilted-pulse-front technique [16]. A schematic of the experimental setup is shown in Figure 3.1, where an amplified mode-locked laser is used as the pump source. Two types of amplified lasers were used in the setup across different experiments. The first was a PHAROS laser from Light Conversion, based on a Yb:KGW system, operating at a central wavelength of 1030 nm, with pulse duration of 170 fs, pulse energy of 1 mJ, and a repetition rate tunable between 6 kHz and 1 MHz. The second system was a Ti:sapphire amplifier with a center wavelength of 800 nm, pulse duration of 45 fs, pulse energy of 2 mJ, and repetition rate of 1 kHz.

The laser output was split into two beams using a polarizing beam splitter (PBS) and a half-wave plate (HWP). One beam was directed to generate THz radiation by optical rectification in the $LiNbO_3$ crystal, while the other beam was routed through a mechanical delay line and used as the probe in electro-optic sampling. To realize a tilted pulse front, the pump beam was diffracted using a transmission grating and re-imaged into the $LiNbO_3$ crystal using a cylindrical lens system. Polarization control was achieved using a polarizing beam splitter (PBS) and a half-wave plate to maximize diffraction efficiency. The generated THz field could reach amplitudes up to 360 kV/cm. To compensate for group velocity dispersion (GVD) introduced by transmissive optics, a negative chirp was applied to the NIR pulse prior to THz generation. After optical rectification, the THz beam was collimated and focused using a pair of off-axis parabolic mirrors (OPMs). A pair of free-standing wire-grid polarizers was placed before the sample to fine-tune the incident THz field strength.

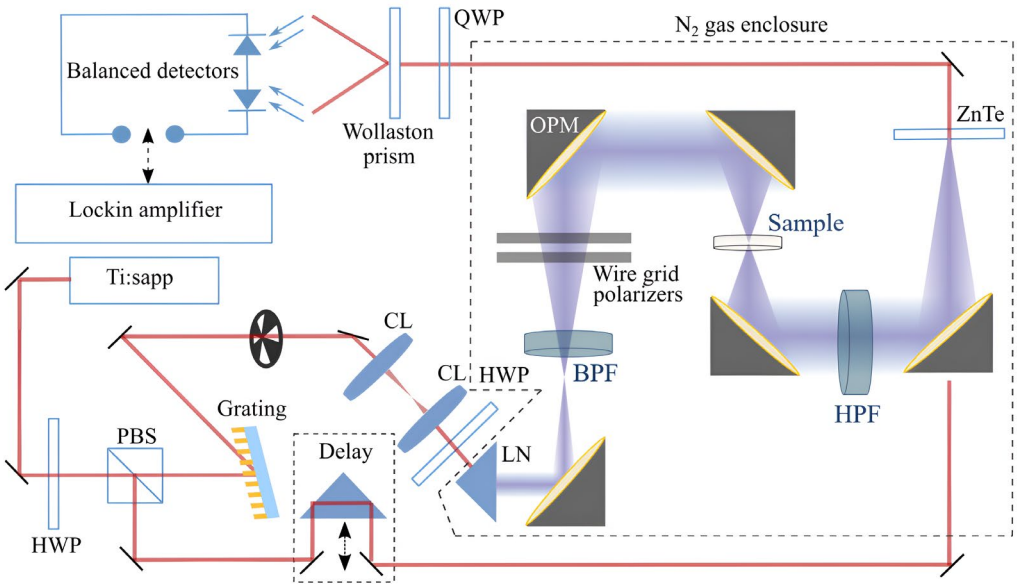

Figure 3.1 Schematic of the high-field THz setup. PBS: Polarizing beam splitter; OPM: Off-axis parabolic mirror; HWP: Half-wave plate; QWP: Quarter-wave plate; PD: Photodetector; CL: Cylindrical lenses; LN: lithium niobate; BPF: Bandpass filter; HPF: Highpass filter [61].

The second beam, acting as a probe, was used to resolve the time-domain electric field of the THz pulse using electro-optic sampling (EOS). EOS is a time-resolved detection technique in which the THz-induced birefringence in an electro-optic crystal modulates the polarization state of a co-propagating probe beam [104]. A 500 μm-thick ZnTe crystal was used for this purpose. The induced polarization change was detected through a balanced detection scheme comprising a quarter-wave plate, Wollaston prism, and a pair of photodiodes connected to a lock-in amplifier. The entire THz beam path was enclosed in a nitrogen-purged enclosure to eliminate absorption from atmospheric water vapor. This configuration ensured a stable and high signal-to-noise ratio for time-resolved nonlinear experiments.

A representative time-domain waveform of the THz electric field and its Fourier-transformed spectrum are shown in Figures 3.2(a) and 3.2(b), respectively. These data demonstrate the broadband nature of the generated THz pulses and serve as a baseline for evaluating spectral shaping introduced by optical filters used in the experiment.

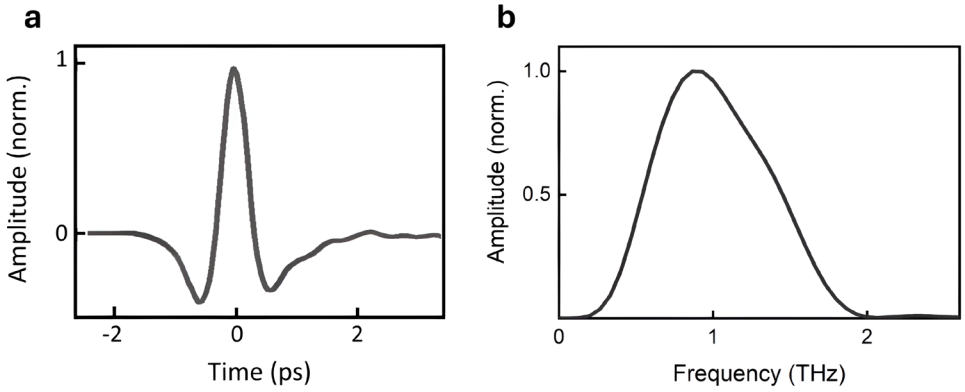

Figure 3.2 a Time-domain THz transient measured in air. **b** Corresponding THz spectrum calculated by Fourier transform

To quantify the peak electric field strength of the THz pulse at the focal point in THz setup, we use a standard EOS calibration method based on the response of the detection crystal. The THz field strength E_{THz} is derived from the normalized EOS signal through the following relation [105]:

$$E_{THZ} = \frac{A-B}{A+B} \cdot \frac{\lambda_{gat} K_{gat}}{2\pi r_{41} n_0^3 L t_{tot}}$$

Here, A and B are the voltages measured by the balanced photodiodes, λ_{gat} is the central wavelength of the gating beam, r_{41} is the electro-optic coefficient of the detection crystal, n_0 is its refractive index at the gating wavelength, and L is the crystal thickness. The factor t_{tot} accounts for transmission losses due to the THz interaction with intermediate optical components (e.g., Fresnel reflections at the surface of the detection crystal).

To precisely shape the spectral content of the THz pump and improve the sensitivity of high-order nonlinear measurements such as HHG, we implemented a configuration of filters using a bandpass filter (BPF) and a highpass filter (HPF) that is shown schematically in Fig. 3.3. The BPF, placed before the sample, narrows the THz spectrum and serves to isolate a specific frequency window used to drive the nonlinear interaction. After the sample, an HPF is used to block the remaining low-frequency pump and transmit the higher-order generated components, significantly enhancing the sensitivity of time-resolved detection to weak harmonic signals. A detailed discussion of the design principles and fabrication of the BPF and HPF filters is provided in Chapter 4, and improved performance of the configuration is presented in Chapter 5.

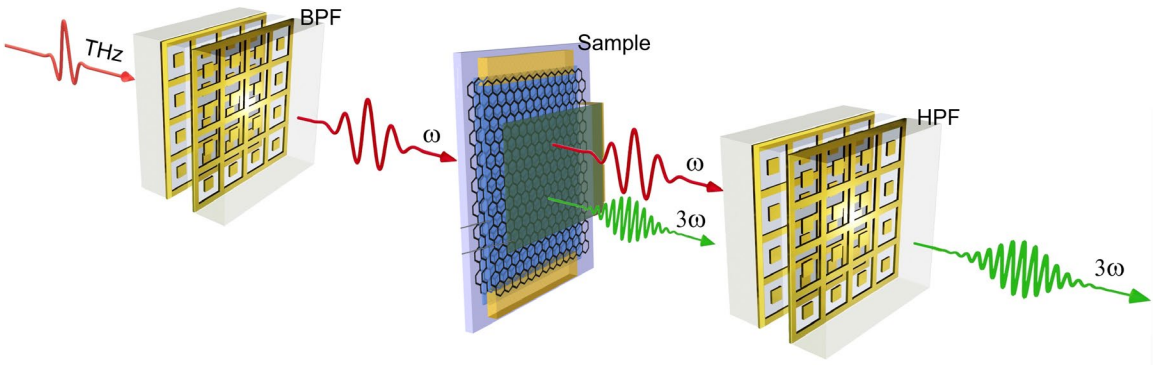

Figure 3.3 Schematic of the filters' configuration at the sample position to improve THz detection sensitivity. A bandpass filter (BPF) transmits a multicycle THz pulse at ω, which produces a signal at 3ω after nonlinear interactions in a graphene sample, and a highpass filter (HPF) attenuates the pump pulse and passes 3ω signal.

3.2 Fabrication of graphitic samples

3.2.1 CVD Graphene and transfer process

Commercial monolayer graphene films were purchased from Graphenea, provided on copper foils and coated with a poly(methyl methacrylate) (PMMA) support layer. These graphene sheets were cut into 1 cm × 1 cm sections and wet-transferred onto Zeonor substrates (188 μm thickness). Zeonor is a cyclo-olefin copolymer that is transparent to THz radiation and has a refractive index of approximately 1.53 at 1 THz [106].

The transfer process is illustrated in Fig. 3.4, which summarizes the sequential steps used to move the graphene from the copper foil onto the desired substrate. First, the sample is exposed to 10 sccm of oxygen plasma in a reactive ion etcher (RIE) at 100 W for 1 minute to remove the unwanted graphene from the backside. After plasma treatment, the sample was immersed in a copper etchant solution at 70°C until all copper was dissolved, then transferred through multiple DI water baths to rinse off residual etchant. The PMMA-graphene film was carefully lifted using an etch-resistant slide and deposited onto the Zeonor substrate. The PMMA layer was dissolved in acetone at 50°C for 1 hour to complete the transfer. This transfer method preserves the monolayer integrity and minimizes contamination, ensuring a high-quality graphene surface suitable for THz optical measurements.

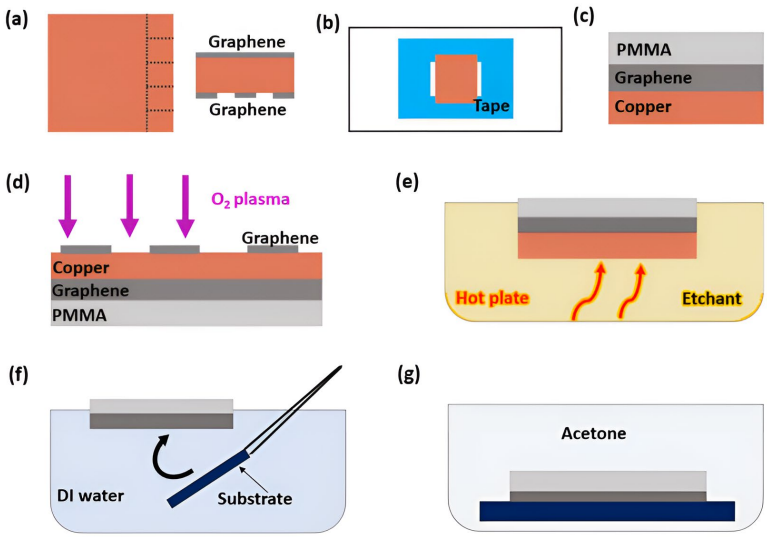

Figure 3.4 Sequential steps of the wet-transfer process for CVD-grown graphene. (a) Copper foil covered with monolayer graphene; dashed lines indicate cutting geometry for individual samples. (b) Sample mounted on a glass slide using adhesive tape. (c) PMMA supporting layer spin-coated over graphene. (d) Backside graphene removed using O_2 plasma. (e) Sample immersed in copper etchant solution. (f) Floating graphene/PMMA film is rinsed in DI water and transferred to the substrate. (g) PMMA is dissolved in acetone to yield the final transferred graphene layer. Schematic of the graphene wet transfer process from copper foil to Zeonor substrate. (a–g) The procedure includes PMMA spin-coating, oxygen plasma treatment, copper etching, DI water rinse, and PMMA removal. Figure adapted from [107].

3.2.2 Multilayer Graphene and Gated Sample Architecture

To fabricate multilayer structures, alternating layers of graphene and a 60 nm-thick Al_2O_3 insulating spacer were sequentially stacked on the same Zeonor substrate. The Al_2O_3 layers were deposited using an electron-beam evaporator (NexdepSeries, Angstrom). The resulting stack maintained spacing between the graphene sheets while preserving optical and electrical isolation.

To implement electrical gating, a set of 5 nm Ti / 20 nm Pd / 150 nm Au electrodes were deposited on the sides of the graphene layers using thermal evaporation through a shadow mask. The source and drain terminals made direct contact with the outermost graphene layers, while the gating contact was applied via a transparent polymer electrolyte. The polymer electrolyte, consisting of

polyethylene oxide (PEO) and $LiClO_4$ in an 8:1 weight ratio, was dissolved in methanol and spray-coated onto the graphene area [108,109]. The complete sample was mounted on a custom-designed printed circuit board (PCB) with a central hole to allow THz transmission. A schematic of the gated multilayer graphene sample structure and a photograph of the fabricated structure on the PCB is shown in Fig. 3.5.

For each device, a gate offset voltage was applied to compensate for intrinsic (usually p-type) doping introduced during the wet transfer or by interfacial effects. The values varied between 0.1–0.3 V across samples and were optimized to shift the Fermi level toward the Dirac point. All electrical measurements were performed using Keithley 2400 source meters under a constant bias configuration.

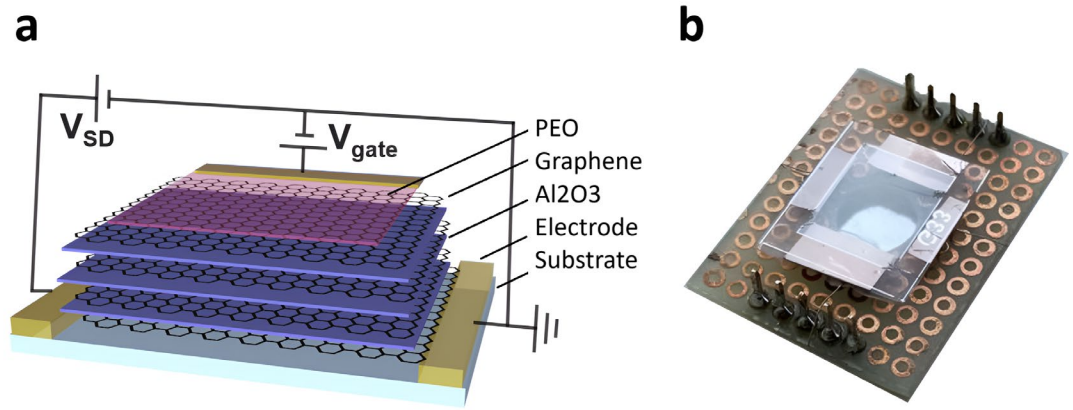

Figure 3.5 a Schematic of the multilayer graphene stack used in electrically gated samples. Graphene layers are spaced using 60 nm-thick Al_2O_3 dielectric layers. The top and bottom graphene sheets are connected to electrodes functioning as source and drain terminals, while gating is achieved via a polymer electrolyte [$LiClO_4$–PEO] layer deposited atop the stack. **b** Photograph of the completed device mounted on a custom PCB designed for simultaneous optical transmission and electrical characterization.Photograph of a completed electrically gated multilayer graphene sample mounted on a custom PCB. The design enables optical access from the rear and electrical contacts for source, drain, and gate terminals.

3.2.3 Graphene oxide sample preparation

In addition to CVD graphene, we fabricated graphene oxide (GO), reduced graphene oxide (rGO), and highly reduced graphene oxide (hrGO) samples for comparative nonlinear optical measurements. To prepare GO samples, a 0.5 mg/mL aqueous dispersion of graphene oxide (Sigma Aldrich) was sonicated for 30 minutes to ensure uniform flake distribution. The solution was then spray-coated onto quartz substrates using a home-built system comprising an airbrush (VH174, VIVOHOME) operating at 30 kPa. The substrates were maintained at 150 °C on a hotplate to facilitate rapid solvent evaporation and promote uniform film formation. A schematic of the spray coating setup used to deposit GO is shown in Fig. 3.6.

For fabrication of rGO, the GO dispersion was chemically treated with hydrazine hydrate (Sigma Aldrich). A solution with a GO:hydrazine volume ratio of 1:0.04 was left at room temperature for 24 hours, resulting in a color change from dark brown to black, indicating chemical reduction. The resulting suspension was then sonicated again at 40 kHz for 30 minutes to promote exfoliation of the rGO layers. hrGO samples were produced by subjecting the rGO films to thermal annealing at 800 °C for 2 hour in a nitrogen atmosphere. This process effectively removes oxygen-containing functional groups and enhances the conductivity and crystallinity of the films. This multi-step fabrication approach allows precise control over GO thickness, reduction level, and structural properties, enabling a systematic investigation of their THz-induced nonlinear optical response. Figure 3.6 shows schematic of the spray coating technique used for GO and rGO film deposition. A dispersion of GO flakes in water is atomized through an airbrush onto a heated substrate placed on a hotplate, enabling solvent evaporation and formation of a uniform GO film [110].

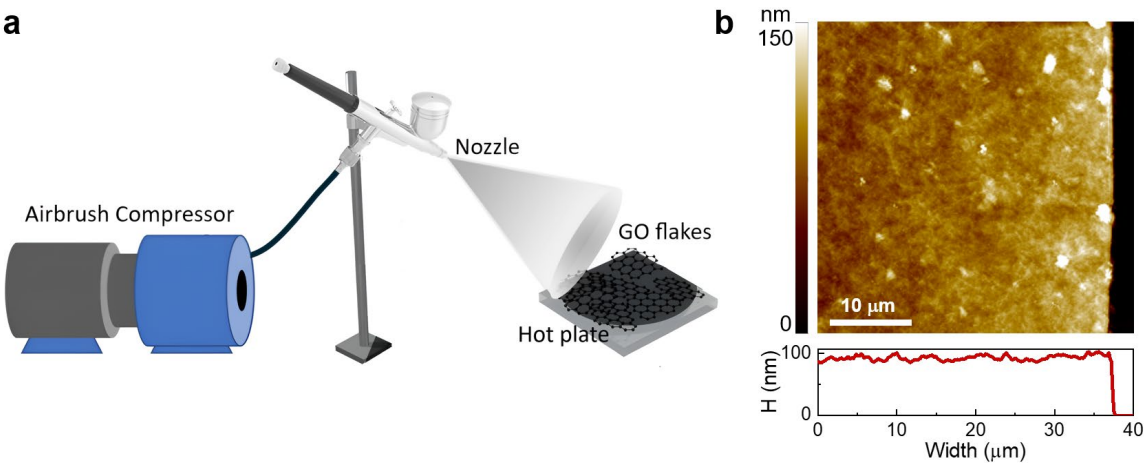

Figure 3.6 a Schematic of the spray coating technique used for GO film deposition. A dispersion of GO flakes in water is atomized through an airbrush onto a heated substrate placed on a hotplate, enabling solvent evaporation and formation of a uniform GO film. **b** AFM image of the spray-coated GO film on a quartz substrate, along with the corresponding height profile.

3.3 Plasmonic metasurfaces

Plasmonic metasurfaces were designed and fabricated to tailor the spatial and spectral properties of THz radiation through engineered resonances and field confinement. Over the course of this research, we designed and implemented a wide variety of plasmonic structures—including bandpass filters, bandstop filters, polarizers, broadband structures, and tailored resonators—each serving a specific functional role depending on the needs of different experiments. These metasurfaces provided not only spectral shaping and polarization control, but also local field enhancement necessary for boosting nonlinear optical interactions, such as third-harmonic generation, especially when integrated with active 2D materials like graphene (chapter 5).

Metasurface fabrication was performed in collaboration with Iridian Spectral Technologies (Ottawa, Canada), leveraging their experience in advanced lithographic techniques and large-area uniform deposition. Both aluminum and gold were employed as the plasmonic metal layers depending on the target resonance and process compatibility. Characterization of fabricated structures was carried out using a suite of nanofabrication and metrology tools including atomic force microscopy (AFM), Dektak profilometry for height measurements, optical microscopy for

pattern fidelity inspection, and Raman spectroscopy to confirm material quality and verify graphene layer integrity post-transfer.

3.3.1 FDTD simulation and design principles

The metasurfaces employed in this study were designed using a 3D finite-difference time-domain (FDTD) solver (Lumerical Inc.) to manipulate THz field profiles and engineer local field enhancements at the target frequency. The simulations modeled the metasurfaces as periodic arrays of metallic elements on a dielectric substrate, incorporating boundary conditions such as perfectly matched layers (PMLs) along the optical axis and periodic boundary conditions in the transverse plane. Mesh sizes as small as 30 nm in the plane of the metasurface and a few nm in the propagation direction were employed to ensure accurate field distribution near sharp metallic features.

3.3.2 Fabrication of metasurface structures

The metasurfaces were fabricated on 188 μm-thick Zeonor substrates via conventional photolithography. A negative lift-off resist was patterned to define the metasurface layout, followed by aluminum deposition (220 nm) via sputtering and lift-off to form the metallic features. High uniformity and reproducibility were confirmed by AFM and optical microscopy. An example of the topography of a fabricated metasurface, captured via AFM, is shown in Fig. 3.7b.

For bilayer metasurface structures, two identical metasurfaces were stacked with a dielectric coupling layer consisting of low-loss, THz-transparent double-sided adhesive films sourced from 3TC and Nitto. Specifically, we used tapes from Nitto Denko Corp. (Osaka) with thicknesses of 10 μm (No. 5601) and 30 μm (No. 5603), and tapes from 3TC (Taichen Corporate (Jiangxi) Co., Ltd.) with thicknesses of 10 μm (J0005) and 15 μm (J0010). These films provided mechanical stability, precise vertical spacing, and excellent optical transparency in the THz regime, ensuring reproducible spectral characteristics across devices between them. Alignment was achieved using a photomask aligner, allowing sub-micron precision in overlaying the structures. This stacking

enables advanced spectral filtering characteristics such as sharp roll-offs and high stopband attenuation as discussed in Chapter 4.

3.3.3 Graphene-metasurface hybrid structures and gating

To study nonlinear optical interactions, multilayer graphene sheets were transferred onto the metasurfaces using the same wet-transfer protocol described earlier. A 60 nm Al_2O_3 spacer layer was first deposited on the metasurface to avoid direct contact between graphene and the metal, minimizing plasmonic quenching and preserving high nonlinear response. Gating was achieved using a spray-coated polymer electrolyte ($LiClO_4$–PEO) applied atop the graphene layers. Source and drain electrodes were connected to the top and bottom graphene sheets, while the gate electrode controlled the carrier density via the electrolyte layer. This configuration enables electrostatic tuning of the optical response. A schematic of the hybrid structure, the mask alignment setup used for metasurface stacking, and an AFM image of a fabricated unit cell are shown in Fig. 3.7b [106].

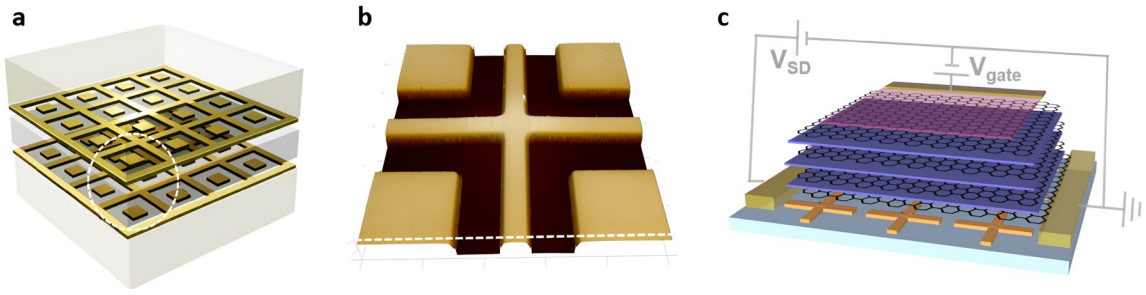

Figure 3.7 a Schematic of the bilayer plasmonic metasurface structure. Two metasurfaces consisting of periodic metallic square-loop arrays deposited on Zeonor substrates are stacked and separated by a dielectric coupling layer composed of a low-loss adhesive tape. **b** 3D atomic force microscope (AFM) image of the unit cell structure fabricated in (a), demonstrating nanoscale feature fidelity. **c** Schematic of the gated graphene–metasurface hybrid structure. Multiple graphene sheets spaced by Al_2O_3 are transferred above the yellow cross-shaped plasmonic metasurface and gated using a polymer electrolyte layer.

Chapter 4

Metamaterial-based THz spectral filters for nonlinear optical experiments

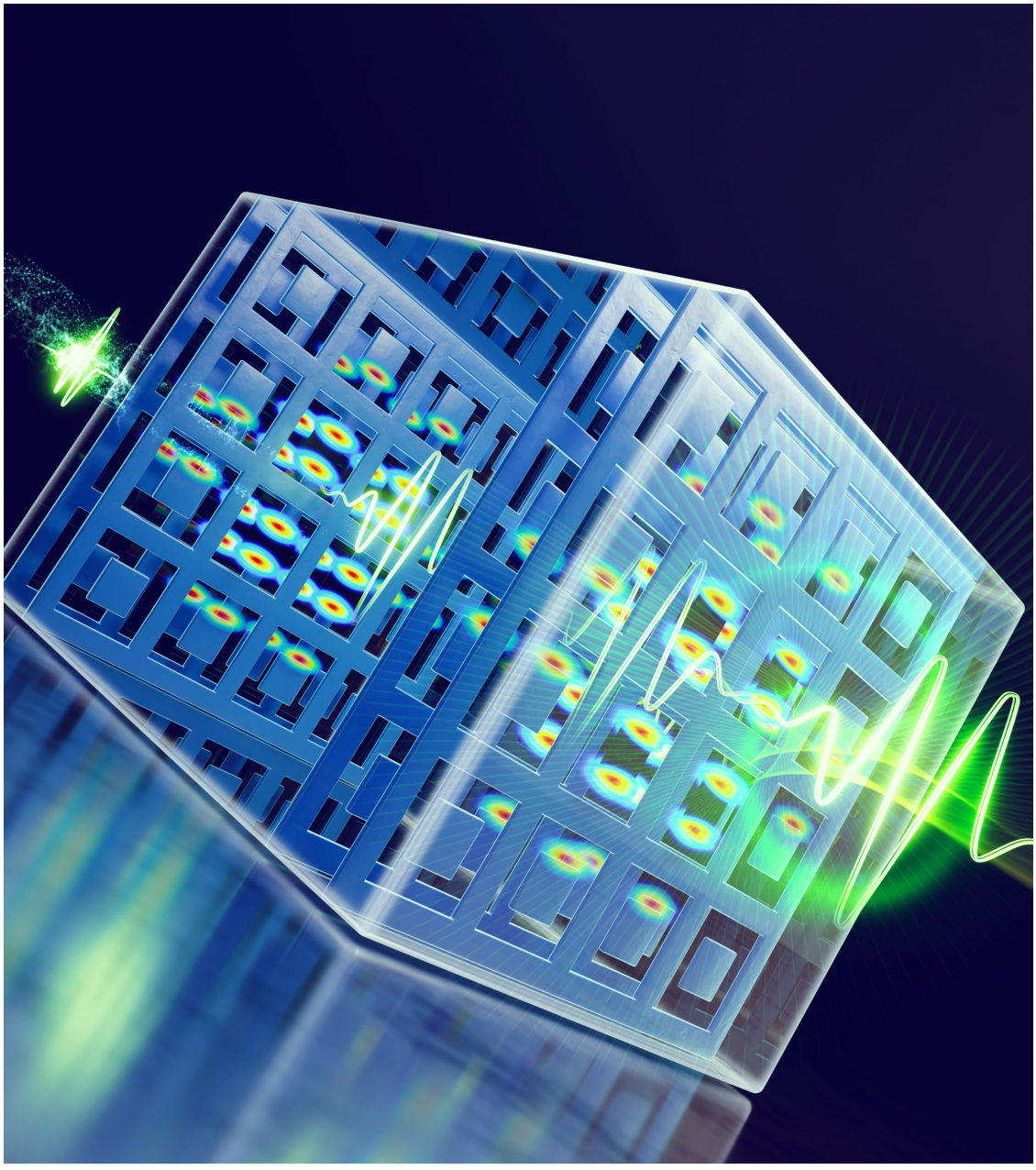

Figure 4.1 Artwork representing a multilayer stacked metasurface structure acting as a THz spectral filter.

4.1 Motivation and experimental challenge

In recent years, there has been significant interest in exploring the nonlinear THz response of two-dimensional materials such as graphene. Landmark studies, including the 2018 work by Hafez *et al.* published in *Nature* [38], demonstrated extremely efficient high-harmonic generation (HHG) in graphene under intense THz excitation. Subsequent works [49,67] extended these findings to complex THz nonlinearities and electrically tunable responses in graphene-based systems. However, all these pioneering experiments relied on advanced accelerator-based THz sources, particularly the TELBE facility in Germany, capable of producing high-field, narrowband THz pulses with excellent signal-to-noise characteristics [111]. TELBE operates using a superconducting radio-frequency (SRF) linear accelerator that generates coherent THz pulses via superradiant emission from ultrashort, high-charge electron bunches passing through diffraction radiators or undulators. This approach enables the production of both broadband and tunable narrowband THz radiation with high field strength and repetition rate [111]. Figure 4.2 compares the performance of various laser-based THz sources with the TELBE facility, a superconducting accelerator-driven source. TELBE exceeds the pulse energy of laser-based systems by more than two orders of magnitude and operates at significantly higher repetition rates, which are critical for achieving superior signal-to-noise ratios in sensitive THz measurements.

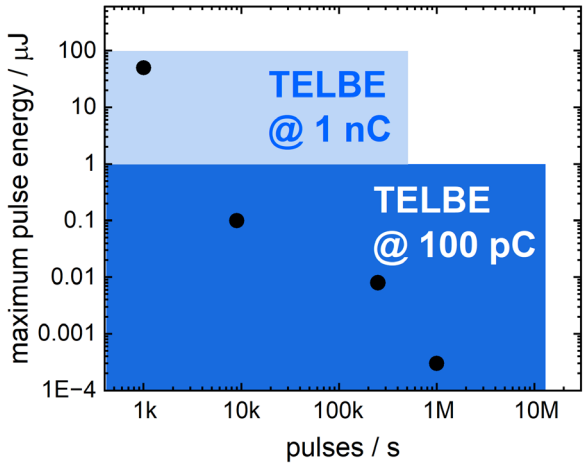

Figure 4.2 Comparison of THz pulse energy versus repetition rate for various laser-based sources (black dots) and the TELBE accelerator-driven facility (blue-shaded). The regions marked TELBE @ 100 pC and TELBE @ 1 nC correspond to different bunch charge operation modes of the TELBE Superconducting Radio-Frequency (SRF) accelerator, with higher charge (1 nC) enabling pulse energies in the 100 µJ regime via enhanced superradiant emission. Figure adapted from [111].

Such facilities, however, are not widely accessible. A major objective of this PhD project was to develop a pathway to perform THz nonlinear optical experiments using conventional table-top THz sources, which are far more accessible and cost-effective. These systems, based on optical rectification, typically generate broadband THz pulses with limited field strength and high background noise—factors that complicate the observation of weak nonlinear signals such as harmonic generation.

4.2 Design strategy: spectral filtering for table-top THz Systems

To address the challenges of broadband excitation and high noise levels inherent in table-top THz sources, a spectral filtering strategy was adopted to tailor the THz field before and after its interaction with the nonlinear sample, as outlined earlier in Section 3.1 (Chapter 3). The key idea is to suppress unnecessary spectral components that carry excess noise, thereby enhancing the detection sensitivity for weak nonlinear signals. Specifically:

- Bandpass filtering was implemented before the sample to isolate the pump frequency and suppress all other spectral components. This ensured that the nonlinear interaction was driven by a well-defined excitation frequency.
- Highpass filtering was applied after the sample to eliminate residual pump light and selectively transmit higher-frequency harmonic signals generated in the material, significantly improving signal-to-noise performance.

Since high-performance commercial filters are scarce in the THz domain—unlike in the optical or microwave regimes—this thesis pursued the custom design and fabrication of THz spectral filters tailored for harmonic generation experiments.

Designing high-performance THz filters suitable for nonlinear optical experiments requires satisfying several critical criteria. An ideal filter must exhibit (i) high transmission within the passband to efficiently deliver the pump pulse to the sample, along with low insertion loss to preserve pulse energy. Equally important is (ii) achieving deep attenuation in the stopband to suppress unwanted spectral components—particularly residual pump fields and broadband background radiation. (iii) Sharp spectral roll-offs between passband and stopband are essential for isolating the pump frequency from generated harmonics. Additionally, (v) the ability to design filters with ultra-broadband performance—such as octave-wide passbands—is highly desirable, particularly for highpass configurations intended to transmit a wide range of high-frequency harmonics generated in nonlinear experiments. Finaly, (iv) practical considerations such as reproducibility in fabrication, mechanical robustness, and compatibility with scalable and cost-effective manufacturing techniques must be addressed. These characteristics are especially important in the THz regime, where commercial filter availability is limited, and custom solutions must often meet demanding experimental specifications.

In this chapter, we focus on the design, simulation, and fabrication of these spectral filters using stacked metasurface architectures. Our approach employed multilayer metamaterial structures, or consisting of identical metasurfaces separated by a precisely defined THz-transparent dielectric spacers. While the single-layer metasurfaces were fabricated in collaboration with Iridian Spectral Technologies, the multilayer stacking strategy—designed and assembled at the University of Ottawa—enabled sharper spectral roll-offs and deeper stopband attenuation compared to single-layer designs. An artist illustration of the multilayer plasmonic metasurface configuration is shown in Fig. 4.2.

These filters serve as enabling tools for our subsequent nonlinear experiments. Over the course of the project, the filter designs were progressively optimized to improve out-of-band attenuation and spectral selectivity. Notably, the attenuation performance improved significantly across different experiments — from approximately 40 dB in the measurements presented in Chapter 5 to nearly 50 dB in the experiments described in Chapter 6. This advancement in filtering performance was critical for suppressing background signals and isolating weak nonlinear responses. In Chapters 5 and 6, we demonstrate how these custom-designed components were instrumental in revealing high-order harmonic signals in graphene and graphene oxide. Their integration was key to improving the sensitivity, selectivity, and robustness of THz-driven nonlinear measurements.

The results of this work have been published in *Photonics Research* [31] (2023) under the title *"Metamaterial-based octave-wide terahertz bandpass filters"* and were also presented at multiple international conferences [112–114]. These documents are reproduced in their published form in the remainder of this chapter.

526 66 Vol. 11, No. 4 / April 2023 / Photonics Research Research Article

PHOTONICS Research

Metamaterial-based octave-wide terahertz bandpass filters

Ali Maleki,[1] Avinash Singh,[1] Ahmed Jaber,[1] Wei Cui,[1] Yongbao Xin,[2] Brian T. Sullivan,[2] Robert W. Boyd,[1,3,4] and Jean-Michel Ménard[1,*]

[1]Department of Physics, University of Ottawa, Ottawa, Ontario K1N 6N5, Canada
[2]Iridian Spectral Technologies Ltd, Ottawa, Ontario K1G 6R8, Canada
[3]School of Electrical Engineering and Computer Science, University of Ottawa, Ottawa, Ontario K1N 6N5, Canada
[4]Institute of Optics and Department of Physics and Astronomy, University of Rochester, Rochester, New York 14627, USA
*Corresponding author: jean-michel.menard@uottawa.ca

Received 8 August 2022; revised 31 January 2023; accepted 31 January 2023; posted 1 February 2023 (Doc. ID 472109); published 9 March 2023

We present octave-wide bandpass filters in the terahertz (THz) region based on bilayer-metamaterial (BLMM) structures. The passband region has a super-Gaussian shape with a maximum transmittance approaching 70% and a typical stopband rejection of 20 dB. The design is based on a metasurface consisting of a metallic square-hole array deposited on a transparent polymer, which is stacked on top of an identical metasurface with a subwavelength separation. The superimposed metasurface structures were designed using finite-difference time-domain (FDTD) simulations and fabricated using a photolithography process. Experimental characterization of these structures between 0.3 and 5.8 THz is performed with a time-domain THz spectroscopy system. Good agreement between experiment and simulation results is observed. We also demonstrated that two superimposed BLMM (2BLMM) devices increase the steepness of the roll-offs to more than 85 dB/octave and enable a superior stopband rejection approaching 40 dB while the maximum transmittance remains above 65%. This work paves the way toward new THz applications, including the detection of THz pulses centered at specific frequencies, and an enhanced time-resolved detection sensitivity toward molecular vibrations that are noise dominated by a strong, off-resonant, driving field.

https://doi.org/10.1364/PRJ.472109

1. INTRODUCTION

Sub-wavelength structures, also referred to as metamaterials, are deemed to play a crucial role for the advancement of terahertz (THz) technologies, notably in the fields of wireless communications [1,2], imaging [3], and signal processing [4]. These structures can be engineered to control several parameters of a THz pulse, such as its spectral amplitude, spatial phase, local field distribution, and polarization state [5,6]. Recently, metamaterials have been used to tune the properties of a THz pulse in both the spectral and temporal domains [7,8]. Other devices such as compact metalenses [9], chemical sensors [10], optical switching modulators [4], and perfect absorbers [11,12] were demonstrated when the metamaterial is confined to a single plane to form a metasurface. Metallic-based THz metasurfaces benefit from relatively low plasmonic loss compared to their counterparts operating in the visible or near-IR regions. More importantly, for many applications, these devices do not require precision nanofabrication tools since the metallic structures are in the range of tens of microns, scaling proportionally with the wavelength of operation, which is 300 μm (at 1 THz). The relatively large feature sizes of metasurfaces allow them to be fabricated with a scalable and cost-effective metal deposition and photolithography techniques. Moreover, metasurface devices fill a special niche for spectral filtering applications in the THz region since multilayered dielectric filters, such as those commonly used in the visible and near-IR regions, would require the deposition of millimeter-thick coatings, which is both costly and technically challenging. Previous works demonstrated that plasmonic modes in the THz region can be used to achieve tunable spectral filters [8], wide bandstops [13], and bandpass spectral filters [14]. Sharp bandpass spectral filters are especially important for signal detection since they can be used to select specific spectral components while rejecting unwanted frequencies that contribute to the noise. In standard time-resolved measurements in which all frequencies are effectively resolved simultaneously, this approach can significantly improve detection sensitivity over a given spectral region [15].

In recent years, multilayered plasmonic metasurfaces have been designed and fabricated to enable new coupled electric or magnetic modes that can contribute to creating broadband

resonances [16–18]. These filtering devices rely on two or more planar periodic arrays of subwavelength structures using different shapes such as rectangles, crosses, or circular-slot structures [13,16,17,19]. They can also include phase-changing materials, such as vanadium dioxide, to achieve tunable spectral properties [20]. The performances of such filters are typically evaluated from three main criteria: (i) the maximum transmission power within a flat passband window, (ii) the rejection efficiency of frequency components in the stopband region, and (iii) the transition between the passband and stopband regions, also referred to as the roll-off, which ultimately allows the device to distinguish desired spectral components from those nearby frequencies that must be blocked. In this paper, the broadband THz filtering properties of a bilayer metamaterial (BLMM) device are demonstrated featuring ~70% flat-top transmittance over an octave-spanning bandwidth. The stopband attenuation is greater than 10 dB over the spectral window of interest (0.3 to 5.8 THz) with some spectral regions featuring more than 20 dB attenuation. This device relies on two identical plasmonic metasurfaces, both based on a square-loop hole periodic array, separated by a transparent polymer ("coupling") layer. The BLMM design is first optimized for broadband transmission in the THz region using numerical FDTD simulations, then fabricated with standard photolithography techniques, and finally characterized using a time-domain THz system. An excellent agreement is observed between the theoretical and experimental results. In addition, it is demonstrated that stacking two BLMMs dramatically improves the rejection efficiency in the stopband region while the maximum transmittance remains relatively unaffected.

2. EXPERIMENT

Figure 1(a) shows a schematic of the BLMM broadband filters, which consist of two identical plasmonic metasurfaces separated by a thin dielectric coupling layer. A photolithography process using a negative lift-off resist to pattern the desired metasurface (square-loop hole arrays) on a 188 μm thick Zeonor substrate (Zeonor is a cyclo-olefin copolymer transparent to THz radiation with a refractive index of $n \sim 1.53$ at 1 THz). Aluminum is next deposited onto the patterned substrate using a sputtering process. It is then followed by a lift-off process that results in the desired metallic square-loop hole arrays that have a fourfold symmetry that ensures a linear optical response independent of the incident polarization state. Figures 1(b) and 1(c) show the topography of the fabricated metasurface as measured with an atomic force microscope (AFM) and an optical microscope, respectively. Depth profile analysis of the structures, as shown in Fig. 1(d), indicates a uniform aluminum thickness of ~220 nm. To create a steeper bandpass fall-off, a "double-cavity" BLMM structure is created using two identical metasurfaces (described above) in which the metasurface layers are separated by a thin dielectric coupling layer. Double-sided tapes are used as dielectric layers, which allows two metasurface devices to easily bind together. Previous work has demonstrated that the spectral properties of bilayered structures are relatively robust to misalignment between the structural elements of the stacked metasurfaces [19,21]. Nonetheless, we used a mask aligner to achieve a submicron positioning of the overlapping square-loop hole pattern to ensure good reproducibility between different samples and optimal agreement between experimental measurements and

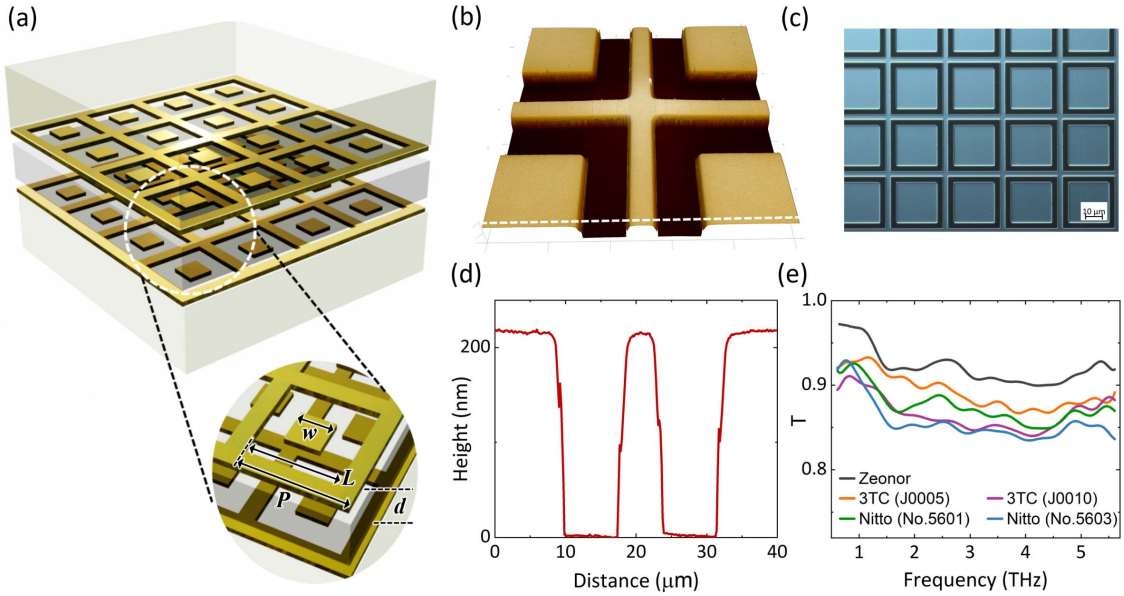

Fig. 1. (a) General schematic of the bilayer-metamaterial (BLMM) bandpass filter. Two plasmonic metasurfaces are placed adjacent to each other separated by a dielectric coupling layer of thickness d. Each metasurface consists of an array of a metallic square-loop hole structure deposited on Zeonor, a THz transparent substrate. The lattice pitch (P), length of the outer square-loop hole (L), and length of the inner square-loop hole (w) of the array are labeled with black arrows. (b) 3D atomic force microscope (AFM) image and (c) optical microscope image of the device S2, and (d) corresponding depth profile indicating a metal depth of ~220 nm. (e) THz power transmittance of the commercial double-sided adhesive tapes from Nitto and 3TC used in the fabrication of the BLMM and 2BLMM devices. In this experiment, the double-sided tapes are laminated on a Zeonor substrate and the spectral transmission measured through that substrate is also displayed (black line).

68

Table 1. Geometrical Parameters of the Broad Bandpass Device[a]

Device	P (μm)	L (μm)	w (μm)	d (μm)	Tape	f_0 (THz)	Δf (THz)
S1	86	80	60	33	No. 5603	0.84	0.58
S2	70	66	48	33	No. 5603	1.00	0.77
S3	52	48	36	23	J0010 and No. 5601	1.46	0.86
S4	29	23	17	10	No. 5601	3.10	1.57
S5	28	24	16	10	No. 5601	3.17	2.02
S6	32	28	15	33	No. 5603	3.44	3.20

[a]P is the lattice pitch, L is the outer square-slot length, w is the inner square-slot length, and d is the distance between two metasurfaces, as shown schematically in Fig. 1(a). The tapes used in the device fabrication are also listed as well as the center frequency (f_0) of the passband region and its spectral bandwidth (FWHM) (Δf).

numerical simulations. The tape is applied manually on the metallic side of a metasurface device while an identical device is positioned and pressed against the first one. We used different tape thicknesses to achieve optimal filtering properties at different THz regions. We are, however, limited to the thickness offered by commercial suppliers. In this work, we used tapes from Nitto Denko Corp. (Osaka) with thicknesses of 10 μm (No. 5601) and 33 μm (No. 5603), and tapes from 3TC [Taichen Corporate (Jiangxi) Co., Ltd.] with thicknesses of 9 μm (J0005) and 13 μm (J0010). Table 1 catalogs their use in the different devices presented in this work. The thickness of the tapes is measured with a profilometer (Dektak, Bruker, Billerica) and its THz absorption is characterized with time-resolved THz measurements. Figure 1(e) shows the THz spectral transmission of different tapes laminated on a Zeonor substrate as well as the one measured with the bare substrate (labeled as Zeonor).

The BLMM devices are characterized using time-domain THz spectroscopy. The experimental setup relies on an optical source delivering 60 fs pulses centered at a wavelength of 1030 nm [22,23]. Optical rectification in a 200 μm thick 110-orientated GaP crystal generates broadband THz transients detected by electro-optic sampling relying on an identical nonlinear detection crystal. Numerical simulations are performed with a 3D finite-difference time-domain (FDTD) solver (Lumerical Inc.) to investigate and optimize the target design parameters and achieve the desired broadband filtering properties in the THz region. As shown in the inset of Fig. 1(a), the geometry of the metallic structure is defined from its lattice pitch (P), length of the outer square-loop hole (L), length of the inner square-loop hole (w), and the thickness of the dielectric coupling layer (d) separating the two metasurfaces. We modeled the tape as a lossy dielectric layer with a real part and an imaginary part of the refractive index corresponding to $n = 1.65$ and $k = 0.003$, respectively, which are, within a small uncertainty, the frequency-independent values obtained with time-resolved THz spectroscopy for all tape samples. Periodic boundary conditions along the in-plane axes are employed in the simulations as well as a perfectly matched layer (PML), which is applied in the direction of optical propagation to absorb all incident fields and prevent reflection at that interface.

The geometrical dimensions shown in Table 1 were determined using numerical simulations to obtain a broad, sharp, and symmetrical bandpass region centered at different frequencies. Due to scale invariance, decreasing the size of all geometrical parameters by the same amount proportionally shifts the device's transmittance profile to shorter wavelengths (higher frequencies). The structures S1, S2, and S3 are based on a common metasurface design displaying similar ratios between geometrical parameters. As a result, these three filters display similar properties in terms of bandwidth, roll-offs, and overall transmittance profile. Limitations in the wafer-size photolithography process prevented using the same filter design at higher frequencies since defects and spatial homogeneity across the devices play a larger role as the structure parameters are decreased. More specifically, it was established that the minimum feature sizes of P–L should not be less than 4 μm. The devices S4, S5, and S6 are therefore designed using a different model to explore filtering properties centered around 3 THz, while ensuring the minimum feature is large enough to ensure the fabrication of high-quality samples. Note that the coupling parameter d cannot be fully controlled because it is based on the thickness of the adhesive region between the two metasurfaces.

3. RESULTS AND DISCUSSION

A. Spectral Filtering Performances

The metasurface geometry used for the fabrication of six BLMM devices, labelled S1 to S6, is presented in Table 1. Figures 2(a) and 2(b) show that the measured THz transmission spectrum (circles) corresponding to each structure is in good agreement with FDTD simulation results (solid lines). We find that the ratio between the highest and lowest frequencies at half the maximum of the transmittance corresponds to 2, 2.2, 1.9, 1.7, 1.9, and 2.8 for the devices S1 to S6, respectively. Therefore, the BLMM designs demonstrate an FWHM bandwidth that corresponds to approximately one octave (or a factor of 2). The transmittance spectra exhibit a super-Gaussian shape with a measured transmittance >70% in the passband region. This relatively high transmittance is partially attributable to the weak Fresnel reflection at the air–polymer interface, which is significantly lower than that typically observed at an air–semiconductor interface [8]. Additionally, the BLMM devices exhibit steep roll-offs (as measured from the high-frequency side of the passband) of >50 dB/octave and up to 100 dB/octave for S6. Such roll-off values are larger than those reported for other double-layered metamaterial devices based on structures such as skewed circular slot rings (30.2 dB/octave), meandered slots (44.6 dB/octave), and Jerusalem cross slots (58.3 dB/octave) [19]. These roll-offs are also comparable to those reported for more complex multilayered metamaterial structures [24]. As shown in Fig. 2(b) for S1, S2, and S3, such

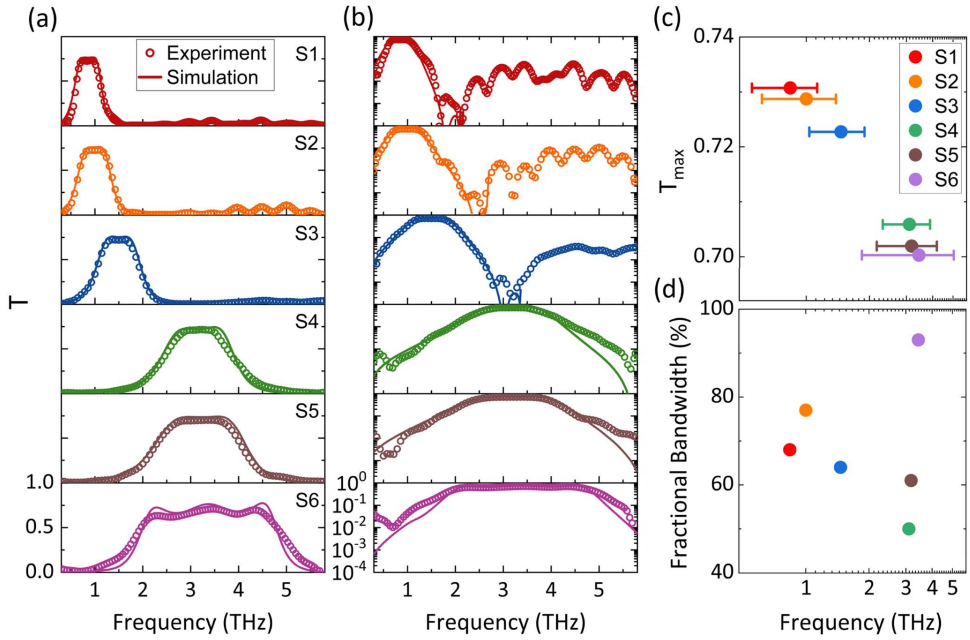

Fig. 2. THz measured (circles) and simulated (solid lines) transmittance spectrum of the BLMM-based broad bandpass filters in (a) linear scale and (b) semi-logarithmic scale. Experiments are performed with a time-domain THz spectroscopy system and are in good agreement with FDTD simulation results. (c) Measured maximum transmission (T_{max}) of the structures over center frequency in semilogarithmic scale, in which error bars present the corresponding octave-spanning FWHM linewidth. (d) Calculated fractional bandwidth (in percentage) of all BLMM devices over frequency for the experiment results.

a roll-off leads to a significant transmittance suppression, approaching 30 dB within an octave of the central transmitted frequency. Furthermore, the attenuation of these devices remains relatively high (>10 dB) at frequencies extending beyond an octave from the passband region. Figure 2(c) shows the measured maximum transmittance (T_{max}) of the six devices as a function of frequency, in which circles indicate the center frequency of the passband filters and horizontal lines correspond to the FWHM linewidth of the devices. Another figure of merit used to characterize bandpass filters is the fractional bandwidth (FBW) defined as the absolute bandwidth at FWHM divided by the central frequency. As shown in Fig. 2(d), our structures feature an FBW > 50%, and up to 93% for S6, which is, to the best of our knowledge, the largest FBW reported for a THz bandpass filter. Compared to single-layer metasurface structures, the BLMM design provides a broad bandpass region with higher attenuation in the stopband region, a flatter passband, and steeper roll-offs [25–27].

B. 3D Numerical Simulations

2D maps of the electric field spatial distribution and surface current distribution on the metallic layer of the structure S5 are shown in Fig. 3. Focusing on the spectral components within the bandpass region of the filter, Fig. 3(a) shows a

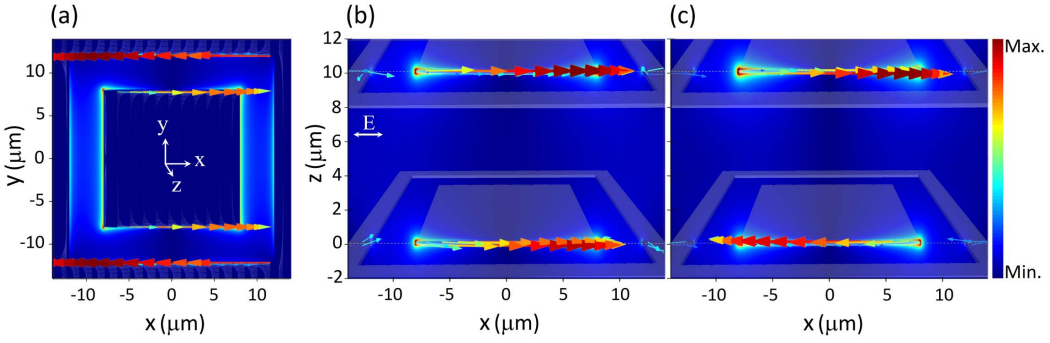

Fig. 3. Normalized electric field amplitude distribution of the BLMM structure S5. The arrows indicate surface current distribution within one period of the array. (a) Top view distribution in x–y plane at the surface of the bottom layer plasmonic structure ($z = 0.2$ μm) at the frequency of 2.9 THz. (b) and (c) Side view of the electrical field distribution and direction in the x–z plane, corresponding to a 2D cross section taken at $y = -8$ μm at a frequency of 2.9 THz and 3.6 THz, respectively. The gray 3D schematics in (b) and (c) illustrate the simulated unit cell of the stacked metasurfaces. The incident THz wave propagates in the z direction and is polarized along the x direction.

top view of the device with localized surface resonances at 2.9 THz. A field enhancement of 26 (relative to the incoming field amplitude) is observed at the corners of the central square structure along with an anisotropic field distribution with higher field amplitudes along the lateral sides of the structures due to the incident horizontal polarization. Electrical currents are induced at the outer edge of the central square and the inner edge of the surrounding frame with similar magnitude but opposite directions. Figures 3(b) and 3(c) show a cross section of the electric field amplitude and direction at frequencies of 2.9 and 3.6 THz, respectively, corresponding to the boundaries of the filter passband region. This side view is taken at the edge of the inner square structures with a 3D schematic of the unit cell (in gray) superimposed. Spectral filters relying on stacked metasurfaces are able to support effective cavity modes dominated by electric dipole resonances, magnetic dipole resonances, and standing-wave-like resonances, as previously discussed in the literature [13,16,17,19,28,29]. In Fig. 3(b), the symmetric oscillation of the induced current in the top and bottom layers indicates an electric dipole resonance. At a slightly upshifted frequency, Fig. 3(c) shows an antisymmetric resonance where electrical currents in the top and bottom layers oscillate in opposite directions. Such a mode is related to a magnetic dipolar resonance. It is the interference between these two modes, also referred to as trapped modes [29,30], that leads to such a broad and sharp passband region centered at 3.1 THz. Note that the surrounding frame creates a standing-wave-like resonance, which increases the absorption in the stopband region [16,19].

C. 2BLMM Design

To create devices with improved spectral-filtering performances, two BLMMs were joined together with a thin adhesive film (3TC-J0005) to fabricate a 2BLMM device shown schematically in Fig. 4(a). Based on the thickness of the Zeonor substrate and the adhesive film, the two BLMM structures are separated by a distance $D = 386$ μm, which is large enough to prevent near-field effects. The configuration is therefore independent of the relative cross structure alignment and orientation. We compare in Figs. 4(b) and 4(c) the THz transmittance measured with S2 and S4 as individual BLMM devices (blue curves) and the transmission measured in a 2BLMM configuration (orange curves). The 2BLMM devices show improved filtering performances in terms of the background attenuation. The stopband region, for example, provides stronger signal attenuation by approximately two orders of magnitude (dotted lines). In addition, the roll-offs (as measured from the high-frequency side) now correspond to 86 dB/octave and 85 dB/octave for S2-2BLMM and S4-2BLMM, respectively, an improvement corresponding roughly to the square value of the roll-offs measured with the corresponding BLMM devices. This stronger stopband attenuation and the sharper transitions between the passband and stopband regions are consistent with a design based on two independent BLMMs, where the transmittance spectrum then corresponds to the square transmittance of a single device. There are, however, significant advantages in stacking and binding the two BLMMs. First, the maximum transmittance in the passband region is kept relatively high (>65%) because there is no air gap, thus avoiding

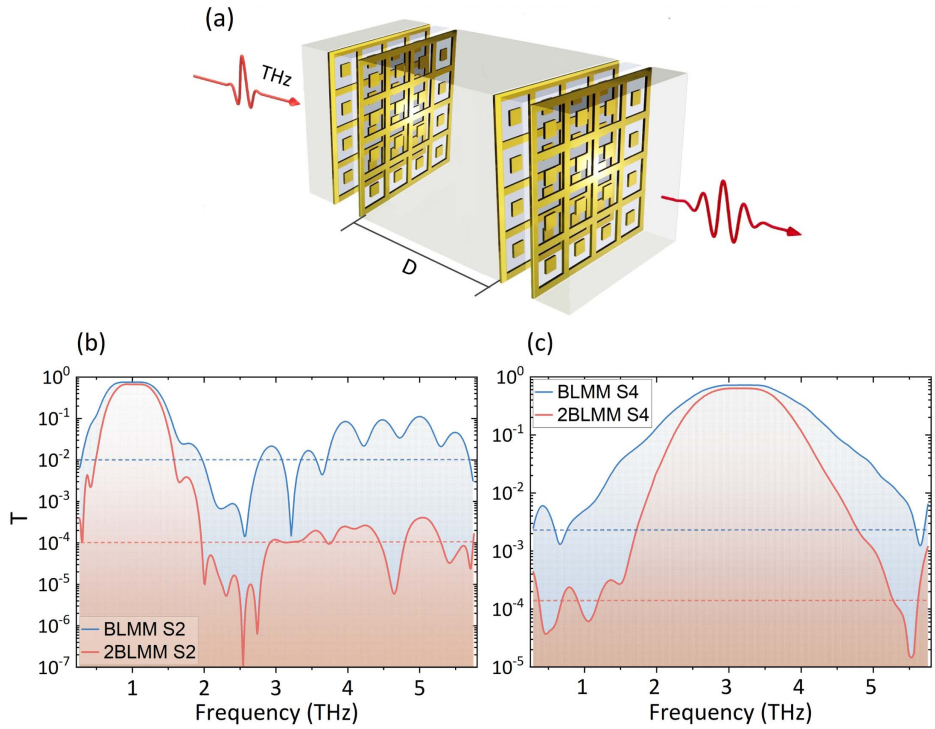

Fig. 4. (a) Schematic of the 2BLMM devices fabricated from two BLMM structures bound together with double-sided tape (separated by a length D). Comparison of the measured THz transmission of the BLMM (blue curve) and 2BLMM (orange curve) devices for (b) S2 and (c) S4. Dotted lines show the averaged attenuation floor.

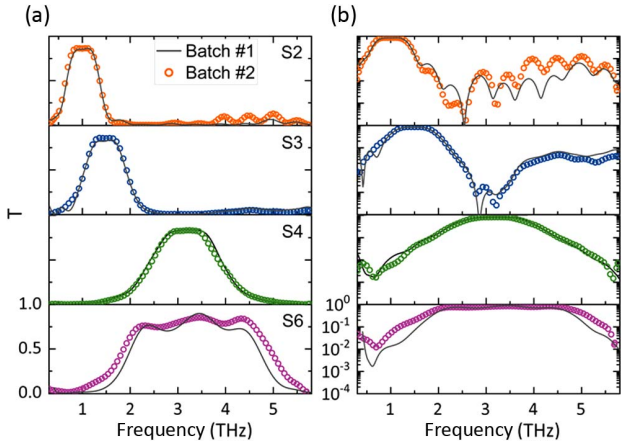

Fig. 5. Measured THz transmittance spectrum of two batches (lines and circles) of the BLMM-based broad bandpass filters in (a) linear scale and (b) semi-logarithmic scale. There is a good repeatability between the pairs of S2, S3, S4, and S6 devices fabricated in two batches and characterized on two different days.

additional Fresnel reflections. A stronger than expected attenuation also is observed in the stopband region. For S2, the transmittance between 4 and 5.5 THz is reduced from 10^{-1} to $<5 \times 10^{-4}$ (or 10 dB to 33 dB) when using a 2BLMM geometry, which exceeds the expected signal reduction based on a square dependence. This enhanced signal reduction in the stopband region may be indicative of a dipole interaction between the two BLMM devices inducing a new coupled mode that contributes to reducing transmittance across this spectral region.

D. Device Fabrication Repeatability

To test the repeatability of the fabrication process of the BLMM devices, we fabricated two sets of samples on two different days. Figure 5 shows the measured transmittance spectra for the two distinct devices based on the S2, S3, S4, and S6 designs. The pairs of S2, S3, and S4 devices are nearly indistinguishable on a linear scale [Fig. 5(a)], while a small (7%) difference in bandpass bandwidth (FWHM) can be seen for S6. This study indicates a reliable fabrication process and good repeatability. The small disparity could be due to misalignments when attaching the two metasurfaces together, or some minor variations of the metasurface structure due to the photolithography process. The S6 device is expected to be more susceptible to these variations because of its smaller feature sizes.

E. Comparison to Previous Work

We have compared the filtering performance of our devices with similar reported THz spectral filters also relying on a pair of coupled metasurfaces (see Table 2). Our BLMM and 2BLMM devices based on square hole slot metasurfaces can feature a relatively large bandpass region, sharp roll-offs, high fractional bandwidths, and a strong attenuation in the stopband region. Those are among the most critical properties of a bandpass filter. Furthermore, our design can support a bandpass centered at higher frequencies, while the structures presented in most previous work on THz filters were designed for the low frequency region (<2 THz) [16,19,21,24]. Finally, we report a stopband region extending over an unprecedentedly large spectral region. For example, device S1, which has a peak transmission around 0.9 THz, blocks spectral components between 1.5 and 6 THz, by more than 30 dB.

4. CONCLUSION

We have designed and experimentally demonstrated six bilayer metamaterial (BLMM) devices with THz bandpass filtering properties. These devices feature a flat passband region centered at different frequencies, with a maximum transmittance exceeding 70% and a large spectral bandwidth corresponding to approximately one octave. The transmittance spectrum has a super-Gaussian profile featuring steep roll-offs, while the stopband region offers a strong signal suppression (generally >20 dB) and likely extends much beyond the investigated spectral region of 0.3 to 5.8 THz. Experimental measurements and FDTD simulations are in good agreement. The fabrication of the BLMM devices is relatively straightforward because it relies on a standard photolithography process. Furthermore, it has been demonstrated that 2BLMM devices can be joined together to improve the spectral filtering selectivity. This 2BLMM configuration significantly enhances the signal suppression in the stopband region while the transmission remains flat and high (>65%). We believe this type of filter design will play a major role in selecting THz signals contained within a known spectral region to notably enable sensitive wireless communications systems [2]. In time-domain spectroscopy, spectral filtering can also lead to significant improvement of the SNR by notably blocking spectral components necessary to drive a nonlinear system while investigating the signal at higher harmonics [15].

Table 2. Performance Comparison of the Filters Presented in This Work to Similar Structures Based on Layered Metasurfaces Reported in the Literature

Study	Structure	Bandpass FWHM (THz)	Roll-off (dB/octave)	FBW (%)	Attenuation (dB)
Current designs	Square-loop hole	0.5–3.2	50–100	50–93	30–50
Ref. [19]	Skewed circular slot	0.85	30.2	51.7	~7
Ref. [19]	Meandered slots	0.45	44.6	60	~10
Ref. [19]	Jerusalem cross slots	0.45	58.3	82.2	~10
Ref. [21]	Square slot (fishnet)	0.4	–	~37	~15
Ref. [24]	Cross slot	0.69	~74	~76	30
Ref. [16]	Custom-shape slot	0.47	~65	~67	30

Funding. Natural Sciences and Engineering Research Council of Canada (RGPIN-2016-04797, STPGP/521619-2018); Canada Foundation for Innovation (35269).

Acknowledgment. The authors would like to thank Ksenia Dolgaleva and Orad Reshef for insightful discussions. Ali Maleki acknowledges support from the Ontario Graduate Scholarship (OGS), the University of Ottawa Excellence Scholarship, and the University of Ottawa International Experience Scholarship.

Disclosures. The authors declare no conflicts of interest.

Data Availability. Data underlying the results presented in this paper are not publicly available at this time but may be obtained from the authors upon reasonable request.

REFERENCES

1. H. Sarieddeen, N. Saeed, T. Y. Al-Naffouri, and M. S. Alouini, "Next generation terahertz communications: a rendezvous of sensing, imaging, and localization," IEEE Commun. Mag. **58**, 69–75 (2020).
2. Y. Ghasempour, R. Shrestha, A. Charous, E. Knightly, and D. M. Mittleman, "Single-shot link discovery for terahertz wireless networks," Nat. Commun. **11**, 2017 (2020).
3. I. E. Carranza, J. Grant, J. Gough, and D. R. S. Cumming, "Metamaterial-based terahertz imaging," IEEE Trans. Terahertz Sci. Technol. **5**, 892–901 (2015).
4. L. Wang, Y. Zhang, X. Guo, T. Chen, H. Liang, X. Hao, X. Hou, W. Kou, Y. Zhao, T. Zhou, S. Liang, and Z. Yang, "A review of THz modulators with dynamic tunable metasurfaces," Nanomaterials **9**, 965 (2019).
5. H. W. Tian, H. Y. Shen, X. G. Zhang, X. Li, W. X. Jiang, and T. J. Cui, "Terahertz metasurfaces: toward multifunctional and programmable wave manipulation," Front. Phys. **8**, 584077 (2020).
6. J. He, X. He, T. Dong, S. Wang, M. Fu, and Y. Zhang, "Recent progress and applications of terahertz metamaterials," J. Phys. D **55**, 123002 (2022).
7. L. Gingras, W. Cui, A. W. Schiff-Kearn, J.-M. Ménard, and D. G. Cooke, "Active phase control of terahertz pulses using a dynamic waveguide," Opt. Express **26**, 13876–13882 (2018).
8. L. Gingras, A. Jaber, A. Maleki, O. Reshef, K. Dolgaleva, R. W. Boyd, and J.-M. Ménard, "Ultrafast modulation of the spectral filtering properties of a THz metasurface," Opt. Express **28**, 20296–20304 (2020).
9. J. He, J. Ye, X. Wang, Q. Kan, and Y. Zhang, "A broadband terahertz ultrathin multi-focus lens," Sci. Rep. **6**, 28800 (2016).
10. S. Shen, X. Liu, Y. Shen, J. Qu, E. Pickwell-MacPherson, X. Wei, and Y. Sun, "Recent advances in the development of materials for terahertz metamaterial sensing," Adv. Opt. Mater. **10**, 2101008 (2022).
11. D. Das, K. Bhattacharyya, and S. Baruah, "A review of terahertz technology and metamaterial based electromagnetic absorber at terahertz band," ADBU J. Eng. Technol. **9**, 009020638 (2020).
12. M. Kenney, J. Grant, Y. D. Shah, I. Escorcia-Carranza, M. Humphreys, and D. R. S. Cumming, "Octave-spanning broadband absorption of terahertz light using metasurface fractal-cross absorbers," ACS Photon. **4**, 2604–2612 (2017).
13. Q. Zeng, Y. Huang, S. Zhong, T. Lin, Y. Zhong, Z. Zhang, Y. Yu, and Z. Peng, "Multiple resonances induced terahertz broadband filtering in a bilayer metamaterial," Front. Phys. **10**, 857422 (2022).
14. Y. Huang, T. Okatani, and Y. Kanamori, "Broadband stop filters for THz waves using H-shaped metamaterials with dual electronic-plasmonic functionality," Jpn. J. Appl. Phys. **61**, 1007 (2022).
15. J. C. Deinert, D. Alcaraz Iranzo, R. Pérez, X. Jia, H. A. Hafez, I. Ilyakov, N. Awari, M. Chen, M. Bawatna, A. N. Ponomaryov, S. Germanskiy, M. Bonn, F. H. L. Koppens, D. Turchinovich, M. Gensch, S. Kovalev, and K. J. Tielrooij, "Grating-graphene metamaterial as a platform for terahertz nonlinear photonics," ACS Nano **15**, 1145–1154 (2021).
16. L. J. Liang, J. Q. Yao, and X. Yan, "Ultrabroad terahertz bandpass filter based on a multiple-layered metamaterial with flexible substrates," Chin. Phys. Lett. **29**, 64–67 (2012).
17. M. Khodaee, M. Banakermani, and H. Baghban, "GaN-based metamaterial terahertz bandpass filter design: tunability and ultra-broad passband attainment," Appl. Opt. **54**, 8617–8624 (2015).
18. M. Lu, W. Li, and E. R. Brown, "Second-order bandpass terahertz filter achieved by multilayer complementary metamaterial structures," Opt. Lett. **36**, 1071–1073 (2011).
19. T.-T. Yeh, S. Genovesi, A. Monorchio, E. Prati, F. Costa, T.-Y. Huang, and T.-J. Yen, "Ultra-broad and sharp-transition bandpass terahertz filters by hybridizing multiple resonances mode in monolithic metamaterials," Opt. Express **20**, 7580–7589 (2012).
20. J. Huang, J. Li, Y. Yang, J. Li, J. Li, Y. Zhang, and J. Yao, "Active controllable bandwidth of THz metamaterial bandpass filter based on vanadium dioxide," Opt. Commun. **465**, 125616 (2020).
21. J. S. Li, Y. Li, and L. Zhang, "Terahertz bandpass filter based on frequency selective surface," IEEE Photon. Technol. Lett. **30**, 238–241 (2018).
22. A. Halpin, N. Couture, and J.-M. Ménard, "Optical pulse structuring in gas-filled hollow-core Kagomé PCF for generation and detection of phase-locked multi-THz pulses [Invited]," Opt. Mater. Express **9**, 3115 (2019).
23. W. Cui, A. W. Schiff-Kearn, E. Zhang, N. Couture, F. Tani, D. Novoa, P. S. J. Russell, and J. M. Ménard, "Broadband and tunable time-resolved THz system using argon-filled hollow-core photonic crystal fiber," APL Photon. **3**, 111301 (2018).
24. L. Liang, B. Jin, J. Wu, Y. Huang, Z. Ye, X. Huang, D. Zhou, G. Wang, X. Jia, H. Lu, L. Kang, W. Xu, J. Chen, and P. Wu, "A flexible wideband bandpass terahertz filter using multi-layer metamaterials," Appl. Phys. B **113**, 285–290 (2013).
25. D. Sun, L. Qi, and Z. Liu, "Terahertz broadband filter and electromagnetically induced transparency structure with complementary metasurface," Results Phys. **16**, 102887 (2020).
26. H. Sun, L. Zhao, J. Dai, Y. Liang, J. Guo, H. Meng, H. Liu, Q. Dai, and Z. Wei, "Broadband filter and adjustable extinction ratio modulator based on metal-graphene hybrid metamaterials," Nanomaterials **10**, 1359 (2020).
27. H.-T. Chen, J. F. O'Hara, A. J. Taylor, R. D. Averitt, C. Highstrete, M. Lee, and W. J. Padilla, "Complementary planar terahertz metamaterials," Opt. Express **15**, 1084–1095 (2007).
28. J. C. Yan, Z. K. Li, Y. Zhang, Y. L. Wang, and C. P. Huang, "Trapped-mode resonances in all-metallic metasurfaces comprising rectangular-hole dimers with broken symmetry," J. Appl. Phys. **126**, 213102 (2019).
29. O. Paul, R. Beigang, and M. Rahm, "Highly selective terahertz bandpass filters based on trapped mode excitation," Opt. Express **17**, 18590–18595 (2009).
30. V. A. Fedotov, M. Rose, S. L. Prosvirnin, N. Papasimakis, and N. I. Zheludev, "Sharp trapped-mode resonances in planar metamaterials with a broken structural symmetry," Phys. Rev. Lett. **99**, 5–8 (2007).

Chapter 5

Strategies to enhance third-harmonic generation in graphene-metamaterial architecture

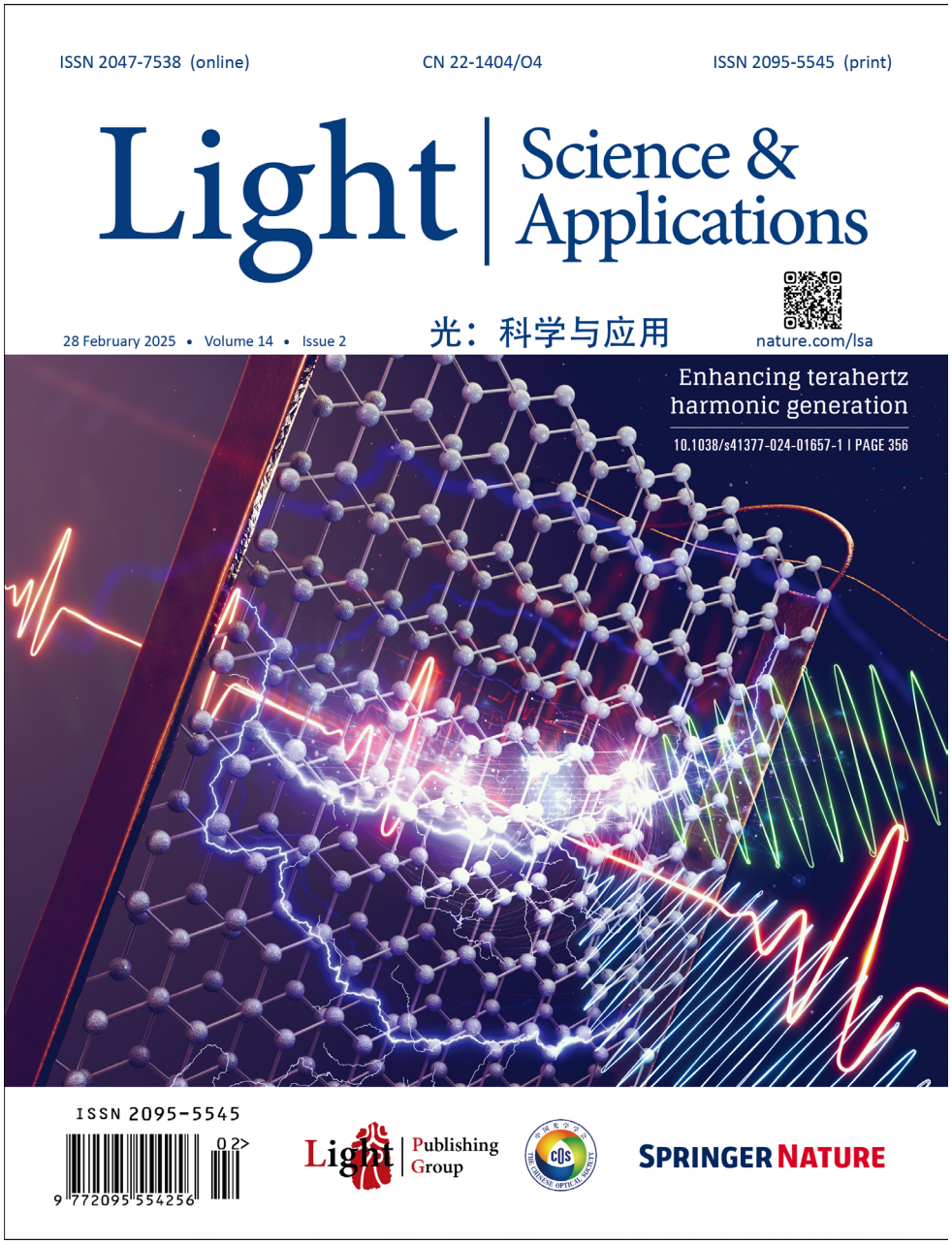

Figure 5.1 Cover image of *Light: Science & Applications* (Vol. 14, 2025), featuring our work on enhancing THz harmonic generation in graphene [47].

In Chapter 4, we demonstrated the design and fabrication of custom THz spectral filters with octave-wide bandpass characteristics. These filters exhibit flat passband regions with maximum transmittance exceeding 60%, sharp spectral roll-offs, and strong signal suppression in the stopband (generally greater than 40 dB) [31]. In this chapter, we integrate these components into our tilted-pulse-front table-top THz source to explore and enhance nonlinear optical responses in graphene. Specifically, we employ a combination of a bandpass filter (BPF) and a highpass filter (HPF)—as discussed in Chapter 3—to enable sensitive detection of third-harmonic generation (THG). The BPF is positioned before the sample to isolate the fundamental frequency, while the HPF is placed after the sample to suppress residual pump noise and transmit only the higher-frequency harmonic signals.

Graphene's extraordinary properties make it a promising material for a wide range of optoelectronic applications [48]. Its large third-order optical nonlinearity, broadband response, and ease of integration render it particularly attractive for all-optical switching and frequency conversion. In the THz regime, graphene exhibits an exceptionally high third-order nonlinear susceptibility—on the order of $\chi^{(3)} \sim 10^{-9} m^2 / V^2$ [38]. However, a key challenge lies in the atomically thin nature of monolayer graphene, which limits the overall interaction length and results in relatively weak nonlinear signal generation. This limitation presents a significant obstacle to the practical use of graphene in THz frequency conversion devices. To overcome this, our work implements three distinct strategies to enhance third-harmonic generation:

1. **Multilayer stacking**: We stack multiple CVD-grown graphene layers, separated by thin dielectric spacers to reduce interlayer coupling. This approach increases the effective light–matter interaction length. For up to six layers, we observe enhancement factors as high as 33× in THG power compared to a monolayer. To understand and quantify this enhancement, we use a semi-analytical model that accounts for pump and third harmonic absorption across the stacked layers. The model includes layer-by-layer absorption using experimentally extracted coefficients based on

Beer–Lambert law and is validated through FDTD simulations (see Supplementary Information, Section S1). These absorption values are derived from measured and simulated transmission data. This framework allows us to realistically capture the nonlinear response and saturation behavior in multilayer graphene structures.

2. **Electrostatic gating**: By applying a gate voltage via a polymer electrolyte layer, we modulate the carrier density in the graphene. This allows us to optimize the nonlinear conductivity by tuning the Fermi level away from the charge neutrality point, where nonlinear interactions are suppressed.
3. **Plasmonic metasurfaces**: We utilize THz metasurface substrates to locally enhance the pump electric field at the graphene interface. Metasurface types explored include bandstop filters (BSF), bandpass filters (BPF), and wire-grid polarizers (WGP). Among these, BSF-based metasurfaces exhibit the highest enhancement, as confirmed by numerical simulations and experimental measurements.

These findings are presented in our article: "Strategies to enhance THz harmonic generation combining multilayered, gated, and metamaterial-based architectures" *Light: Science & Applications*, Vol. 14, Article 44 (2025) [47].

This publication was honored by being featured on the cover page of *Light: Science & Applications* (see Fig. 5.1) and was selected as an Editor's Highlight, recognizing its contribution to the advancement of nonlinear THz photonics. The results have also been presented at international conferences [115,116].

The full published article, along with its supplementary information, is reproduced in the following pages.

Official journal of the CIOMP 2047-7538
www.nature.com/lsa

ARTICLE Open Access

Strategies to enhance THz harmonic generation combining multilayered, gated, and metamaterial-based architectures

Ali Maleki[1], Moritz B. Heindl[2], Yongbao Xin[3], Robert W. Boyd[1,4,5], Georg Herink[2] and Jean-Michel Ménard[1,4]✉

Abstract

Graphene has unique properties paving the way for groundbreaking future applications. Its large optical nonlinearity and ease of integration in devices notably makes it an ideal candidate to become a key component for all-optical switching and frequency conversion applications. In the terahertz (THz) region, various approaches have been independently demonstrated to optimize the nonlinear effects in graphene, addressing a critical limitation arising from the atomically thin interaction length. Here, we demonstrate sample architectures that combine strategies to enhance THz nonlinearities in graphene-based structures. We achieve this by increasing the interaction length through a multilayered design, controlling carrier density with an electrical gate, and modulating the THz field spatial distribution with a metallic metasurface substrate. Our study specifically investigates third harmonic generation (THG) using a table-top high-field THz source. We measure THG enhancement factors exceeding thirty and propose architectures capable of achieving a two-order-of-magnitude increase. These findings underscore the potential of engineered graphene-based structures in advancing THz frequency conversion technologies for signal processing and wireless communication applications.

Introduction

Nonlinear optics in the terahertz (THz) region has emerged as a promising field with diverse scientific and technological applications, fostering innovations in optical devices, advancements in material analysis, and imaging[1–3]. Intense THz fields interacting with nonlinear materials offer pathways for fundamental insights, from studying solid-state materials to capturing carrier and phonon dynamics[4–6]. To enable ultrahigh-speed information and communication technologies, many efforts are also invested to achieve efficient nonlinear THz frequency converters[7]. An archetypal illustration of this process is high harmonic generation (HHG), where resulting photons are generated at energies corresponding to multiples of the incident photons' energy[8].

Recent years have witnessed a broadening landscape of efficient THz HHG platforms relying on various materials. They include superconductors[9,10], transition metal oxides (such as $CaRuO_3$)[11], bulk semiconductors[12], and most notably, Dirac fermion systems. Dirac electronic band structures exhibit a linear energy-momentum dispersion that has been associated with a strong nonlinear response at THz frequencies. These effects have been studied in different material geometries, such as one-dimensional (1D) massless Dirac systems (e.g. carbon nanotubes)[13], 2D semimetals and topological insulators (e.g. Bi_2Se_3)[14–16], and 3D Dirac semimetals (e.g. Cd_3As_2)[17]. HHG in 2D Dirac-fermion graphene[18] has been reported across a wide spectral range, from the near-infrared[19], to the mid-infrared[20–22] and the THz[23–25] regions. One contribution to the optical nonlinearity of graphene can be closely linked to the transport dynamics of its carriers in response to an applied electric field. Unlike visible or NIR excitations leading to interband transitions, a THz driving field causes intraband transitions. As free carriers absorb energy through Drude absorption, this energy is

Correspondence: Jean-Michel Ménard (jean-michel.menard@uottawa.ca)
[1]Department of Physics, University of Ottawa, Ottawa, ON K1N 6N5, Canada
[2]Experimental Physics VIII – Ultrafast Dynamics, University of Bayreuth, Bayreuth 95447, Germany
Full list of author information is available at the end of the article

redistributed, increasing the free-carrier temperature (exceeding 1000 K at THz field strength of 20 kV/cm)[26] due to graphene's low electronic heat capacity. This rise in temperature reduces THz conductivity and absorption, leading to a heating-cooling cycle that creates strong thermodynamic nonlinearity and resulting in harmonic generation at odd multiples of the THz driving field frequency[23,24,27].

In the THz region, previous work on graphene relying on comparably narrowband accelerator-based super-radiant THz sources reported a strong nonlinear response ($\chi^{(3)} \sim 10^{-9}\,m^2/V^2$), resulting in an efficient THG conversion efficiency of 0.1%[24]. Remarkably, this nonlinear response in graphene is achievable at moderate THz pump field strengths ranging between 10 to 90 kV/cm, at room temperature, and under ambient conditions. To enhance nonlinear effects in graphene-based samples in the THz region, several approaches have been used. For example, previous work has shown that an optimization of the carrier density in graphene can enhance the power conversion efficiency of the THz THG[28]. Metasurfaces can also be used to locally enhance an incident pump field to enable stronger HHG in a graphene sheet, reaching up to a 1% field conversion efficiency at an incident field strengths <30 kV/cm[29]. While these approaches are efficient in boosting nonlinear effects, they have certain limitations. Notably, they have been demonstrated independently in the context of a single graphene layer. A multiple-layer graphene device could offer longer interaction lengths to improve frequency conversion efficiency. However, it remains unclear how such a design could be combined with other techniques to enhance nonlinear effects. Moreover, most studies reported on THz HHG have relied on accelerator-based super-radiant sources, which provide narrow-bandwidth (20% of the central frequency, FWHM) multicycle THz pulses with peak field amplitudes reaching up to 85 kV/cm. Here, we access the regime of THz HHG using a table-top configuration generating a 32 kV/cm peak field, which consists of an ultrafast near-infrared source, a high-field THz setup, and a combination of THz spectral filters. Most importantly, we experimentally explore how to efficiently combine different strategies to enhance these nonlinear effects.

Here, we investigate the enhancement of third harmonic generation (THG) in chemical vapor deposition (CVD) graphene through three distinctive approaches. We first investigate the nonlinear response of stacked decoupled graphene sheets, ranging from 1 to 15 layers. Results show a correlation between the field strength of the generated third harmonic and the increasing number of graphene layers with a maximum nonlinear signal observed for 6 layers, partially due to a trade-off between enhanced interaction length and linear absorption. Then, we use an electrical gate to investigate the effect of doping concentration in a 1-, 2-, and 3-layer graphene stack. Finally, we look at the effect of a metallic patterned substrate to locally enhance the THz driving field. We compare three types of metasurfaces acting on the THz driving field as a bandpass filter, a bandstop filter, and a linear wire-grid polarizer (WGP). The two kinds of spectral filters provide larger field enhancements than any previously reported metasurface substrates up to now used in these THz HHG experiments. A simple model is proposed to estimate the THG enhancement factor based on the metasurface geometry. This study on a various set of graphene-based architectures provides privileged insight on the combination of distinct experimental strategies to increase frequency conversion processes in 2D materials.

Results

Stacked graphene layers

We explore THG in CVD graphene within the THz region using a table-top time-resolved THz setup generating single-cycle pulses from a nonlinear lithium niobate crystal[30] with a peak field of 360 kV/cm (see Methods). Multilayered graphene samples are fabricated on a THz transparent Zeonor substrate by successively depositing single graphene layers onto each other with the wet-transfer method (see Methods) while a 60 nm-thick aluminum oxide (Al_2O_3) spacing layers, only located between graphene sheets, reduces interlayer interactions. The total sample thickness remains significantly sub-wavelength, eliminating the need to satisfy phase-matching conditions to achieve coherent nonlinear effects.

The experimental configuration is shown schematically in Fig. 1. Sensitive detection of the THG signal requires the use of a lowpass filter (LPF), reducing the spectral width of the pump pulse and eliminating any residual pump at the third harmonic frequency. After the generation of the THG inside the graphene-based sample, a highpass filter (HPF) is used to limit the incident pump reaching the detection scheme. Although the HPF used in our experiment does not completely eliminate the pump, it still reduces the pump-induced noise at the third harmonic frequency to a value close to the noise floor. This technique relying on a HPF significantly increases the sensitivity of time-resolved detection to monitor the creation of new spectral components[24,29]. The general design of these filters are described in previous work[31] and their spectral transmission properties are shown in Section 2 of the Supplementary Information. In brief, the LPF transmits multicycle THz pump pulse centered at the frequency, $\omega = 0.8$ THz, and strongly attenuates (~50 dB) spectral components beyond 1.5 THz. The HPF attenuates the pump pulse by >30 dB while transmitting the third harmonic at 3ω.

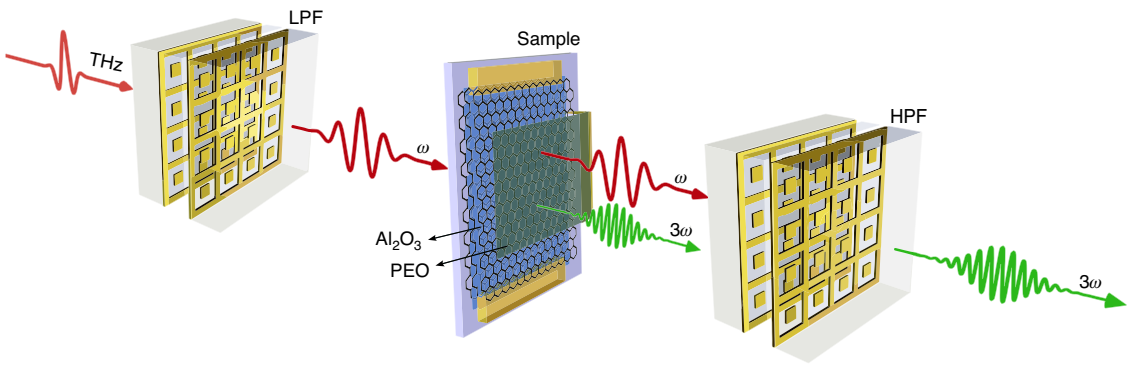

Fig. 1 Schematic of the experimental configuration at the sample position to generate and detect THz third harmonic generation. A LPF transmits a multicycle fundamental pulse at ω, which produces a signal at 3ω after nonlinear interactions in a graphene-based sample. The LPF and HPF consist of a superposition of four metasurfaces, but two only are schematically shown here for clarity. The graphene sheet is attached to electrodes (top and bottom), functioning as source and drain terminals for electrical characterization. Gating is facilitated by a polymer electrolyte [$LiClO_4$-Polyethylene oxide (PEO)] layer deposited on top of the graphene sample

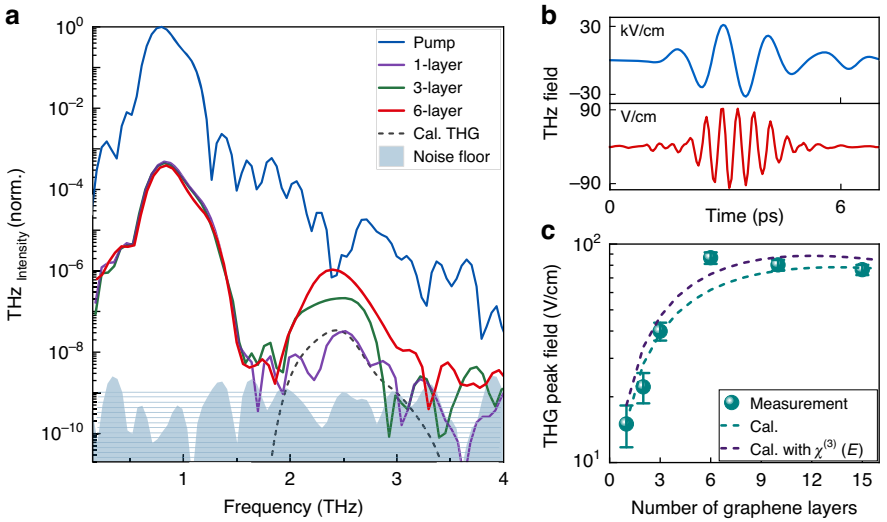

Fig. 2 Measured THG in stacked graphene layers. a The blue line represents the spectrum of normalized THz pump intensity transmitted through a LPF. A HPF is used to collect the other measurements. THG signature is observed around 2.4 THz for stacked graphene layers: 1-, 3-, and 6-layers. The grey shaded area shows the noise floor. The dashed black line is a calculation of the THG spectrum produced by a single-layer graphene also accounting for the experimental detection efficiency. **b** Time-domain THz transient of the pump pulse (blue line) and third harmonic pulse (red line) collected with 6-layer graphene. The y-axis units for the fundamental pulse are kV/cm and they are V/cm for the third harmonic, **c** THG peak field measured in samples with different numbers of graphene layers (green circles) compared with calculations (dashed lines). The error bars correspond to the standard deviation calculated from five measurements on different spots

We investigate six nonlinear samples consisting of stacked graphene sheets, from 1 to 15 layers, allowing us to vary the nonlinear interaction length. Figure 2a shows the spectrum of the THz pulse (blue line) transmitted through the LPF and used as the pump at the fundamental frequency ω. This graph only contains spectral measurements collected with the 1-, 3-, and 6-layer graphene samples (purple, green and red lines, respectively) for enhanced clarity of the display. A distinct THG spectral peak at $3\omega = 2.4$ THz can be observed with an intensity increasing roughly quadratically with the number of graphene layers (see Sections 1 and 3 in the Supplementary Information). The HPF, which role is to decrease the residual pump, allows the noise level at frequencies beyond 1.5 THz to settle close to the noise floor (grey shaded area), enabling sensitive monitoring of the nonlinear effects. Figure 2b shows the time-resolved multicycle pump pulse (blue line) with a peak amplitude of 32 kV/cm. This signal is compared to the THG waveform (red line) generated by a 6-layer graphene sample. The

time-resolved pump pulse is measured directly by electro-optic sampling in the experiment. The third harmonic waveform, weak in amplitude in comparison to the residual pump, is extracted by numerically applying a spectral bandpass filter around 2.4 THz and then using the inverse Fourier transform. Figure 2c shows the third harmonic peak amplitude obtained with all the samples investigated in this experiment. The largest nonlinear signal is obtained with the stack of 6 layers. This sample yields a THG peak amplitude that is a factor of 5.8 (or 33 in peak intensity) larger than the one obtained with the single graphene sheet. We do not observe further increase of the THG peak amplitude using a stack of 10 or 15 layers due to linear losses experienced by the pump and the third harmonic signal. To monitor the level of inhomogeneity on each graphene-stack samples, data is collected on 5 different spatial spots separated by 700 μm. We find standard variations of the THG signal of 22% for the single graphene layer (error bars in Fig. 2c). Spatial fluctuations in nonlinear properties can be attributed to an inhomogeneous distribution of impurities, such as PMMA residues, and uneven sample growth quality leading to changes in the doping level and electronic transport properties[32]. Much smaller fluctuations of ~6% are measured with the 10- and 15-layer samples due to a smoothing effect of the spatial inhomogeneities across the different graphene layers. The displayed amplitudes in Fig. 2b, c correspond to the THG field after the graphene sample as we multiply the measured amplitude by 1.9 to account for the total experimental losses at 2.4 THz. Three effects leading to this signal attenuation are considered: (i) a 25% (factor of 1.33) decrease of the THG signal is due to the gating pulse duration (108 fs FWHM), which reduces the detection sensitivity towards higher THz frequencies[33]; (ii) a 11% (factor of 1.12) lower detection efficiency at 2.4 THz is due to phase matching conditions in the THz detection crystal (see Section 4 in the Supplementary Information); (iii) a 21% (factor of 1.27) is lost because of the transmission properties of the HPF (see Section 2 in the Supplementary Information). Taking these factors into account, we found a peak field conversion efficiency of ~0.2% in 6-layer graphene. When considering the spectrally integrated third harmonic amplitude within the 1/e peak linewidth, the conversion efficiency reaches 0.24%. This value is twice the maximum efficiency previously reported for a single-layer graphene[24], which was obtained with an accelerator-based super-radiant source producing longer multicycle pulses at a lower fundamental frequency of 0.3 THz. Note that a driving THz field with a larger number of cycles would likely lead to larger optical nonlinearities induced by deposited heat[28]. Additionally, a lower driving frequency is expected to produce a stronger nonlinear THz conduction in graphene[23,26].

We perform theoretical calculations of the THG spectrum and peak amplitude based on the nonlinear wave equations[8] using the experimentally measured pump spectrum and peak driving field. Figure 2a shows the calculated spectrum generated within a single graphene sheet (black dashed line) using a nonlinear coefficient $\chi^{(3)} = 2.4 \times 10^{-10}$ m^2/V^2, which is obtained by fitting the THG peak value. To allow direct comparison between this calculation and raw experimental spectral curves in Fig. 2a, we divide the theoretical result by 3.6 (square of the factor 1.9 described above for the field amplitude) to account for experimental losses. The third-order nonlinear coefficient used in this calculation is 20% lower than the one reported in previous work ($\chi^{(3)} = 3 \times 10^{-10}$ m^2/V^2 at 32 kV/cm) in a similar experiment[29]. This can be in part attributed to the duration of our THz driving field, which is shorter than the one used in most previous work on THz HHG. Since the nonlinear response is expected to originate from a ~1 ps energy relaxation time[23], a longer-lasting multicycle driving signal may result in slightly larger nonlinearities[28]. In Fig. 2c, nonlinear calculations using the parameters found for a single-sheet graphene are performed for multilayered graphene samples from which we can extract the THG peak amplitude (see Section 3 in the Supplementary Information). We consider a 4% amplitude loss (8% power loss) for both the THz pump and third harmonic as they pass each graphene layer (see Section 1 in the Supplementary Information). This loss in the THz region is consistent with values reported by previous work[26,32,34]. Furthermore, we also perform the same calculation with a third-order nonlinear coefficient that is a function of the field strength according to previous experimental observation in graphene[29] (see Section 1 in the Supplementary Information). We find an overall agreement between the model and experimental results, and no major differences when field-dependent nonlinearities of graphene are introduced in the model. The main discrepancies between the experiment and calculations, which arise when the number of layers exceeds 3, can be in part attributed to variations of the nonlinear and electrical transport properties across different graphene sheets, as previously observed in other experiments involving graphene[35]. Our calculations indicate that the maximum THG signal is expected for a 9-layer device, which is 14% larger than the signal calculated for a 6-layer device. As a result, the higher nonlinear conversion efficiency experimentally observed with a 6-layer graphene sample can be attributed to sheet-to-sheet fluctuations of the nonlinear properties of graphene.

Electrical gating tunability of stacked graphene

Graphene's electronic THz nonlinearity has been attributed to the interaction of the THz field with free carriers and the subsequent interplay among electronic,

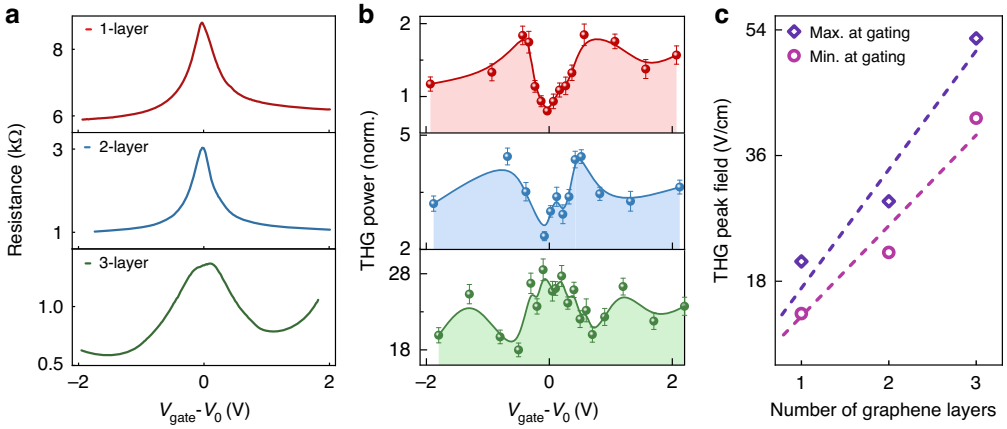

Fig. 3 Electrical tunability of terahertz nonlinearity in gated multilayer graphene sheets. a Experimentally measured sheet resistance and **b** extracted THG power for 1-layer (red), 2-layer (blue), and 3-layer (green) graphene sheets as we vary the gate voltage (V_{gate}). V_0 represents the applied voltage necessary to reach the maximum resistance of graphene, corresponding to the lowest carrier density. The circles represent experimental data points with error bars representing the standard deviation of the measurements, and the lines depict a b-spline interpolation used as a guide to the eye. **c** Maximum and minimum THG peak field amplitudes measured on all gated multilayered samples while varying the gate voltage. The dashed line shows a linear fit

phononic, and thermodynamic processes[6,23,36]. Therefore, a variation of the nonlinear response can be induced by an electrical gate changing the carrier density[28]. We use 1-, 2-, and 3-layer graphene samples electrically connected to a gate to simultaneously study the effect of carrier density and a multilayered design on nonlinear effects. The density is controlled using a polymer electrolyte ($LiClO_4$-Polyethylene oxide (PEO)) gate[37,38] connected to each graphene layer of the stack (see Methods). The electrical resistance of the samples is monitored by measuring the source-drain current as a function of the gate voltage. From these measurements, one can define the voltage offset V_0 required to reach the minimum free carrier density, also referred to as the charge neutrality point. As shown in Fig. 3a, the total resistance decreases as we increase the number of layers because they are connected in parallel (see Fig. S5 of the Supplementary Information). By scanning the gate voltage V_{gate}, we obtain a standard resistance response with a peak corresponding to the minimum doping concentration while the n- and p-doped region correspond to the negative and positive region of V_{gate}-V_0, respectively. We vary the gate voltage and monitor the THG power calculated by integrating the spectrum centered at 2.4 THz over the $1/e^2$ bandwidth. Figure 3b shows experimental measured THG power (circles) as a function of V_{gate}-V_0 where error bars represent the standard deviation of the measurements. With a single graphene layer, we find a minimum THG power at the charge neutrality point because less carriers are contributing to the material nonlinearities[28]. We find two maxima symmetrically on each side of this point, at $|V_{gate}\text{-}V_0| = 0.7$ V. The ratio between the two extreme values is $\varepsilon_{1G} = 2.3$, which confirms that controlling the carrier density is essential for optimizing the THG efficiency. As we further increase both the n- and p-doping concentration, the nonlinear signal decreases by about 50%. This behavior agrees with previous reports on the emergence of a metallic phase at high doping concentration gradually reducing the material's thermodynamic nonlinearity[28].

Interestingly, the dependence of the THG power as a function of the gate voltage is different when we add more graphene layers. In the case of a 2-layer graphene sample, the dependence on V_{gate} closely resembles the one observed with a single layer. However, we find $\varepsilon_{2G} = 1.9$, which is lower than the same ratio measured with a single layer ε_{1G}. For 3 layers, the signal as a function of V_{gate} is more erratic, with a peak, instead of a dip, around V_{gate}-$V_0 = 0$, and what appears to be random oscillations as a function of V_{gate}. Nonetheless, we measure $\varepsilon_{3G} = 1.6$, indicating the significant effect the gate still has on the carrier density to enhance the sample's nonlinear effects. The lower values of ε as the number of graphene layer is increased can be attributed to a different intrinsic doping concentrations across the layers, resulting in different values for V_0[35]. As a result, it is unlikely that the neutrality point of multiple superimposed graphene layers can be reached simultaneously with a single gate. Also, because of the device geometry, the change in carrier density may be different across the layers because of a screening effect, potentially causing larger variations inside the layers closer to the gate on top. Therefore, a multilayered architecture able to independently control carrier density in each graphene sheets would be optimal to reach

maximum nonlinear effects. In this experiment, the 3-layer sample displays the highest nonlinear conversion efficiency due to its longer interaction length even though gate-induced enhancement of nonlinear effects is slightly lower as discussed above. Figure 3c shows the minimum and maximum THG power obtained while changing V_{gate} with the 1-, 2-, and 3-layer gated graphene samples. These two sets of data when expressed in their corresponding peak field values follow a linear dependence (dashed lines) with the number of layers. The significant separation between these lines attest to the importance in controlling graphene's carrier density to optimize nonlinear effects.

Metamaterial-graphene architectures

In a third series of experiments, we explore the effect of metasurfaces on THG in an architecture combining multilayer graphene and an electrical gate. Three different designs of metasurfaces are considered based on their distinctive spectral transmission properties at the THz pump frequency. Figure 4a shows a schematic of these samples. They consist of a cross-slot bandpass filter (BPF), a cross-shaped bandstop filter (BSF), and a wire-grid polarizer (WGP). Two superimposed graphene sheets acting as the nonlinear medium are transferred on each metasurface. A transparent polymer electrolyte gate deposited on top of the structure is used to vary the carrier density (see Section 5 of the Supplementary Information). Figure 4c shows the measured THz transmission spectrum of each device with the fundamental resonance of the BPF and BSF centered at the THz pump frequency of 0.8 THz. We use FDTD simulations (Lumerical) to visualize the electric field distribution within a metasurface's unit cell at the height corresponding to the 2-layer graphene sample (Fig. 4b). We observe a significant enhancement of the incident THz field in the gap between metallic elements, locally reaching more than an order of magnitude. Since the third harmonic field amplitude $E_{3\omega}$ has a cubic dependence on the driving field E_{ω}, this effect directly leads to a more efficient THG. Figure 4d shows the measured third harmonic power normalized to the value obtained with the bare 2-layer graphene. We distinguish measurements collected when no gate voltage is applied ($V_{gate} = 0$) (yellow columns) and when V_{gate} is optimized to reach the maximum THG power (blue columns). The BSF-graphene architecture leads to the largest THG power. We measure an enhancement factor of 2.5 when the sample is non-gated and a factor of 3 when V_{gate} is optimized to the maximum THG power. The WGP-graphene architecture increases the THG power by a factor of 2 for non-gated approach, similar to the results presented in previous work for a similar device at the same peak field[29]. The use of BPF slightly reduces THG if the sample is not gated. Although this structure locally displays a high field enhancement, this feature is partially counteracted by a large fraction of the sample covered by the metallic structure, and therefore not contributing to nonlinear effects. For both BPF and WGO, the effect of gating can increase the THG signal by 20% and 75%, respectively.

To theoretically estimate the impact of the metasurface substrate on the nonlinear conversion efficiency, we use numerical simulations to calculate the field distribution and we then integrate E_{ω}^3 within a metasurface's unit cell (uc). This value is compared to a reference obtained without the metasurface. In our calculations, we incorporated the induced field dependence of the third-order nonlinear coefficient, $\chi^{(3)}(E_{\omega})$, using a rational fitted model derived from previously work[29] (see Section 1 in the Supplementary Information for simulation details and fitting model). The ratio $\gamma = \oint_{uc}\chi^{(3)}E_{\omega,MS}^3 da / \oint_{uc}\chi^{(3)}E_{\omega,0}^3 da$ indicates the THG enhancement factor induced by the metasurfaces. In Fig. 4d, we compare γ (magenta columns) to the corresponding experimental results. We find a good agreement between the calculated and measured THG power. The slight discrepancies may arise from variations in the enhancement of plasmonic structures between simulations and fabricated samples, particularly at the sharp edges. Additionally, minor shifts in resonance may occur due to deviations in dimensions during the fabrication process.

Numerical simulations reveal that the field amplitude at the driving frequency remains nearly constant along the direction normal to the substrate. Within a 2 μm distance, the amplitude variation remains below 5%. This ensures that similar metasurface-induced enhancement factors of the THG signal will be observed regardless of the number of decoupled graphene layers in the sample. This remains true for thick samples since, after 15 graphene layers, additional layers contribute less to the THG signal due to the absorption of the driving field. Therefore, considering a sample with 6 to 9 decoupled graphene sheets, electrically connected to allow independent control of carrier concentration in each layer, and deposited on a BSF metasurface substrate, we can envision a total THG enhancement factor exceeding 100.

Discussion

Figure 5 summarizes the measured and calculated THG in single and multilayer graphene samples as a function of the incident THz pump peak field. Using a single graphene sheet (purple circles) and a 6-layer graphene (red circles) device, we monitor the THG at several driving fields while moving the position of the sample at the THz focus along the driving beam propagation axis. Using the model described in Section 1 of the Supplementary Information, we also calculate the corresponding THG field (dashed lines). We compare our findings with those reported by Deinert et al.[29] on THz THG in a single graphene sheet (open circles), which is consistent with our results. When graphene is deposited on a grating

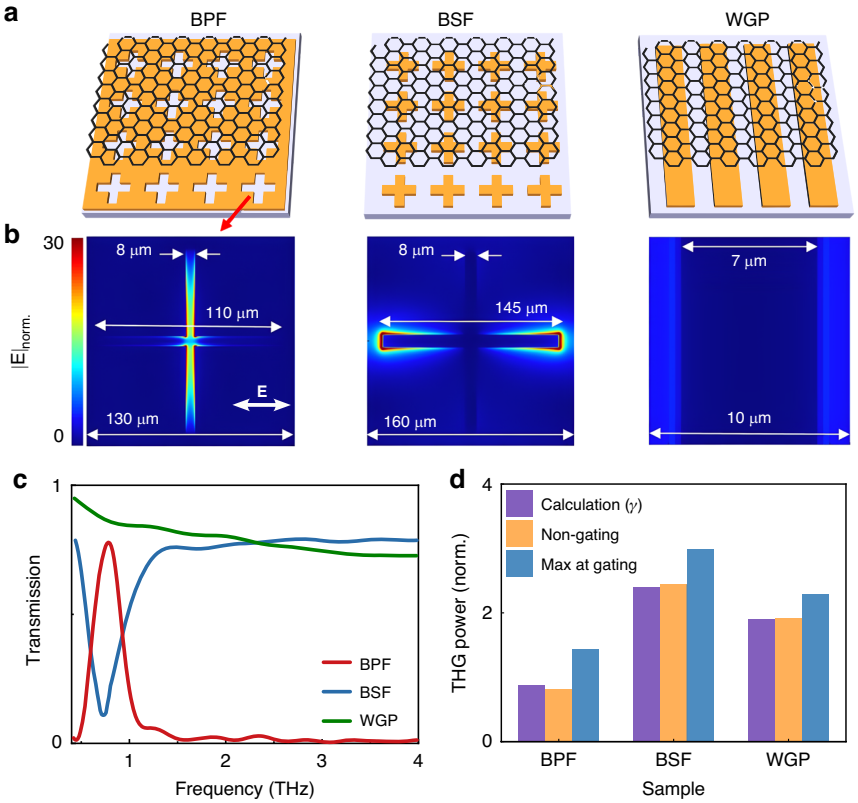

Fig. 4 Metamaterial-graphene-based architectures. a Schematic of a cross-slot bandpass filter (BPF), cross-shaped bandstop filter (BSF), and a wire-grid polarizer (WGP) with multilayer graphene deposited on their top surface. **b** FDTD simulated electric field distribution inside graphene for the three architectures. Metallic elements are shown in dark blue. **c** Measured THz power transmission of the metamaterial structures displaying fundamental resonances around 0.8 THz for the BPF and BSF. **d** Metasurface-induced enhancement of the THG signal. We show numerical calculations γ compared to experimental THG power normalized to the value obtained with a bare 2-layer graphene. We distinguish measurements collected when no gate voltage is applied ($V_{gate} = 0$) and when V_{gate} is optimized to obtain a maximum THG

metasurface (MS) structure (open squares), similar to a wire-grid polarizer (WGP) design, Deinert et al. observe a ten-fold increase in THG amplitude. Using a similar device architecture, we observe a THG signal (orange squares) that is not as high, which might be due to sample-to-sample fluctuations in electric transport properties in graphene. Similar THG field amplitudes can nonetheless be reached using a 6-layer graphene sample (red circles) or by depositing a three-layer graphene sample on a WGP (orange diamonds). Note that saturation effects in graphene at high fields limit the maximum THG signal when the THz driving field exceeds 20 kV/cm. A multilayer sample can be used to achieve a large THG signal without relying on local field enhancement, which mitigates these saturation effects. Furthermore, in such a multilayer design, each graphene layer partially absorbs the driving field, which also contributes in reducing saturation effects. As a result, a design relying on multiple-layer graphene offers the best perspective for nonlinear frequency conversion at high driving fields, while a graphene mounted on a metasurface offers the largest enhancement factor at low driving fields, away from the saturation regime. Interestingly, calculations show that a bandstop or bandpass metasurface substrate can lead to an enhancement of the THG amplitude generated in graphene by more than two orders of magnitude at a weak incident field <1 kV/cm (see Section 6 of the Supplementary Information).

We investigate third harmonic generation (THG) in graphene in the THz range while relying on three types of device architectures to make this nonlinear process more efficient. We experimentally investigate nonlinear samples with (i) a different number of graphene layers to increase the nonlinear interaction length, (ii) an electrical bias with a gate voltage to optimize the carrier density, and (iii) metallic metasurface substrates to locally enhance the pump field. Especially, we explore the potential to combine these techniques together within one structure. The largest improvement of the THG signal is observed by increasing the number of graphene layers. In particular, the most efficient THG is measured with a 6-layered graphene sample, representing a trade-off between the nonlinear

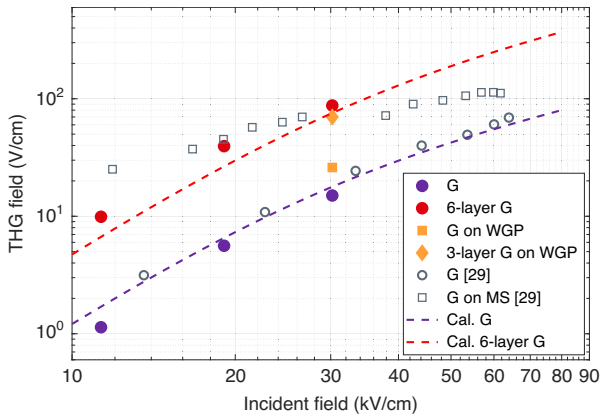

Fig. 5 Efficiency of THG strength in graphene over incident driving peak-field. Solid circles indicate the measured THG for 1-layer and 6-layer graphene. Orange squares and diamonds represent the THG enhancement for 1-layer and 3-layer graphene on a wire-grid polarizer (WGP) metamaterial. The gray circles and squares correspond to the THG measurements for 1-layer graphene on grating metasurface (MS) structures, as reported by Deinert et al.[29]. Dashed lines depict the THG considering the field-dependent third-order nonlinear coefficient ($\chi^{(3)}(E)$) for 1-layer and 6-layer graphene samples

interaction length and linear absorption, which leads to a third harmonic power 33 times higher than obtained with a single graphene layer. We then use a simple configuration allowing a transparent electrical gate to tune nonlinear properties of graphene-based samples. In a gated single graphene layer, THG can increase by a factor of 2.3. Although this factor is lower when the sample contains multiple graphene layers, the gating voltage always leads to a significant increase of the THG signal, larger than 60% in our experiment. Plus, a design allowing independent tuning of the free carrier concentration in each layers could be used to ensure a two-fold THG enhancement in multilayered designs. In a third series of experiments, different types of metasurfaces are used as substrate to explore the effect of local field enhancement on THG in graphene. Interestingly, the most efficient design is a bandstop filter (BSF) at the fundamental frequency, featuring a 3-fold increase in THG power. We propose a model based on numerical calculations to estimate the nonlinear signal enhancement induced by a metasurface, which provides good agreement with experimental results. More importantly, our work demonstrates the possibility to combine these strategies to potentially enhance THG by more than two orders of magnitude. The sample architectures can also apply to other types of 2D nonlinear materials, such as transition-metal dichalcogenides[39], and they can be combined with other techniques to enhance nonlinear effects, such as the use of topological insulating substrates[14,40]. Multilayered samples, potentially combining different materials, may also be an interesting route leading to enhanced THG, especially at high fluences. Additionally, given that the efficiency of THz generation and detection in table-top systems can still be improved, there remains many nonlinear phenomena leading to THz frequency conversion that are yet to be explored in greater detail. Altogether, such advancements are essential to enable efficient chip-integrated nonlinear THz signal converters that will be used in future communication technologies.

Materials and methods

Sample preparation

We use commercial monolayer CVD-grown graphene on copper foil, coated with a poly(methyl methacrylate) (PMMA) layer, obtained from Graphenea. Graphene layers of 1 cm × 1 cm dimensions are wet-transferred onto a 188 μm thick Zeonor substrate[32] (a cyclo-olefin copolymer transparent to THz radiation with a refractive index of n ~ 1.53 at 1 THz). This is followed by the deposition of a 60 nm-thick Al_2O_3 layer using an electron-beam evaporator (NexdepSeries, Angstrom). To form multilayer graphene samples, additional graphene layers and alternating Al_2O_3 layers are stacked on the same substrate.

The gating voltage is applied with a 5 nm Ti/20 nm Pd/150 nm Au electrodes deposited on the sides of the graphene layers using a single evaporation system and a shadow mask placed atop the graphene surface. The source and drain contacts make direct contact with the graphene layer, while the gating contacts has no direct contact. A spray-coating technique is employed to apply a 400 nm-thick transparent polymer electrolyte onto the graphene layers. The electrolyte is made of Polyethylene oxide (PEO) and $LiClO_4$ in an 8:1 weight ratio, which is dissolved in a methanol solution. Subsequently, the sample is affixed onto a custom-printed circuit board (PCB) with a central hole to perform optical transmission measurements. The electrical measurements are performed at constant voltage while monitoring the current with Keithley source meters (models 2400).

The metasurfaces are fabricated on a 188 μm thick Zeonor substrate using a conventional positive photolithography process. Aluminum is deposited onto the patterned substrate using a sputtering technique, followed by a lift-off process to achieve 200 nm-thick metallic arrays. Subsequently, a 60 nm-thick Al_2O_3 layer was deposited on the metasurfaces using an electron-beam evaporator, after which graphene sheets were wet-transferred onto them.

Experiment

In our experimental setup, high-field (360 kV/cm) single-cycle THz pulses are generated using the tilted pulse front technique in a $LiNbO_3$ crystal. These pulses originated from an amplified 10 kHz Yb-laser system with the following parameters: central wavelength of 1030 nm, a pulse width of 170 fs, and a pulse energy of 1 mJ. Detection involved electro-

optical sampling method by utilizing pulses from an optical parametric amplifier (OPA) at 960 nm wavelength, with a pulse duration of 108 fs (FWHM), and employing a 1 mm-thick GaP nonlinear detection crystal. The gating pulses at 960 nm satisfy phase matching condition in GaP to achieve high detection sensitivity at the third harmonic frequencies at 2.4 THz. All experiments are conducted at room temperature inside a dry-air purged enclosure.

Simulations

Numerical simulations are performed with a 3D finite-difference time-domain (FDTD) solver (Lumerical Inc.) to design the plasmonic metasurface resonators with fundamental resonances around 0.8 THz and explore the electric field distribution of the THz pump pulse on the structures. We utilize periodic boundary conditions along the in-plane axis. Additionally, a perfectly matched layer (PML) is applied in the direction of optical propagation to absorb all incident fields, effectively preventing any reflections at that interface. For the simulation of electric field spatial distributions, we employed a minimum override mesh size of 50 nm along the surface of the structures and 4 nm along the THz propagation direction.

Acknowledgements
We acknowledge funding from the Natural Sciences and Engineering Research Council of Canada (NSERC) Discovery funding program (RGPIN-2023-05365) and the University of Bayreuth Centre of International Excellence "Alexander von Humboldt". G.H. acknowledges funding by the Deutsche Forschungsgemeinschaft (DFG, German Research Foundation), via project 492723217. A. Maleki, G. Herink and J.-M. Ménard acknowledge financial support from the Mitacs Globalink Research Award. We thank B. Sullivan, A. Jaber, S. Ntais and S. Biberger for insightful discussions and technical support.

Author details
[1]Department of Physics, University of Ottawa, Ottawa, ON K1N 6N5, Canada. [2]Experimental Physics VIII – Ultrafast Dynamics, University of Bayreuth, Bayreuth 95447, Germany. [3]Iridian Spectral Technologies Ltd, Ottawa, ON K1G 6R8, Canada. [4]School of Electrical Engineering and Computer Science, University of Ottawa, Ottawa, ON K1N 6N5, Canada. [5]Institute of Optics and Department of Physics and Astronomy, University of Rochester, Rochester, NY 14627, USA

Author contributions
A.M., M.B.H., G.H., and J.-M.M. conceptualized the idea and designed the experiment. A.M. completed the FDTD simulations for the metasurfaces and Y.X. fabricated the metasurfaces. A.M. engineered the gated and non-gated multilayer graphene samples, and spectral filters. A.M. and M.B.H. carried out the measurements. A.M. and J.-M.M., analyzed the experimental results. R.W.B., G.H., and J.-M.M. supervised this work.

Data availability
The experimental data that support the findings of this work is available upon reasonable request from the corresponding authors.

Conflict of interest
The authors declare no competing interests.

Supplementary information The online version contains supplementary material available at https://doi.org/10.1038/s41377-024-01657-1.

Received: 20 May 2024 Revised: 23 September 2024 Accepted: 29 September 2024
Published online: 09 January 2025

References

1. Pizzuto, A., Ma, P. C. & Mittleman, D. M. Near-field terahertz nonlinear optics with blue light. *Light Sci. Appl.* **12**, 96 (2023).
2. Chai, X. et al. Subcycle terahertz nonlinear optics. *Phys. Rev. Lett.* **121**, 143901 (2018).
3. Heindl, M. B. et al. Ultrafast imaging of terahertz electric waveforms using quantum dots. *Light Sci. Appl.* **11**, 5 (2022).
4. Nicoletti, D. & Cavalleri, A. Nonlinear light–matter interaction at terahertz frequencies. *Adv. Opt. Photonics* **8**, 401–464 (2016).
5. Koshihara, S. et al. Challenges for developing photo-induced phase transition (PIPT) systems: From classical (incoherent) to quantum (coherent) control of PIPT dynamics. *Phys. Rep.* **942**, 1–61 (2022).
6. Pogna, E. A. A. et al. Hot-carrier cooling in high-quality graphene is intrinsically limited by optical phonons. *ACS Nano* **15**, 11285–11295 (2021).
7. Ganichev, S. D. & Prettl, W. Terahertz nonlinear optics. in Intense Terahertz Excitation of Semiconductors (eds Ganichev, S. D. & Prettl, W.) (Oxford: Oxford University Press, 2005), 269–290, https://doi.org/10.1093/acprof:oso/9780198528302.003.0007.
8. Boyd, R. W. *Nonlinear Optics*. 4th edn. (London: Academic Press, 2020), https://doi.org/10.1016/C2015-0-05510-1.
9. Yang, X. et al. Lightwave-driven gapless superconductivity and forbidden quantum beats by terahertz symmetry breaking. *Nat. Photonics* **13**, 707–713 (2019).
10. Vaswani, C. et al. Terahertz second-harmonic generation from lightwave acceleration of symmetry-breaking nonlinear supercurrents. *Phys. Rev. Lett.* **124**, 207003 (2020).
11. Reinhoffer, C. et al. Strong terahertz third-harmonic generation by kinetic heavy quasiparticles in $CaRuO_3$. *Phys. Rev. Lett.* **132**, 196501 (2024).
12. Meng, F. Q. et al. Higher-harmonic generation in boron-doped silicon from band carriers and bound-dopant photoionization. *Phys. Rev. Res.* **5**, 043141 (2023).
13. Murakami, Y., Nagai, K. & Koga, A. Efficient control of high harmonic terahertz generation in carbon nanotubes using the Aharonov-Bohm effect. *Phys. Rev. B* **108**, L241202 (2023).
14. Tielrooij, K. J. et al. Milliwatt terahertz harmonic generation from topological insulator metamaterials. *Light Sci. Appl.* **11**, 315 (2022).
15. Giorgianni, F. et al. Strong nonlinear terahertz response induced by Dirac surface states in Bi_2Se_3 topological insulator. *Nat. Commun.* **7**, 11421 (2016).
16. Kovalev, S. et al. Terahertz signatures of ultrafast Dirac fermion relaxation at the surface of topological insulators. *npj Quantum Mater.* **6**, 84 (2021).
17. Kovalev, S. et al. Non-perturbative terahertz high-harmonic generation in the three-dimensional Dirac semimetal Cd_3As_2. *Nat. Commun.* **11**, 2451 (2020).
18. Zhou, R. et al. Engineering the harmonic generation in graphene. *Mater. Today Phys.* **23**, 100649 (2022).
19. Yoshikawa, N., Tamaya, T. & Tanaka, K. High-harmonic generation in graphene enhanced by elliptically polarized light excitation. *Science* **356**, 736–738 (2017).
20. Cha, S. et al. Gate-tunable quantum pathways of high harmonic generation in graphene. *Nat. Commun.* **13**, 6630 (2022).
21. Calafell, I. A. et al. High-harmonic generation enhancement with graphene heterostructures. *Adv. Opt. Mater.* **10**, 2200715 (2022).
22. Soavi, G. et al. Hot electrons modulation of third-harmonic generation in graphene. *ACS Photonics* **6**, 2841–2849 (2019).
23. Hafez, H. A. et al. Terahertz nonlinear optics of graphene: from saturable absorption to high-harmonics generation. *Adv. Opt. Mater.* **8**, 1900771 (2020).
24. Hafez, H. A. et al. Extremely efficient terahertz high-harmonic generation in graphene by hot Dirac fermions. *Nature* **561**, 507–511 (2018).
25. Di Gaspare, A. et al. Electrically tunable nonlinearity at 3.2 terahertz in single-layer graphene. *ACS Photonics* **10**, 3171–3180 (2023).
26. Mics, Z. et al. Thermodynamic picture of ultrafast charge transport in graphene. *Nat. Commun.* **6**, 7655 (2015).
27. Mao, W. W., Rubio, A. & Sato, S. A. Terahertz-induced high-order harmonic generation and nonlinear charge transport in graphene. *Phys. Rev. B* **106**, 024313 (2022).

28. Kovalev, S. et al. Electrical tunability of terahertz nonlinearity in graphene. *Sci. Adv.* **7**, eabf9809 (2021).
29. Deinert, J. C. et al. Grating-graphene metamaterial as a platform for terahertz nonlinear photonics. *ACS Nano* **15**, 1145–1154 (2021).
30. Hebling, J. et al. Velocity matching by pulse front tilting for large-area THz-pulse generation. *Opt. Express* **10**, 1161–1166 (2002).
31. Maleki, A. et al. Metamaterial-based octave-wide terahertz bandpass filters. *Photonics Res.* **11**, 526–532 (2023).
32. Scarfe, S. et al. Systematic THz study of the substrate effect in limiting the mobility of graphene. *Sci. Rep.* **11**, 8729 (2021).
33. Gallot, G. & Grischkowsky, D. Electro-optic detection of terahertz radiation. *J. Opt. Soc. Am. B* **16**, 1204–1212 (1999).
34. Hwang, H. Y. et al. Nonlinear THz conductivity dynamics in P-Type CVD-grown graphene. *J. Phys. Chem. B* **117**, 15819–15824 (2013).
35. Rautela, R. et al. Mechanistic insight into the limiting factors of graphene-based environmental sensors. *ACS Appl. Mater. Interfaces* **12**, 39764–39771 (2020).
36. Jensen, S. A. et al. Competing ultrafast energy relaxation pathways in photoexcited graphene. *Nano Lett.* **14**, 5839–5845 (2014).
37. Das, A. et al. Monitoring dopants by Raman scattering in an electrochemically top-gated graphene transistor. *Nat. Nanotechnol.* **3**, 210–215 (2008).
38. Li, H. M. et al. Electric double layer dynamics in poly(ethylene oxide) $LiClO_4$ on graphene transistors. *J. Phys. Chem. C.* **121**, 16996–17004 (2017).
39. Wen, X. L., Gong, Z. B. & Li, D. H. Nonlinear optics of two-dimensional transition metal dichalcogenides. *InfoMat* **1**, 317–337 (2019).
40. Shi, J. J. et al. Giant room-temperature nonlinearities in a monolayer Janus topological semiconductor. *Nat. Commun.* **14**, 4953 (2023).

Supplementary information for

Strategies to enhance THz harmonic generation combining multilayered, gated, and metamaterial-based architectures

Ali Maleki,[1] Moritz B. Heindl,[2] Yongbao Xin,[3] Robert W. Boyd,[1,4,5] Georg Herink,[2] Jean-Michel Ménard[1,4,*]

[1]*Department of Physics, University of Ottawa, Ottawa, ON K1N 6N5, Canada*
[2]*Experimental Physics VIII – Ultrafast Dynamics, University of Bayreuth, Bayreuth, 95447, Germany*
[3]*Iridian Spectral Technologies Ltd, Ottawa, ON K1G 6R8, Canada*
[4]*School of Electrical Engineering and Computer Science, University of Ottawa, Ottawa, ON K1N 6N5, Canada*
[5]*Institute of Optics and Department of Physics and Astronomy, University of Rochester, NY 14627, USA*

**Email: Jean-Michel Ménard (jean-michel.menard@uottawa.ca)*

Section S1: Calculations of the third harmonic generation (THG)

Fig. S1a depicts the schematic of a multilayer graphene nonlinear sample, illustrating the interaction of a pump pulse with graphene layers and resulting THG signals on each layer. The THG signals produce in each graphene sheets accumulate as the THG pulse propagates in the structure. In detail, the THz pump pulse (E_ω) first impinges on the Zeonor substrate, experiencing an 8% power transmission loss due to Fresnel reflections at the air-substrate interface. Then, successive third harmonic fields ($E_{3\omega}^i$) are produced by the THz driving field (E_ω^i) incident on each graphene layers, where i = 1, 2, 3, … refers to the position of the graphene sheet in the multiplayer stack. During the THz pulse propagation through a stack of graphene sheets, we consider that 4% of the pump pulse amplitude is absorbed in the first graphene layer. The remaining pump pulse then proceeds to interact with the second layer to generate a slightly weaker THG ($E_{3\omega}^2$) and where another 4% gets absorbed. This absorption and signal generation process continues for subsequent graphene layers. It is important to note that we also consider a 4% absorption of the third harmonic field amplitude as this component propagates through each graphene layer. Considering both the absorption of the pump pulse (α_ω) and third harmonic components ($\alpha_{3\omega}$), we establish a relationship for THG in n-layer graphene structures as follows:

$$E_{3\omega}^{Total} = \sum_{i=1}^{n} E_{3\omega}^{i} = \frac{3\omega d}{8cn_{3\omega}} \chi^{(3)} \sum_{i=1}^{n} [(1-\alpha_\omega)^{3(i-1)}(1-\alpha_{3\omega})^{n-i} E_{3\omega}^{1},$$

where c is the speed of light, d = 0.3 nm is the thickness of each graphene layer, $n_{3\omega}$ = 10 is the refractive index of the graphene layer, ω is the pump radial frequency, and $\chi^{(3)}$ is the third order susceptibility. For these calculations, we used the linear properties of graphene reported in previous work[1] and nonlinear coefficient of $\chi^3 = 2.4 \times 10^{-10}$ m^2 V^{-2} obtained from our THG data obtained with a single graphene layer.

Since the coefficient $\chi^{(3)}$ of graphene has been observed to be a function of the driving field amplitude, we extract this dependence from previously reported data[1] (circles in Fig. S1b). We calculate a fitting function: $\chi^{(3)} = \frac{7.2e^{-10}}{1+1e^{-9}E_\omega+12e^{-4}E_\omega{}^2}$ in m^2/V^2, where E_ω is the driving electrical

field amplitude in kV cm^{-1}. This model considers a maximum value for $\chi^{(3)}$ as suggested by the thermodynamic calculations of Ref. [1].

This expression for $\chi^{(3)}$ is not only used to estimate the THG in a multilayer graphene structure (purple line in Fig. 2c), but also determine the effect of an inhomogeneous field distribution induced by a metasurface substrate on the THG (purple column in Fig. 4d). We define the metasurface-induced enhancement factor as:

$$\gamma = \oint_{uc} \chi^{(3)} \left(E_{\omega,MS}\right)^3 \, da / \oint_{uc} \chi^{(3)} (E_\omega)^3 \, da,$$

which uses both the calculated electric field spatial distribution inside a graphene layer above the metasurface ($E_{\omega,MS}$), and a homogeneous field impinging on a graphene layer with no metasurface substrate (E_ω). The field modulation induced by the metasurface is simulated using a mesh size of 50 nm along the surface of the structure and 40 nm along the optical propagation direction. Decreasing the mesh size does not alter the results of the calculations. However, increasing the mesh size by a factor of 2 in the in-plane direction, to reach lower spatial resolution, decreases the calculated factor γ by about 5%.

Fig. S1c shows the transmission of the fundamental frequency through samples with different number of graphene layers, along with corresponding FDTD simulations of transmission, reflection, and absorption. We find a good agreement between the simulation and experimental results. The slight discrepancy can be attributed to intrinsic properties of each graphene layer, such as a varying doping level. A fit based on the Beer-Lambert equation reveals a 4% absorption of the THz field through each graphene layer. Reflection gradually increases for samples containing more than 6 layers of graphene, which is consistent with previous studies[2].

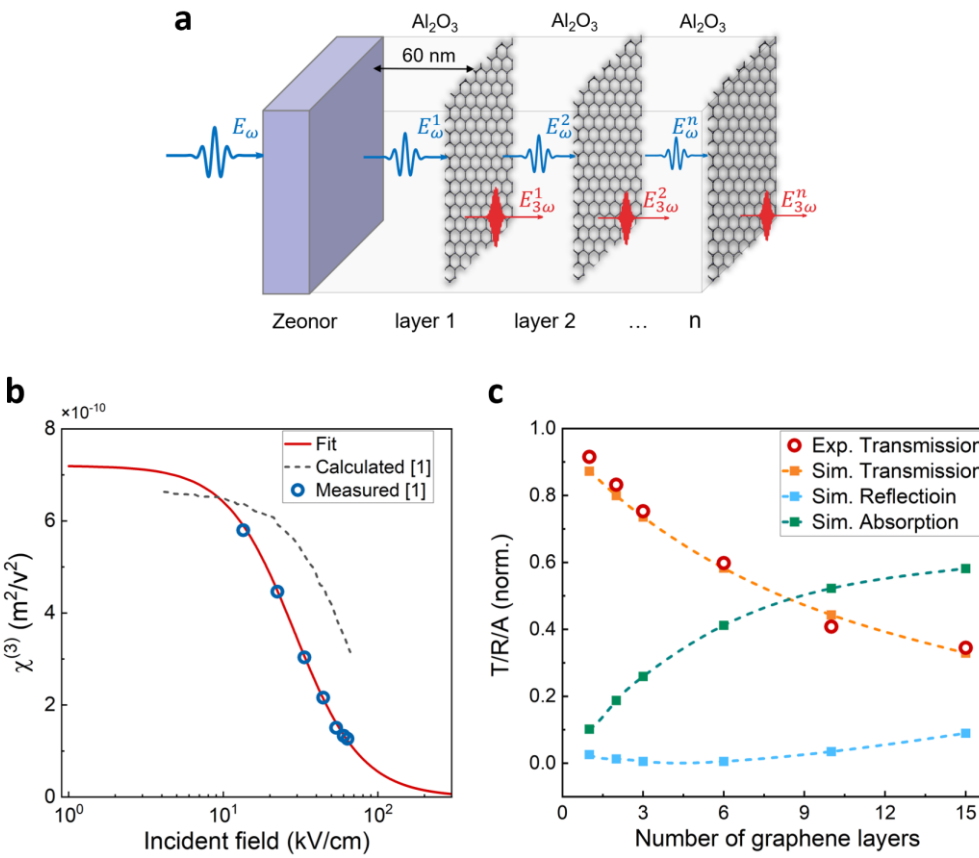

Fig. S1 a Schematic of the THz propagation in multilayer graphene sheets. THz pump pulses on each graphene layer are shown with blue pulses, and THG pulses are shown in red. The schematic of the nonlinear sample comprises a substrate (Zeonor in our experiment) and graphene layers (n-layer), that are separated by Al_2O_3. **b** Measured (circles) and calculated (dashed line) third order nonlinear coefficients ($\chi^{(3)}$) based on the thermodynamic model for a single layer graphene reproduced from J-C. Deinert et al.[1]. Solid line in red shows our fitting function. **c** Measured (red circles) transmission of the stacked graphene samples, obtained from the THz peak intensity at the fundamental frequency (0.8 THz). The solid points represent FDTD simulations of transmission, reflection, and absorption as a function of the number of graphene layers. The dashed lines indicate a spline interpolation to guide the eye.

Section S2: Lowpass filter (LPF) and highpass filter (HPF)

The schematic of the LPF and HPF structures and their corresponding intensity spectral transmission are shown in Fig. S2. The power transmission of the HPF filter is ~60% in the bandpass region, while it attenuates the pump pulse by more than 30 dB in the stopband region. Further improvements of these THz filters would help achieve a more sensitive THG detection.

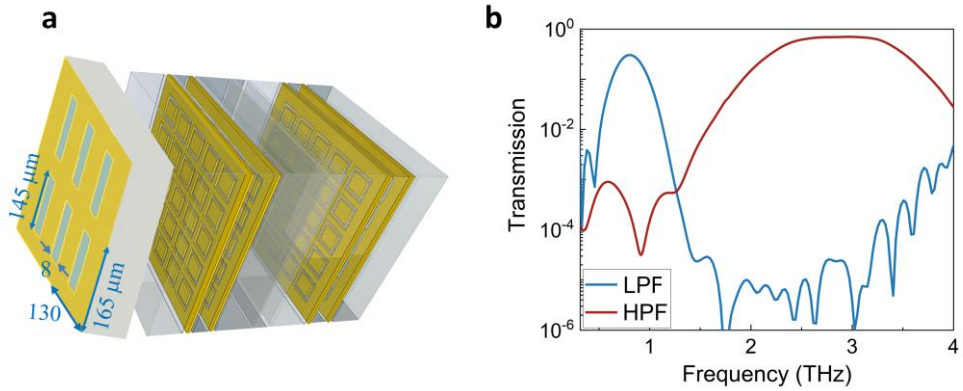

Fig. S2 a Schematic of the spectral filters. The highpass filter (HPF) is made of 4-layer square-slot plasmonic metasurfaces as described in our previous work[3]. During fabrication of the lowpass filter (LPF), we added a bar-slot bandpass filter on top of the 4-layer plasmonic structures to create a sharper bandpass around 0.8 THz and strongly attenuate any residual signal around 2.4 THz. **b** Intensity transmission of the LPF and HPF filters in the THz region.

Section S3: Power vs peak intensity of THG in stacked graphene layers

We calculated the spectral weight by integrating the THG signal in the spectral domain within the e^{-2} bandwidth as a function of the number of graphene layers. The THG peak intensity is obtained by squaring the results presented in Fig. 2c. Overall, the two parameters show the same behavior.

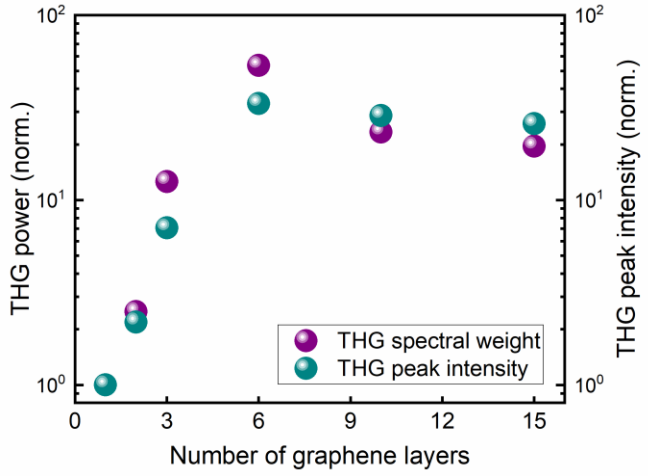

Fig. S3 Third harmonic generation (THG) signal as a function of the number of graphene layers calculated in the frequency domain by integrating the spectral weight to obtain the power (left axis), and in the time-domain by first calculating the field amplitude and then the corresponding peak intensity (right axis).

Section S4: Sensitivity of the GaP detection crystal

We use an electro-optical sampling method to monitor the THz spectrum. The gating pulse, produced by an optical parametric amplifier (OPA), is centered at 960 nm wavelength and has a pulse duration of 108 fs (FWHM) as shown in Fig. S4a. The autocorrelation is obtained by two-photon absorption in a Si photodiode. The deviation from the expected peak-to-background ratio of 8:1 is attributed to a small amount of three-photon-absorption. The wavelength is selected to optimize phase matching conditions at 2.4 THz in our THz detection crystal, which is a 1 mm-thick 110-oriented GaP crystal. The calculated detection efficiency at 2.4 THz is however still 11% lower than the detection efficiency at the pump pulse frequency of 0.8 THz. These calculations use the linear properties of GaP in the THz region[4] are shown in Fig. S4b. The factor of 11% is considered when we compare the field amplitude of the third harmonic and fundamental components.

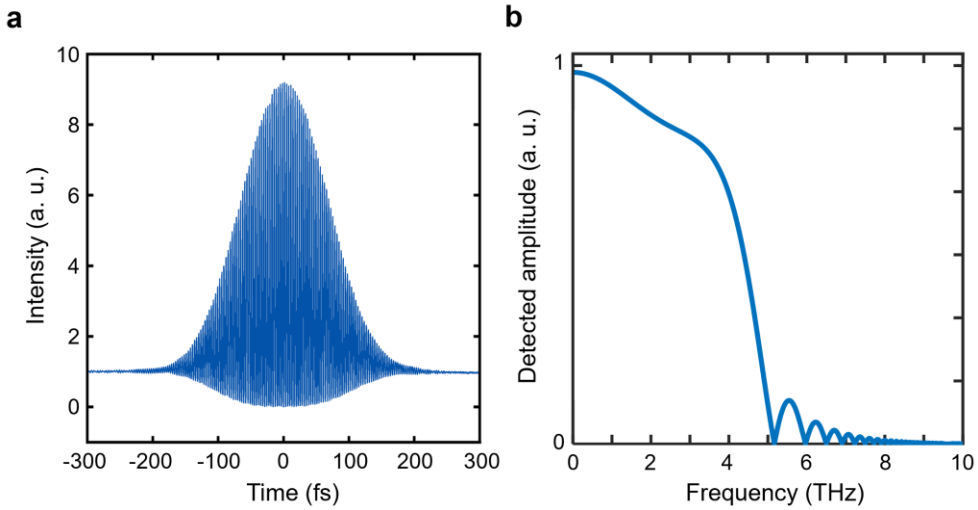

Fig. S4 a Measured interferometric autocorrelation of the gating pulse, representing intensity pulse duration of 108 fs at FWHM. **b** Simulated detection sensitivity of the GaP crystal at the gating 960 nm wavelength.

Section S5: Fabrication of multilayer graphene architectures

We use monolayer CVD graphene on copper foil coated with a poly(methyl methacrylate) (PMMA) layer, and wet transferred them on substrates. This is followed by the deposition of a 60 nm-thick Al_2O_3 layer in between graphene layers. The CVD graphene layer initially exhibited p-type doping, typically originating from chemical residues in the preparation process, wet-transferring processes, interactions with the substrate, and deposited polymer electrolyte[5]. In the next step, a pair of 5 nm Ti/20 nm Pd/150 nm Au electrodes were deposited on the sides of the graphene layers, serving as source and drain terminals for electrical characterization. The graphene sheets were connected in parallel on the sides of the metallic electrodes, as shown schematically in Fig. S5. For each graphene sample, we introduced a gate offset V_0 to effectively compensate for the intrinsically hole-doping effect and shift the Fermi energy towards a neutrally charged Dirac point. This V_0 voltage varied from sample to sample, typically ranging between 0.1 to 0.3 V.

We use the same fabrication process to transfer graphene sheets on plasmonic metasurfaces. 60 nm-thick Al_2O_3 layers serve as spacing between graphene layers and the plasmonic structures to avoid the possibility of any graphene-metal interactions. To apply electrical gating on the graphene-metasurface samples, we employ a spray-coating technique to deposit 400 nm-thick transparent polymer electrolyte (as described in Methods) onto the graphene layers. Finally, in the high-harmonic generation experiment, THz pump light illuminates the structure from the substrate side, initially reaching the plasmonic side, and then interacting with the graphene sheets to achieve THG.

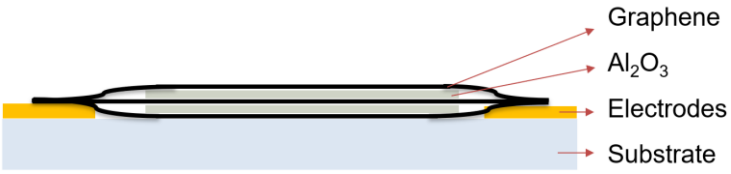

Fig. S5 Schematic of the side-view configuration depicting graphene layers electrically connected in parallel and all attached to metallic electrodes.

Section 6: Metamaterial-based field enhancement

We employ three distinct plasmonic geometries—BSF, BPF, and WGP structures—to locally enhance the THz driving field and improve the nonlinear THG efficiency. Using FDTD simulations, we calculated the electric field distribution within the metasurface unit cell (uc) at 0.8 THz and determined the field-induced THG enhancement ratio in graphene, defined as $\gamma = \oint_{uc} \chi^{(3)} E^3_{\omega,MS}\, da / \oint_{uc} \chi^{(3)} E^3_{\omega,0}\, da$ (see section Metamaterial-Graphene Architectures). This enhancement ratio for each structure is presented in Fig. S6 as a function of the incident field, demonstrating significant enhancement at lower driving fields but a saturation at higher fields to a value corresponding to the actual fraction of graphene not in direct contact with a metallic sub-structure of the metasurface. Due to the sharper geometries in the BPF and BSF structures, which are more effective at locally intensifying the field, this ratio can increase by up to two orders of magnitude at low incident THz driving field. However, saturation effects limit the THG field enhancement to a value below 5 at driving fields above 10 kV cm^{-1}.

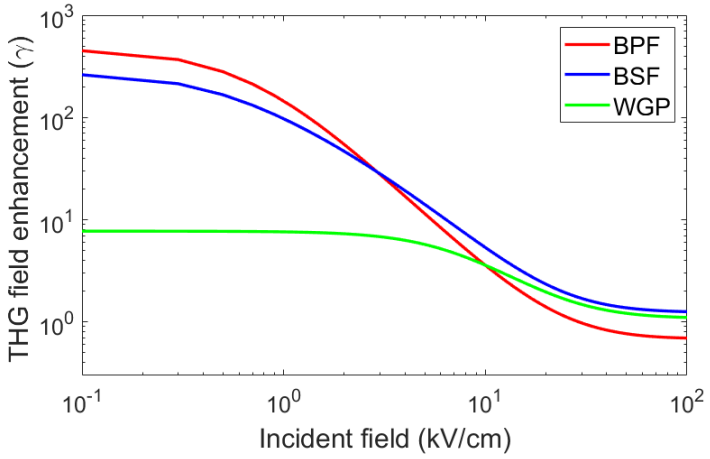

Fig. S6 Calculated THG field enhancement in graphene on different metamaterial structures: bandstop filter (BSF), bandpass filter (BPF), and wire-grid polarizer (WGP), as a function of the driving incident field.

References

1. Deinert, J. C. et al. Grating-graphene metamaterial as a platform for terahertz nonlinear photonics. *ACS Nano* **15**, 1145-1154 (2021).
2. Kim, S.-S., Kim, Y.-K., Park, I.-S. & Shin, S.-C. Optical properties of a thin-film stack illuminated by a focused field. *Journal of the Optical Society of America A* **17**, 1454-1460 (2000).
3. Maleki, A. et al. Metamaterial-based octave-wide terahertz bandpass filters. *Photonics Research* **11**, 526-532 (2023).
4. Gallot, G. & Grischkowsky, D. Electro-optic detection of terahertz radiation. *Journal of the Optical Society of America B* **16**, 1204-1212 (1999).
5. Ryu, S. *et al.* Atmospheric oxygen binding and hole doping in deformed graphene on a SiO2 substrate. *Nano Letters* **10**, 4944–4951 (2010).

Chapter 6

High-harmonic generation in graphene oxide and its reduced forms

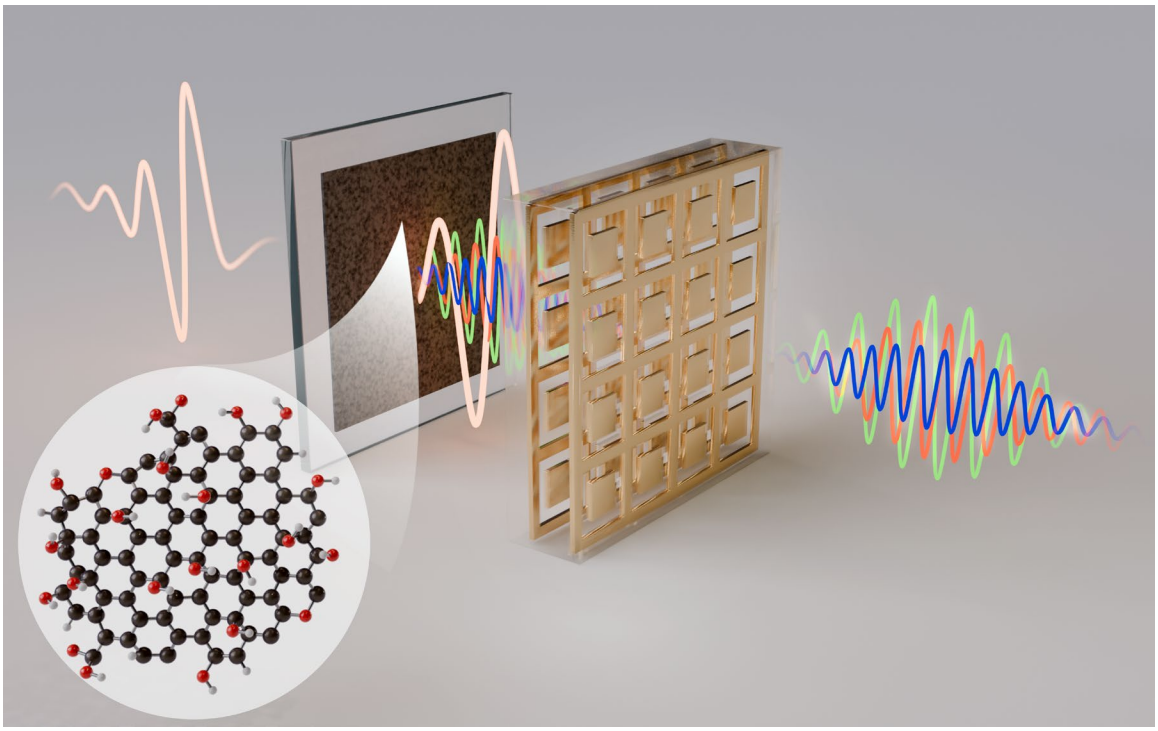

Figure 6.1 Schematic of the high-harmonic generation experiment in graphene oxide

6.1 Motivation and background

In Chapter 5, we presented a comprehensive strategy to enhance the nonlinear optical response of graphene-based systems in the THz regime. Specifically, we demonstrated that third-harmonic generation (THG) in graphene can be significantly enhanced by employing three key approaches: (i) increasing the light–matter interaction length through stacked multilayer graphene sheets with

reduced interlayer coupling; (ii) using electrical gating to tune the carrier density and access regimes of higher nonlinear conductivity; and (iii) implementing hybrid architectures that combine graphene with plasmonic metasurfaces, enabling local field enhancement. Through these methods, we achieved a two-orders-of-magnitude increase in THG efficiency, establishing a platform capable of detecting and manipulating weak nonlinear signals in 2D materials using a table-top THz system.

However, a fundamental limitation remains: the strong linear absorption of graphene in THz regime. As the number of stacked layers increases, propagation losses accumulate, restricting the effective interaction length. This trade-off results in an optimal configuration at around six to eight graphene layers, beyond which further stacking fails to yield additional THG enhancement. This absorption-limited saturation motivates the search for alternative materials or architectures that retain graphene's nonlinear strengths while minimizing loss.

To address this challenge, we now turn to graphene oxide (GO)—a functionalized derivative of pristine graphene (PG) where oxygen-containing functional groups (OFGs) such as hydroxyl, carboxyl, and epoxy groups are covalently bonded to the carbon lattice. GO is particularly attractive for nonlinear photonics due to its chemical tunability, ease of solution processing, compatibility with scalable fabrication techniques, and seamless on-chip integration. These practical benefits, coupled with its strong and adjustable optical response, position GO as a promising material platform for THz nonlinear optics.

From a photonics standpoint, GO offers significantly lower linear absorption in the THz regime compared to pristine graphene, enabling thicker films without the propagation losses encountered in multilayer stacks. At the same time, GO's third-order nonlinear susceptibility has been experimentally estimated to be on the order of $\chi^{(3)} \sim 10^{-10}\ m^2/V^2$, with nonlinear refractive indices (n_2) in the range of $(1.5–4.5) \times 10^{-14}\ m^2/W$, surpassing conventional semiconductors by several orders of magnitude [53,54]. These features make GO not only a testbed for studying fundamental

nonlinear interactions but also a viable platform for future THz photonic devices. Indeed, terahertz nonlinear optics is rapidly emerging as a powerful platform for strong-field light–matter interactions, offering an exciting opportunity to bridge the longstanding gap between high-speed electronics and integrated photonic functionality [7,8,11]. The work presented in this chapter contributes toward realizing this broader vision by demonstrating how tailored 2D materials can support coherent nonlinear processes in accessible THz-driven systems.

Here, we investigate the nonlinear optical response of GO and its reduced forms using a tilted-pulse-front THz source that delivers field strengths up to 260 kV/cm. Our goal is to determine whether GO, with its tunable absorption, local asymmetry, and low-loss characteristics, can support strong high-harmonic generation (HHG), potentially overcome the constraints seen in multilayer graphene, and establish a platform for exploring rich and tunable nonlinear optical processes. Our experiments reveal a striking nonlinear regime in GO, including:

- Generation of odd and even-like harmonics, and an interesting saturable transmission behavior in contrast to the single-threshold response of pristine graphene,
- A phenomenological two-level model that quantitatively captures the observed nonlinear transmission and HHG spectra.

These results establish GO as a versatile nonlinear platform that enables a THz-driven dynamical response fundamentally distinct from that of centrosymmetric graphene. Notably, we identify saturable transmission as a key mechanism underlying the observed nonlinear effects, paving the way for reconfigurable harmonic generation and wave-mixing processes in 2D systems.

The complete experimental study is presented in the manuscript included in this chapter: *"Non-perturbative THz nonlinearities in graphene oxide resulting in even and odd harmonics."*

This manuscript consolidates all experimental procedures, theoretical modeling, and supporting simulations required to understand the HHG behavior in GO, reduced GO, and highly reduced GO.

In Chapter 7, we return to these findings to discuss their broader implications for future device architectures and integrated nonlinear photonics in the THz regime, outlining how this research opens new directions at the intersection of materials science, ultrafast optics, and emerging photonic technologies.

Non-perturbative THz nonlinearities in graphene oxide resulting in even and odd harmonics

Ali Maleki,[1] Lu Wang,[1] Ilhem Bargaoui,[1] Hesam Heydarian,[1] Wei Cui,[1] Jean-Michel Guay,[2] Ksenia Dolgaleva,[3] Robert W. Boyd,[1,3,4] Thomas Brabec,[1] Jean-Michel Ménard[1,3,*]

[1]*Department of Physics, University of Ottawa, Ottawa, ON K1N 6N5, Canada*
[2]*Iridian Spectral Technologies Ltd, Ottawa, ON, K1G 6R8, Canada*
[3]*School of Electrical Engineering and Computer Science, University of Ottawa, Ottawa, ON K1N 6N5, Canada*
[4]*Institute of Optics and Department of Physics and Astronomy, University of Rochester, NY 14627, USA*

**Email: Jean-Michel Ménard (jean-michel.menard@uottawa.ca)*

Abstract

Recent advances in table-top high-field terahertz (THz) sources and spectral filtering techniques have enabled access to strong-field regimes in solid-state systems, allowing exploration of nonlinear dynamics beyond conventional symmetry constraints. Here, we report the generation of coherent even-like harmonics in graphene oxide (GO), a structurally disordered material lacking macroscopic inversion symmetry. Without invoking intrinsic or externally imposed symmetry breaking, we show that GO enters a non-perturbative nonlinear regime under intense THz excitation, exhibiting a distinctive double-plateau saturable transmission response. By developing a phenomenological two-level model informed by intensity-dependent transmission measurements, we demonstrate that this nonlinear behavior reshapes the HHG spectrum through multi-wave mixing, enabling the emergence of even-like harmonics. Our results reveal saturable transmission as an unconventional pathway for harmonic generation beyond conventional symmetry constraints in 2D graphitic materials, opening routes toward ultrafast optoelectronic control and reconfigurable THz photonic platforms.

Introduction

Terahertz (THz) nonlinear optics is emerging as a powerful platform for investigating low-photon-energy, strong-field light–matter interactions, notably offering new opportunities to bridge the gap between high-speed electronics and photonic functionalities[1–3]. In this regime, where individual photon energies are far below electronic bandgaps, nonlinear phenomena are dominated not by resonant multiphoton excitation, as in the near-IR, but by strong-field–induced carrier dynamics such as carrier heating from intraband acceleration of residual carriers and transient symmetry breaking[4–6] . These processes unfold on ultrafast timescales and govern carrier transport,

nonlinear optical interactions, and broadband frequency conversion processes that underpin emerging ultrafast optoelectronic and THz photonic technologies.

Among the many nonlinear effects accessible in this regime, high-harmonic generation (HHG) serves as a sensitive probe of material symmetry, ultrafast carrier dynamics, with sub-cycle carrier acceleration and scattering under the driving field, revealing key aspects of light–matter interactions[7,8]. Even-order HHG, such as second harmonic generation (SHG), is typically forbidden in centrosymmetric materials due to dipole selection rules [9,10]. However, this constraint can be relaxed by introducing mechanisms that locally or macroscopically break inversion symmetry. Well-known examples include symmetry breaking at interfaces between different media[7], strain-induced asymmetry[4,11], or the application of external electric fields—such as static biasing or THz-induced symmetry distortion[12–14]. These effects give rise to SHG and other even-order nonlinear response. In the absence of such symmetry breaking, spectral components at even harmonics interfere destructively and cancel out. This is particularly important in time-resolved THz detection schemes with electro-optic sampling, which are sensitive only to phase-locked spectral components; any incoherent or phase-randomized contribution averages to zero in the measured signal.

These symmetry-breaking mechanisms typically arise in the perturbative regime, where the nonlinear polarization can be described by a power-series expansion. In contrast, the non-perturbative regime—characterized by carrier heating[9], high-field carrier dynamics[15] , and saturation effects[16]—requires high-intensity THz excitation. Such high THz fields can be produced with tilted-pulse-front techniques in $LiNbO_3$[17], surface phase gratings[18], air-plasma sources[19], or free-electron based superradiant sources[20]. Table-top THz sources, though more accessible than large scale facilities, often produce broadband spectra that hinders harmonic detection. This challenge has been addressed through spectral filtering, which first narrows the excitation spectrum and subsequently suppresses the pump background to reduce the overall noise, thereby facilitating clearer detection of high-frequency spectral components[21]. Recent advances in harnessing intense THz sources and sensitive detection techniques have enabled experimental access to these strong-field regimes in condensed matter systems, paving the way for systematic exploration of nonlinear optical processes in tailored material platforms[21,22].

Graphene oxide (GO), a derivative of graphene (G), offers a chemically versatile platform with tunable optical response, scalable and on-chip fabrication[23–25]. GO's unique combination of

optical, electrical, and chemical characteristics arises from its layered carbon network decorated with oxygen-containing functional groups (OFGs), such as hydroxyl, carboxyl, and carbonyl groups[26,27]. Reduction of these functional groups enables for remarkable tunability of the bandgap, ranging from 0.1 to 3.6 eV, enabling control over material properties such as refractive index, optical absorption, and electrical conductivity[28].

In the THz regime, these properties translate into intriguing behaviors. Reduced GO films exhibit broadband THz absorption[29] and high conductivity (~900 S/cm)[30], which can be fine-tuned through reduction levels, film thickness, and optical pumping[31]. Optically pumped GO displays increased photoinduced conductivity along with a peculiar non-Drude relaxation behavior[32], unlike graphene and highly reduced GO (hrGO). The ultrafast relaxation dynamics in hrGO are primarily governed by carrier–carrier scattering and carrier–phonon coupling. These features have motivated the use of GO and its derivatives in THz devices, including absorbers [29], anti-reflection coatings[33], and sensors[34].

The heterogeneous atomic structure of GO also imparts remarkable nonlinear optical properties[35]. For instance, experimental studies have reported third-order optical nonlinearity (n_2) and a nonlinear absorption coefficient (β) for GO at 1550 nm, in the range of (1.5-4.5) × 10^{-14} m^2 W^{-1} and -5.3 × 10^{-8} m W^{-1}, respectively [36,37]. These values indicate that GO's nonlinear refractive index exceeds that of silicon by more than four orders of magnitude, though it remains approximately five times lower than that of graphene [36,38,39]. A wide range of nonlinear optical processes, such as saturable absorption[40,41], self-phase modulation[42], four-wave mixing[43], multiphoton absorption and luminescence [44,45] have been demonstrated in GO and its reduced forms.

Furthermore, saturable absorption (SA) in GO can also plays a significant role in strong-field regimes where the incident fluence approaches or exceeds the material's saturation threshold[9,46,47]. SA has been theoretically shown to contribute to HHG, with a saturable nonlinearly driven harmonic oscillator model accurately reproducing quantum mechanical predictions for harmonic generation[16]. As such, SA not only governs the efficiency of harmonic generation, but also provides window into unconventional mechanisms for light–matter interaction in disordered graphitic materials.

In this work, we employ GO and its reduced forms as a versatile platform to investigate field-driven nonlinear processes in the THz regime. Using a table-top high-field THz source, we explore

how structural tunability, through the reduction of oxygen functional groups and variation in film thickness, modulates the nonlinear optical response, particularly harmonic generation. Our experiments reveal strong higher-order harmonics in GO films, surpassing in amplitude those observed in multilayer graphene (G), and the emergence of wave mixing effects that give rise to spectral components at even harmonic positions, indicative of symmetry-breaking and/or complex nonlinear dynamics. Through power-dependent THz transmission measurements, we uncover a double-plateau saturable transmission behavior in GO, in contrast to the single-threshold response in G. To interpret these findings, we construct a two-level system model that captures the observed dual-saturation dynamics and accurately predicts the harmonic generation, offering a quantitative match with our measurements without invoking symmetry breaking. These results establish GO as a practical and tunable platform for probing strong-field THz nonlinearities and wave-mixing phenomena. Moreover, it demonstrates a nonlinear system able to transfer energy at even harmonic positions without relying on symmetry breaking. This capability has implications for advancing ultrafast optoelectronic components that bridge high-speed electronic and photonic functionalities. For instance, SA-driven nonlinear effects could be used to extend GHz electronic sources into the THz regime through integration of these materials in resonators or waveguides to enable compact, on-chip frequency converters.

Results

A schematic of the GO structure and the HHG experiment is shown in Figure 1. GO is chemically characterized by carboxylic acid groups primarily attached to the sheet edges, while hydroxyl and epoxy groups decorate the basal plane. GO thin films are prepared with a spray-coating technique. The reduction process removing OFG is chemically performed with hydrazine hydrate to produce reduced graphene oxide (rGO). Further annealing at 800 ºC is used to produce a hrGO sample. More details are provided in the Method section. Raman spectra confirm the different chemical structure of GO, rGO and hrGO showing a gradual reduction of oxygen functional groups and partial restoration of sp^2 carbon domains. Characteristic changes in the D, G, and 2D bands—including sharpening of the 2D band and a decreasing ID/IG ratio in hrGO—indicate increasing structural order and the formation of graphene-like regions[26,27]. Full spectral analysis and deconvolution of additional disorder-related bands (D′, D″, I, D+D′, 2D′) are provided in Section S1 of the Supplementary Information.

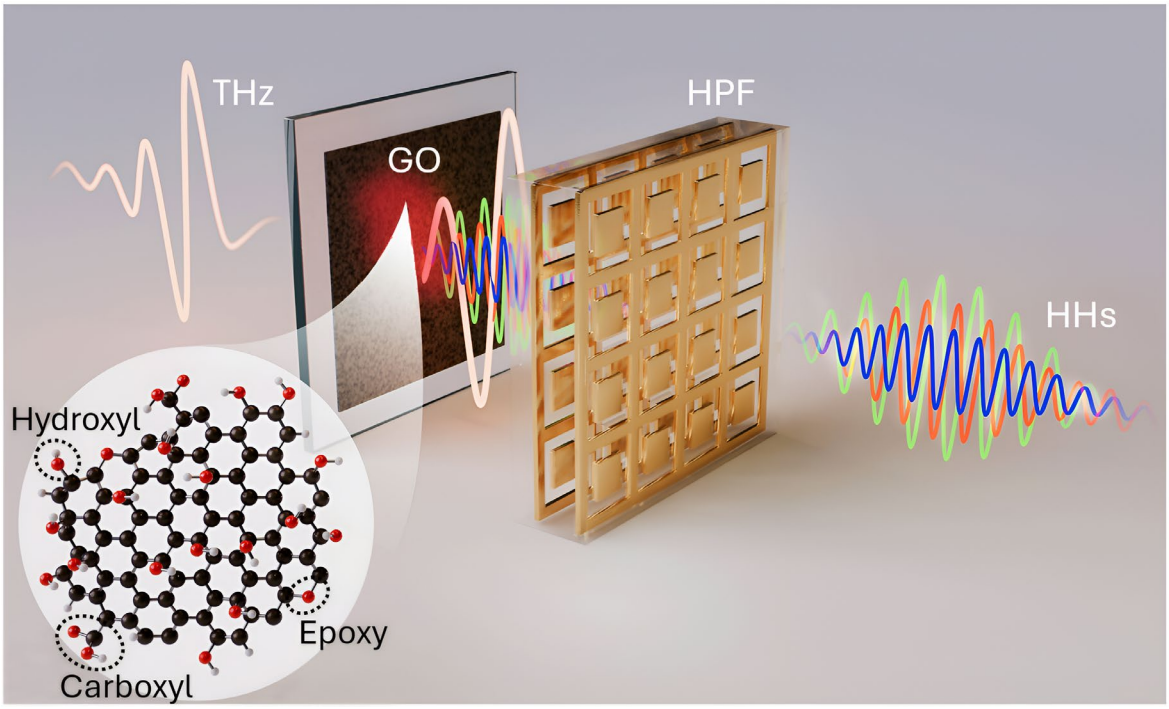

Fig. 1 Schematic of the HHG experiment and graphene oxide (GO). A terahertz (THz) pump pulse centered at 0.37 THz impinges on the GO film with a peak field strength of 30 kV/cm. Nonlinear interactions generate high-order harmonics (HHs). A highpass filter (HPF) suppresses the driving pump pulse and passes HHs to improve detection sensitivity. GO flake containing oxygen-functional groups: carboxyl, hydroxyl, and epoxy. GO flakes are spray coated on a THz transparent substrate to form a 200 nm-thick film.

A table-top time-resolved THz setup generating high-field multi-cycle phase-locked THz waves is used to investigate HHG in different graphitic materials. A highpass filter (HPF) after the sample suppresses the incident pump pulse by 3 orders of magnitude, reducing the noise and enabling sensitive time-resolved detection of nonlinear components at frequencies higher than the pump (see Section 2 in the Supplementary Information)[48]. The general HPF design is described in previous work[49] and its spectral transmission is shown in Section 2 of the Supplementary Information.

High harmonic generation (HHG) driven by intense THz fields is first performed in a 200 nm-thick GO layer and we compare this response to results obtained with six decoupled layers of CVD-grown graphene (6G). Figure 2a shows the transmitted THz spectra from these materials within the 0.7–2.1 THz range, defined by the high-pass filter transmission window. Figure 2b

shows the time-resolved THz pump pulse, resolved by electro-optic sampling, with a peak field of 30 kV/cm and a central frequency of 0.37 THz. This pump pulse interacts with the nonlinear graphitic samples, resulting in the generation of high harmonics resolved up to the 5^{th} order, with field strengths in the range of tens of V/cm. The high-harmonic waveforms are extracted by numerically applying spectral bandpass filters around each harmonic peak in the measured spectrum, followed by an inverse Fourier transform (Fig. 2c). This approach enables precise isolation of individual harmonic components and reconstruction of their time-domain profiles.

The HHG spectrum measured with the 6G sample (black line) shows odd-order harmonics consistent with the dipole-selection rules imposed by a centrosymmetric structure. These harmonics are significantly above the system's electronic noise floor (grey area). The same 6G sample was also used in previous work focusing on enhanced third-harmonic generation[21]. In comparison, results obtained with the GO sample displays a larger nonlinear response, with prominent odd harmonics and a clear spectral feature at the even harmonic position. The third and fifth harmonic peaks in GO (around 1.2 and 1.7 THz) are approximately twice as strong as those observed in 6G. More importantly, GO exhibits a distinct spectral peak near 1.55 THz—absent in the 6G spectrum—that coincides with the nominal position of the fourth harmonic. The emergence of this even-order harmonic is unexpected, as the random distribution of GO flakes during fabrication leads to centrosymmetric characteristics at the scale of the THz spot size. We investigate the spatial inhomogeneity of the GO thin film by collecting measurements at five lateral positions on the sample separated by ~1 mm. The even-like harmonic intensity exhibits a fluctuation of 17% (standard deviation), comparable to the one observed for odd-order harmonics (10%) (see Supplementary Information, Section S3). These variations likely stem from the non-uniform distribution of OFGs, local thickness variations, and inhomogeneities in doping and electronic transport properties. Similarly, the 6G sample yields lower harmonic intensity fluctuations (6%), arising from minor imperfections in layer transfer and stacking; these are far less pronounced than in GO, where flake-based deposition inherently produces larger spatial variations in thickness, doping, and functional group distribution. [50]. Interestingly, phase-resolved analysis of the fourth harmonic component at different lateral positions on the GO sample reveals that these components have the same phase (see Supplementary Information, Section S5).

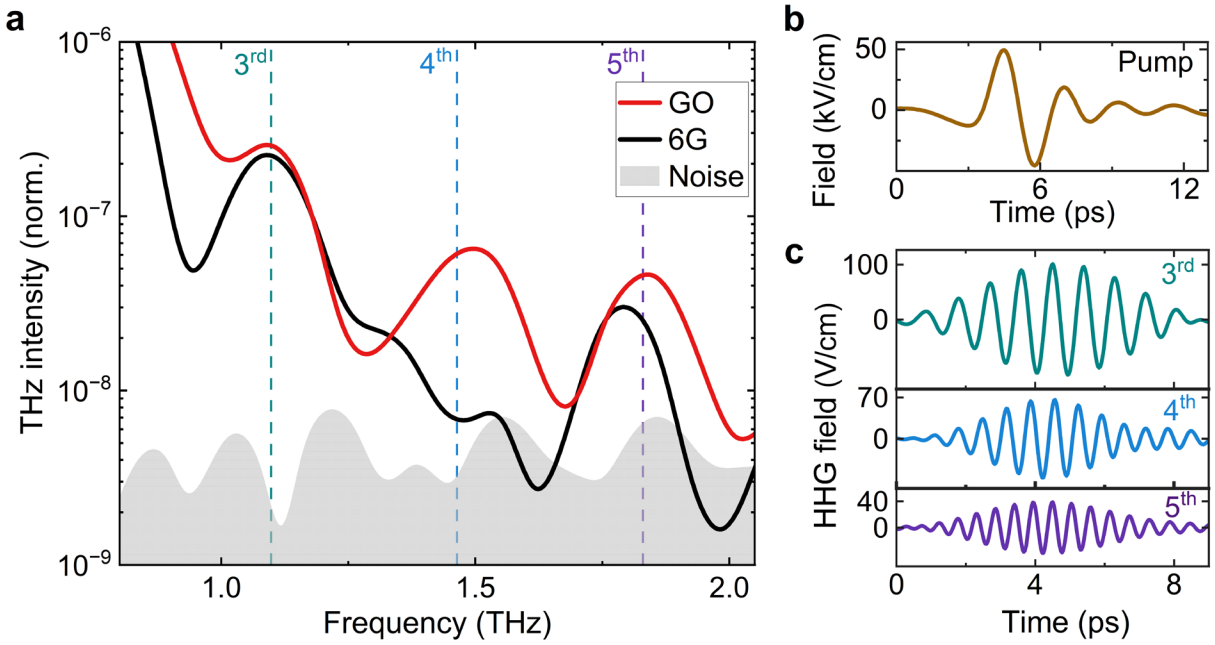

Fig. 2 THz high-harmonic generation (HHG) in GO. a Measured HHG spectrum generated in a 200 nm-thick film of graphene oxide (GO) (red line) and compared to the spectrum generated in a sample of 6 decoupled graphene layers (6G) (black line). The gray-shaded region shows the noise floor (no THz). **b** Time-domain waveform of the THz pump field. **c** Temporal waveforms of the generated harmonics in GO, reconstructed by applying numerical bandpass filters around individual harmonic frequencies followed by inverse Fourier transformation.

Previous work, such as powder second harmonic, also reported second-order nonlinear effects in centrosymmetric materials[42,49,50]. However, the mechanism at play in these experiments is local symmetry breaking, which can either be resolved spatially with an imaging technique or inferred from residual effects. In either case, these techniques produce a second-order nonlinear signal characterized by large spot-to-spot intensity variations and a phase determined by the orientation of the local asymmetry in the excitation region. In contrast, our experiments exhibit only modest spot-to-spot fluctuations in the even-like harmonic amplitude, and, more importantly, the phase of the harmonic components extracted from time-resolved measurements remains constant (see Section 5 in the Supplementary Information), indicating a fundamentally different mechanism that does not rely on localized symmetry breaking. The observation of non-perturbative nonlinear effects leading to even-like harmonic generation is made possible by our use of a field-resolved detection technique. Measurements collected with an intensity-based detection method might have led to the alternative interpretation that even-order harmonics arise from randomly distributed non-

centrosymmetric regions. Instead, our phase-resolved THz measurements show that, regardless of the specific excited region on the sample, the phase of the 4th harmonic remains constant.

To further examine the origin of the even-like harmonics observed in GO, we investigated the influence of OFGs and film thickness on the nonlinear response. Figure 3a compares the HHG spectra of GO with its reduced derivatives, rGO and hrGO. The GO (red line) and rGO (purple line) samples have the same 200 nm thickness and yield a comparable HH spectrum. Meanwhile, the hrGO spectrum (dark yellow line) is largely defined by odd-order harmonics, with negligible spectral amplitude observed at the fourth harmonic, which is within the noise level. The similarity between this result and the one obtained with 6G can be attributed to the progressive removal of OFGs during thermal reduction of GO, which partially restores sp² carbon domains. This process also increases the linear absorption of hrGO to values close to that of graphene, ~10% per layer in the THz range[47,51,52]. Therefore, a 50 nm hrGO film thickness is used, instead of the 200 nm thickness used for other samples, to prevent significant attenuation of the driving field and propagating HH components.

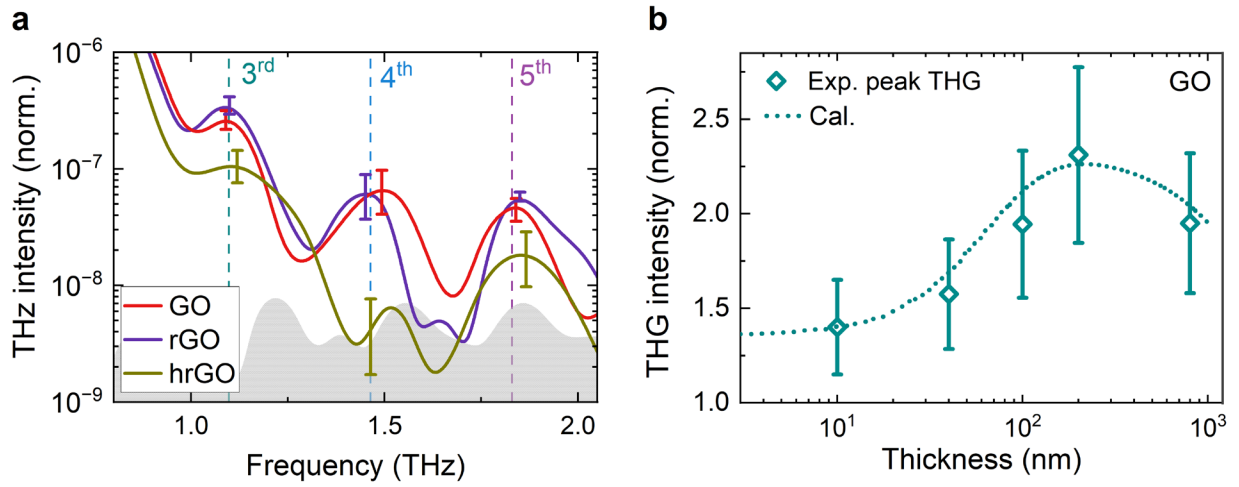

Fig. 3 Comparison of HH spectrum generated in GO thin films. a, Measured HHG spectra for three types of graphitic films: graphene oxide (GO, 200 nm thick), reduced graphene oxide (rGO, 200 nm thick), and highly reduced graphene oxide (hrGO, 50 nm thick). Within our detection window, GO and rGO produce odds and even-like harmonics, while only odd harmonics are produced by hrGO. For frequencies <0.8 THz, the incident pump is strongly attenuated by the HPF to resolve HHG with enhanced sensitivity. Therefore, we show only the higher frequency region of this measurement. **b**, Peak intensity of the third harmonic (THG) generated in GO as a function of film thickness. The dashed line represents the calculated

THG intensity. In **a** and **b**, the error bars represent the standard deviation from measurements collected on five different spots of the same sample.

We also explored the thickness dependence of third harmonic generation (THG) in GO films ranging from 10 nm to 800 nm, as shown in Fig. 3b. The THG intensity increases with thickness up to ~200 nm, beyond which it gradually declines. This trend reflects a competition between the effective interaction length and absorption losses: thinner films provide insufficient volume for nonlinear interactions, while in thicker films, increased linear absorption attenuates the generated HH components as well as the driving THz field, thereby limiting harmonic generation efficiency. This behavior is consistent with our previous findings in multilayer CVD-stacked graphene, where THG efficiency saturated beyond 6–8 layers due to linear absorption-dominated limitations[21]. The calculated thickness-dependent THG (dotted line in Fig. 3b) is obtained using a model that incorporates the measured absorption coefficient $\alpha_{GO}(\Omega \approx 0.37\ \text{THz}) = 164 \pm 11\ \text{cm}^{-1}$ at the driving frequency. We obtain a good agreement with experimental data when considering a slightly higher absorption coefficient at the third harmonic, $\alpha_{GO}(\Omega \approx 1.1\ \text{THz}) = 170 \pm 12\ \text{cm}^{-1}$, which could possibly account for additional losses due to phonon absorption.

To investigate the mechanism underlying the even-like harmonic generation, we characterize the saturable absorption behavior of GO, rGO and 6G as a function of the driving field amplitude. This response, when applied to the time-resolved THz transients, can then be used to model the optical nonlinear response. Accurately extracting transmission as a function of THz field amplitude is experimentally challenging, primarily because the driving field inherently spans a continuous range of amplitudes. Moreover, saturable absorption can exhibit temporal dependence, further complicating the analysis. To address this, we opted to characterize the transmission behavior specifically at the peak field amplitude. While this approach constitutes an approximation, it is justified by the shape of our THz transient, which suggests that time-dependent nonlinear contributions from earlier portions of the pulse are comparatively minor. Figure 4 shows the transmission at the peak field position as a function of the peak field amplitude incident on GO, rGO (Fig. 4a) and 6G (Fig. 4b). GO and rGO feature a gradual increase in transmission from 0.3 kV/cm up to a plateau between ~2 and 40 kV/cm followed by another increase in transmission, which must also reach a plateau beyond 260 kV/cm, the maximum field used in our experiment.

This multi-step behavior points to complex nonlinear effects beyond a perturbative approach based on a power expansion of the polarization term with the applied electric field. In contrast, 6G (black line in Fig. 4b) features a transmission response characterized by a gradual increase in transmission starting at ~1 kV/cm and saturating beyond 200 kV/cm. This transmission is consistent with the one reported for monolayer graphene[51] (dotted gray line), however, multiple layers enhance absorption, leading to an overall reduction in transmission and an earlier onset of the saturation behavior. We used a model based on a two-level system to capture the transmission response[7] (see Section 4 in the Supplementary Information for mathematical derivation). The model fits to the experimental data are shown as plain lines in Fig. 4a and b.

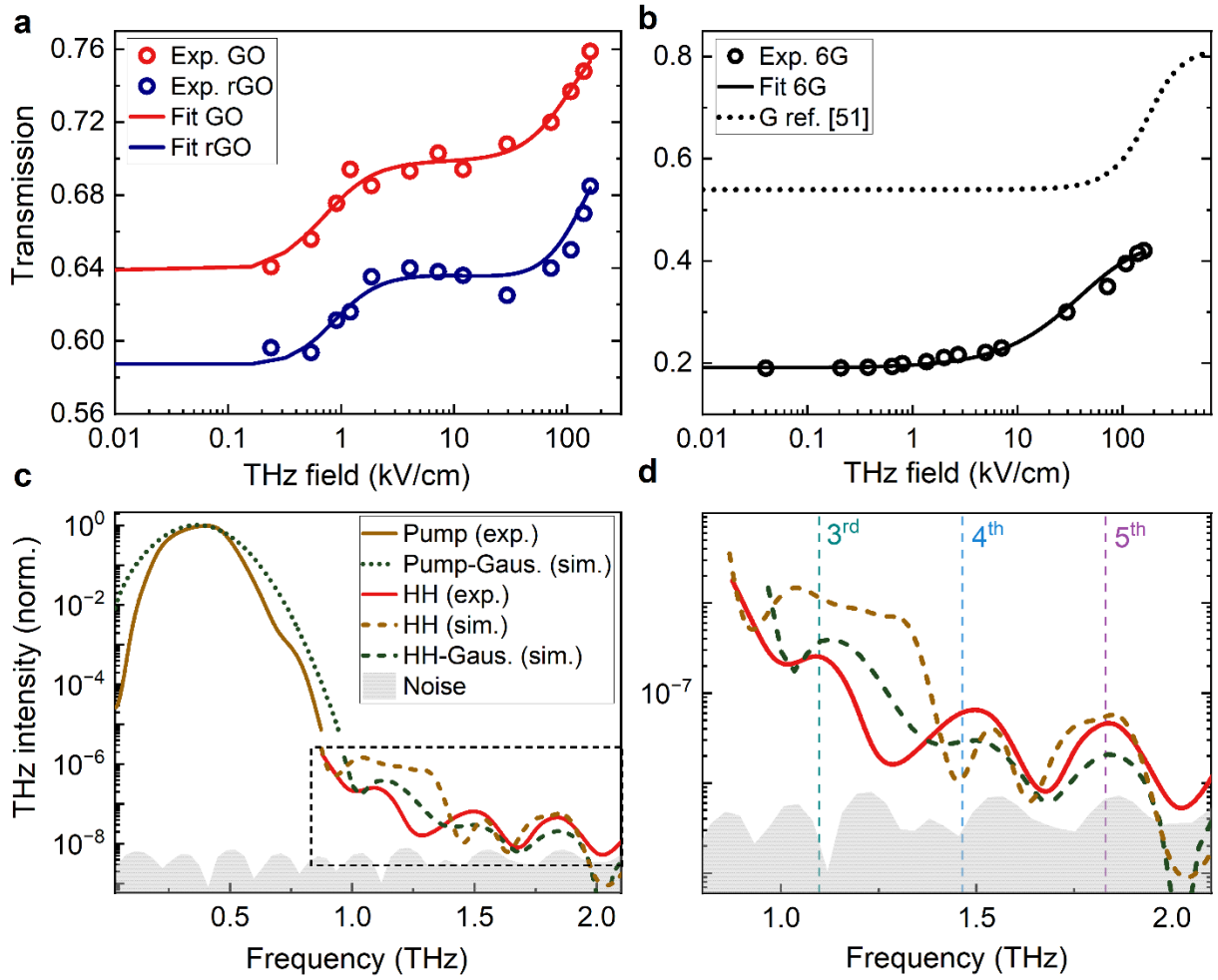

Fig. 4 Measured saturable transmission to model high harmonic generation. a. Measured THz transmission in GO (red circles) and rGO (blue circles) as a function of the driving peak field amplitude with corresponding fits based on a two-level saturable transmission model (lines). **b.** Same measurements

performed with 6G (black line) compared to transmission measurement in monolayer graphene[51] (dotted grey line). **c** Comparison between the incident measured pump (dark yellow), Gaussian pump (green), experimentally measured HH (red) and simulated HHs (dashed lines) in GO, for various pulse shapes. Simulations are performed using the experimental pump (dark yellow) and a Gaussian pump (HH-Gaus., green), reproducing the emergence of both odd and even-like harmonics. Zoomed-in view of the high-frequency region.

Using the fitted transmission data of GO, we simulate the THz-driven HHG spectra by applying the saturable transmission response to the measured time-resolved THz driving field. Figure 4c shows the incident driving field spectrum (dark yellow line), the measured HHG (red line) and the simulated results (dashed lines) obtained by applying a Fourier transform to the time-domain THz driving field, which is modulated by the saturable transmission function. Simulations are performed using two different driving fields: the measured experimental pump (dark yellow) and a Gaussian pump closely following the experimental curve (green). A zoomed-in view of the higher frequency components is shown in Fig. 4d. Remarkably, the simulated HHG from GO reproduces the experimental spectrum, including the even-like harmonic at 1.45 THz, with slight discrepancies. These discrepancies may be attributable to uncertainties in the measured saturable transmission, arising in part from spatial inhomogeneity of the sample, differences between the positions used for HHG and saturable-transmission measurements, and variations in the measured driving pump. For a standard saturable absorber such as graphene, the transmission response in Fig. 4b can be expanded in power series of the optical field containing only odd terms, leading to odd harmonic generation only. The agreement between experiment and simulations confirm that the observed HHG in GO, including even-like harmonics, can be effectively captured with a multi-step saturable transmission, without requiring structural inversion symmetry breaking.

We investigate harmonic generation with numerical simulations by varying key driving pulse parameters such as the duration, carrier-envelope phase (CEP), and peak power (see Figs. S6 to S8 in the Supplementary Information). In GO, the even-like harmonics only significantly emerge when the field amplitude reaches the first transmission plateau at 2 kV/cm. Only odd harmonics are generated for lower peak fields, indicating that this transmission response can be linked to the onset of even-like harmonic generation. We observe that longer THz pulse durations, which correspond to narrower spectral bandwidths, do not produce even-like harmonics. In contrast,

shorter pulse durations facilitate the emergence of spectral features between odd harmonics, consistent with a wave mixing behavior. CEP variations also affect the amplitude and symmetry of even-like harmonics, in agreement with previous findings where CEP can be used to modulate the amplitude and shape of the different harmonics[53–55].

Our experimental and simulation results show that the generation of even-order harmonics in GO is primarily governed by a multi-step saturable transmission response. Unlike the conventional nonlinear polarization response, which relies on a power series expansion of the electric field, this mechanism exhibits a fundamentally different, non-perturbative behavior. Moreover, this mechanism leading to even-like harmonics stands in contrast to traditional symmetry-breaking or non-dipole-based HHG processes. In brief, the multi-step saturable response in GO enables conditions under which multi-wave mixing between harmonic components becomes feasible, effectively producing even-like harmonics in a medium without requiring a net structural asymmetry.

Conclusion

We investigated high-harmonic generation (HHG) in graphitic materials and revealed a striking nonlinear optical response in graphene oxide (GO), characterized by the emergence of an even-like harmonic, which is typically forbidden in centrosymmetric materials. Through a combination of THz transmission measurements, HHG spectroscopy, and saturable transmission (ST) modelling, we identified a distinctive multi-step behavior of ST in GO that plays a central role in enabling this response. We demonstrate that the observed even-like harmonic do not stem from symmetry breaking but rather from a non-perturbative nonlinear response dictated by a two-level saturable absorption process. These findings establish saturable transmission as a powerful mechanism for driving high-field nonlinearities in 2D materials. To fully exploit such nonlinear effects for frequency conversion, more work is required to identify the origin of this multi-level saturable absorption. The SA observed in GO is clearly transient on sub-millisecond timescales, as the response recovers between successive excitation pulses at a kHz repetition rate, but its exact dynamics cannot be extracted from our measurements. Its microscopic origin—whether primarily electronic, phononic, or mixed— could be investigated with THz pump - THz probe experiments. Two potential mechanisms could explain the multi-step SA: a spatially decoupled system featuring saturable absorption at different field amplitudes, and a three-energy-level system with the two

first excited levels starting to feature saturable absorption behavior, but only after the first excited level is strongly populated. Beyond advancing the general understanding of HHG in 2D materials, our results open new pathways for dynamically reconfigurable THz photonic components—including frequency converters, ultrafast modulators, and logic devices—potentially bridging the gap between high-speed electronics and nonlinear optics in thin film platforms.

Materials and methods

Sample preparation.

We use a home-made spray coating technique to deposit GO samples onto substrates (see Section S8 in the Supplementary Information). The setup employs an airbrush (VH174, VIVOHOME) operating at an air pressure of 30 kPa, with a hot plate beneath the sample heated to 150 °C to evaporate the solvent during deposition. A nanocolloidal solution of GO in water (Sigma Aldrich) is prepared at a concentration of 0.5 mg/mL and ultrasonicated for 30 minutes at room temperature to ensure uniform dispersion. The GO solution is then spray-coated onto quartz substrates heated to 150 °C, forming uniform thin films. To fabricate rGO, the GO solution is chemically reduced using a hydrazine hydrate liquid route. Hydrazine hydrate (N_2H_4) is a widely used reducing agent, capable of efficiently removing functional groups attached to both the basal plane and edges of GO. A nanocolloidal GO dispersion (0.5 mg/mL, Sigma Aldrich) is mixed with pure hydrazine hydrate (Sigma Aldrich) at a ratio of GO: N_2H_4 = 1:0.04 (4% of GO volume). The precursor solution rests for 24 hours, during which its color changes from dark brown to black, indicating the formation of suspended rGO. The resulting dispersion is sonicated for 30 minutes at 40 kHz to facilitate the mechanical exfoliation of rGO layers.

To obtain hrGO samples, the rGO samples are thermally reduced by heating them to 800 °C in an oven under a nitrogen atmosphere to effectively remove oxygen-containing functional groups (OFGs). This thermal reduction process ensures a significant reduction in defects and an enhancement of graphene-like properties. This fabrication process provides precise control over the thickness and reduction levels of the samples, enabling a systematic investigation of their nonlinear optical properties. Further details on the spray coating and reduction methods can be found in our previous publication[56]. The total sample thickness is maintained significantly below the wavelength of the incident THz radiation, eliminating the requirement for phase matching to achieve coherent nonlinear effects. For the fabrication of a 6-layer graphene sample, commercial

monolayer CVD-grown graphene on copper foil, coated with a poly(methyl methacrylate) (PMMA) layer, is obtained from Graphenea. Graphene layers measuring 1 cm × 1 cm are wet-transferred onto a 188 μm-thick Zeonor substrate, followed by the deposition of a 60 nm-thick Al_2O_3 layer using an electron-beam evaporator (Nexdep Series, Angstrom). This process is repeated to create a stack of 6 graphene layers, each separated by a 60 nm-thick Al_2O_3 layer[21].

Experiment

Intense THz radiation is generated using optical rectification in a lithium niobate ($LiNbO_3$) crystal[55], where the tilted-pulse-front technique was implemented to achieve phase matching. A Ti:sapphire laser operating at 800 nm with a pulse duration of 45 fs and a repetition rate of 1 kHz, serves as the pump source. The resulting single-cycle THz pulse reaches a peak electric field strength of 260 kV/cm. Electro-optical sampling is performed using a 500-μm-thick ZnTe crystal to detect the transmitted THz field. A bandpass filter (BPF) is employed to decrease the spectral bandwidth of the pump pulse and attenuate spectral components beyond 1.1 THz by approximately 50 dB (see section S2 in the Supplementary Information for details). A pair of free-standing wire-grid polarizers is used to control the THz field strength without introducing dispersion. For low-field transmission measurements in the linear regime, we use a conventional THz time-domain spectroscopy (TDS) setup, where THz pulses are generated via optical rectification in a GaP crystal, producing field strengths well below 1 kV/cm. All experiments were conducted at room temperature inside a dry-air purged enclosure to eliminate water vapor absorption.

Conflict of interest

The authors declare no competing interests.

Data availability

The experimental data that support the findings of this work are available upon reasonable request from the corresponding authors.

Supplementary information

The Supplementary Information provides additional details on Raman spectroscopy measurements, the theoretical two-level saturation model, high-harmonic generation (HHG)

simulations, spectral filtering methods, HHG analysis using Gaussian pump pulses, and the fabrication process of graphene oxide structures.

Acknowledgements

We acknowledge funding from the Natural Sciences and Engineering Research Council of Canada (NSERC) Discovery (RGPIN-2023-05365) and Alliance (ALLRP 592522) funding program. This work was supported by Mitacs through the Mitacs Accelerate program (IT39338). The authors acknowledge the use of the LUXSc facility for experimental measurements. We thank B. Sullivan, G. Flizikowski, S Aghili for insightful discussions and technical support.

References

1. Hafez, H. A. *et al.* Terahertz Nonlinear Optics of Graphene: From Saturable Absorption to High-Harmonics Generation. *Adv Opt Mater* **8**, (2020).
2. Chai, X. *et al.* Subcycle Terahertz Nonlinear Optics. *Phys Rev Lett* **121**, 143901 (2018).
3. Nicoletti, D. & Cavalleri, A. Nonlinear light–matter interaction at terahertz frequencies. *Adv Opt Photonics* **8**, 401 (2016).
4. Hafez, H. A. *et al.* Extremely efficient terahertz high-harmonic generation in graphene by hot Dirac fermions. *Nature* **561**, 507–511 (2018).
5. Lu, K. *et al.* Strong second-harmonic generation by sublattice polarization in non-uniformly strained monolayer graphene. *Nat Commun* **14**, 1–8 (2023).
6. Vaswani, C. *et al.* Terahertz Second-Harmonic Generation from Lightwave Acceleration of Symmetry-Breaking Nonlinear Supercurrents. *Phys Rev Lett* **124**, 207003 (2020).
7. Kovalev, S. *et al.* Non-perturbative terahertz high-harmonic generation in the three-dimensional Dirac semimetal Cd3As2. *Nat Commun* **11**, 6–11 (2020).
8. Boyd, R. W. *Nonlinear Optics*. *Nonlinear Optics* (Elsevier, 2020). doi:10.1016/C2015-0-05510-1.
9. Schubert, O. *et al.* Sub-cycle control of terahertz high-harmonic generation by dynamical Bloch oscillations. *Nat Photonics* **8**, 119–123 (2014).

10. Kovalev, S. *et al.* Electrical tunability of terahertz nonlinearity in graphene. *Sci Adv* **7**, 1–10 (2021).

11. Lu, K. *et al.* Strong second-harmonic generation by sublattice polarization in non-uniformly strained monolayer graphene. *Nat Commun* **14**, 1–8 (2023).

12. Zhang, Y. *et al.* Doping-Induced Second-Harmonic Generation in Centrosymmetric Graphene from Quadrupole Response. *Phys Rev Lett* **122**, 47401 (2019).

13. An, Y. Q., Nelson, F., Lee, J. U. & Diebold, A. C. Enhanced optical second-harmonic generation from the current-biased graphene/SiO2/Si(001) structure. *Nano Lett* **13**, 2104–2109 (2013).

14. Grishunin, K. A. *et al.* THz Electric Field-Induced Second Harmonic Generation in Inorganic Ferroelectric. *Sci Rep* **7**, 1–8 (2017).

15. Hohenleutner, M. *et al.* Real-time observation of interfering crystal electrons in high-harmonic generation. *Nature* **523**, 572–575 (2015).

16. Varin, C., Bart, G., Emms, R. & Brabec, T. Saturable Lorentz model for fully explicit three-dimensional modeling of nonlinear optics. *Opt Express* **23**, 2686 (2015).

17. Hebling, J., Almasi, G., Kozma, I. & Kuhl, J. Velocity matching by pulse front tilting for large area THz-pulse generation. *Opt Express* **10**, 1161 (2002).

18. Cui, W., Awan, K. M., Huber, R., Dolgaleva, K. & Ménard, J. M. Broadband and High-Sensitivity Time-Resolved THz System Using Grating-Assisted Tilted-Pulse-Front Phase Matching. *Adv Opt Mater* **10**, (2022).

19. Dai, J., Liu, J. & Zhang, X.-C. Terahertz Wave Air Photonics: Terahertz Wave Generation and Detection With Laser-Induced Gas Plasma. *IEEE Journal of Selected Topics in Quantum Electronics* **17**, 183–190 (2011).

20. Green, B. *et al.* High-field high-repetition-rate sources for the coherent THz control of matter. *Sci Rep* **6**, (2016).

21. Maleki, A. *et al.* Strategies to enhance THz harmonic generation combining multilayered, gated, and metamaterial-based architectures. *Light Sci Appl* **14**, 1–10 (2025).

22. Lu, Y. *et al.* Nonlinear optical physics at terahertz frequency. *Nanophotonics* **13**, 3279–3298 (2024).

23. Wu, J., Lin, H., Moss, D. J., Loh, K. P. & Jia, B. Graphene oxide for photonics, electronics and optoelectronics. *Nat Rev Chem* **7**, 162–183 (2023).

24. Wu, J. *et al.* 2D Graphene Oxide Films Expand Functionality of Photonic Chips. *Advanced Materials* **2403659**, 1–14 (2024).

25. Zheng, X. *et al.* Highly efficient and ultra-broadband graphene oxide ultrathin lenses with three-dimensional subwavelength focusing. *Nat Commun* **6**, 1–7 (2015).

26. Dimiev, A. M. & Tour, J. M. Mechanism of Graphene Oxide Formation. *ACS Nano* **8**, 3060–3068 (2014).

27. Chen, D., Feng, H. & Li, J. Graphene oxide: Preparation, functionalization, and electrochemical applications. *Chem Rev* **112**, 6027–6053 (2012).

28. Loh, K. P., Bao, Q., Eda, G. & Chhowalla, M. Graphene oxide as a chemically tunable platform for optical applications. *Nat Chem* **2**, 1015–1024 (2010).

29. Sun, X. *et al.* Gradient-Reduced Graphene Oxide Aerogel with Ultrabroadband Absorption from Microwave to Terahertz Bands. *ACS Appl Nano Mater* **6**, 3893–3902 (2023).

30. Hong, J. T. *et al.* Terahertz conductivity of reduced graphene oxide films. *Opt Express* **21**, 7633 (2013).

31. Xing, X. *et al.* Photoinduced Terahertz Conductivity and Carrier Relaxation in Thermal-Reduced Multilayer Graphene Oxide Films. *Journal of Physical Chemistry C* **121**, 2451–2458 (2017).

32. Kim, J. *et al.* Unconventional terahertz carrier relaxation in Graphene oxide: Observation of enhanced auger recombination due to defect saturation. *ACS Nano* **8**, 2486–2494 (2014).

33. Zhou, Y. *et al.* Solution-processable reduced graphene oxide films as broadband terahertz wave impedance matching layers. *J Mater Chem C Mater* **3**, 2548–2556 (2015).

34. Sajeev, V. *et al.* Terahertz sensing of reduced graphene oxide nanosheets using sub-wavelength dipole cavities. *Sci Rep* **13**, 1–9 (2023).

35. Zhang, Y. *et al.* Graphene Oxide for Nonlinear Integrated Photonics. *Laser Photon Rev* **17**, 1–28 (2023).

36. Xu, X. *et al.* Observation of Third-order Nonlinearities in Graphene Oxide Film at Telecommunication Wavelengths. *Sci Rep* **7**, 1–7 (2017).

37. Zhang, Y. *et al.* Enhanced Kerr Nonlinearity and Nonlinear Figure of Merit in Silicon Nanowires Integrated with 2D Graphene Oxide Films. *ACS Appl Mater Interfaces* **12**, 33094–33103 (2020).

38. Steinberg, D. *et al.* Graphene oxide and reduced graphene oxide as saturable absorbers onto D-shaped fibers for sub 200-fs EDFL mode-locking. *Opt Mater Express* **8**, 144 (2018).

39. Zhao, X. *et al.* Ultrafast carrier dynamics and saturable absorption of solution-processable few-layered graphene oxide. *Appl Phys Lett* **98**, (2011).

40. Zhang, Y. *et al.* Enhanced Spectral Broadening of Femtosecond Optical Pulses in Silicon Nanowires Integrated with 2D Graphene Oxide Films. *Micromachines (Basel)* **13**, (2022).

41. Qu, Y. *et al.* Enhanced Four-Wave Mixing in Silicon Nitride Waveguides Integrated with 2D Layered Graphene Oxide Films. *Adv Opt Mater* **8**, (2020).

42. Russier-Antoine, I. *et al.* Second harmonic scattering from mass characterized 2D graphene oxide sheets. *Chemical Communications* **56**, 3859–3862 (2020).

43. Qian, J. *et al.* Observation of multiphoton-induced fluorescence from graphene oxide nanoparticles and applications in invivo functional bioimaging. *Angewandte Chemie - International Edition* **51**, 10570–10575 (2012).

44. Bianchi, V. *et al.* Terahertz saturable absorbers from liquid phase exfoliation of graphite. *Nat Commun* **8**, 15763 (2017).

45. Mics, Z. *et al.* Thermodynamic picture of ultrafast charge transport in graphene. *Nat Commun* **6**, 1–7 (2015).

46. Hafez, H. A. *et al.* Extremely efficient terahertz high-harmonic generation in graphene by hot Dirac fermions. *Nature* **561**, 507–511 (2018).

47. Maleki, A. *et al.* Metamaterial-based octave-wide terahertz bandpass filters. *Photonics Res* **11**, 526 (2023).

48. Rautela, R. *et al.* Mechanistic Insight into the Limiting Factors of Graphene-Based Environmental Sensors. *ACS Appl Mater Interfaces* **12**, 39764–39771 (2020).

49. Hwang, H. Y. *et al.* Nonlinear THz conductivity dynamics in P-Type CVD-grown graphene. *Journal of Physical Chemistry B* **117**, 15819–15824 (2013).

50. Scarfe, S., Cui, W., Luican-Mayer, A. & Ménard, J. M. Systematic THz study of the substrate effect in limiting the mobility of graphene. *Sci Rep* **11**, 1–9 (2021).

51. Krebs, M. *et al.* Towards isolated attosecond pulses at megahertz repetition rates. *Nat Photonics* **7**, 555–559 (2013).

52. Baltuška, A. *et al.* Attosecond control of electronic processes by intense light fields. *Nature* **421**, 611–615 (2003).

Supplementary information for

Non-perturbative THz nonlinearities in graphene oxide resulting in even and odd harmonics

Ali Maleki,[1] Lu Wang,[1] Ilhem Bargaoui,[1] Hesam Heydarian,[1] Wei Cui,[1] Jean-Michel Guay,[2] Ksenia Dolgaleva,[3] Robert W. Boyd,[1,3,4] Thomas Brabec,[1] Jean-Michel Ménard[1,3,*]

[1]*Department of Physics, University of Ottawa, Ottawa, ON K1N 6N5, Canada*
[2]*Iridian Spectral Technologies Ltd, Ottawa, ON, K1G 6R8, Canada*
[3]*School of Electrical Engineering and Computer Science, University of Ottawa, Ottawa, ON K1N 6N5, Canada*
[4]*Institute of Optics and Department of Physics and Astronomy, University of Rochester, NY 14627, USA*

**Email: Jean-Michel Ménard (jean-michel.menard@uottawa.ca)*

Section S1: Raman analysis of graphene oxide and its reduced forms

Raman spectroscopy is used to analyze the structural evolution of graphene oxide (GO), reduced graphene oxide (rGO), and highly reduced graphene oxide (hrGO) across both the first-order (1100–1900 cm^{-1}) and second-order (2400–3300 cm^{-1}) spectral regions. As shown in Fig. S1, in the first-order region, the spectra of all samples exhibit the characteristic D band (~1350 cm^{-1}), attributed to the breathing modes of sp^2 rings activated by structural defects, and the G band (~1580 cm^{-1}), associated with sp^2 carbon hybridizations. Additional peaks, including the D′ (~1620 cm^{-1}), D″ (~1500 cm^{-1}), and I (~1200 cm^{-1}) bands, are also observed and deconvoluted. These bands are commonly linked to amorphous carbon, and sp^3-hybridized domains, respectively[1,2]. Notably, the ID/IG intensity ratio (i.e., the ratio of the D- to G-band peak intensities) slightly increased from GO to rGO due to the formation of smaller but more numerous sp^2 domains, and then decreased for hrGO, indicating an improvement in graphitic order.

In the second-order region, the spectra reveal a prominent 2D band (~2700 cm^{-1}), which becomes sharper and more symmetric with increasing reduction, consistent with the recovery of extended conjugation and a reduction in defects. The D+D′ combination band (~2950 cm^{-1}), which is sensitive to disorder, is strongest in GO and significantly diminished in hrGO. The presence of the 2D′ band (~3200 cm^{-1}) and the D+D″ mode (~2450 cm^{-1}) further supports these observations, as both bands decrease in intensity upon reduction. These trends confirm the gradual transition from

a defect-rich, oxidized structure in GO to a more ordered, graphitic framework in hrGO, demonstrating the effectiveness of the reduction treatments.

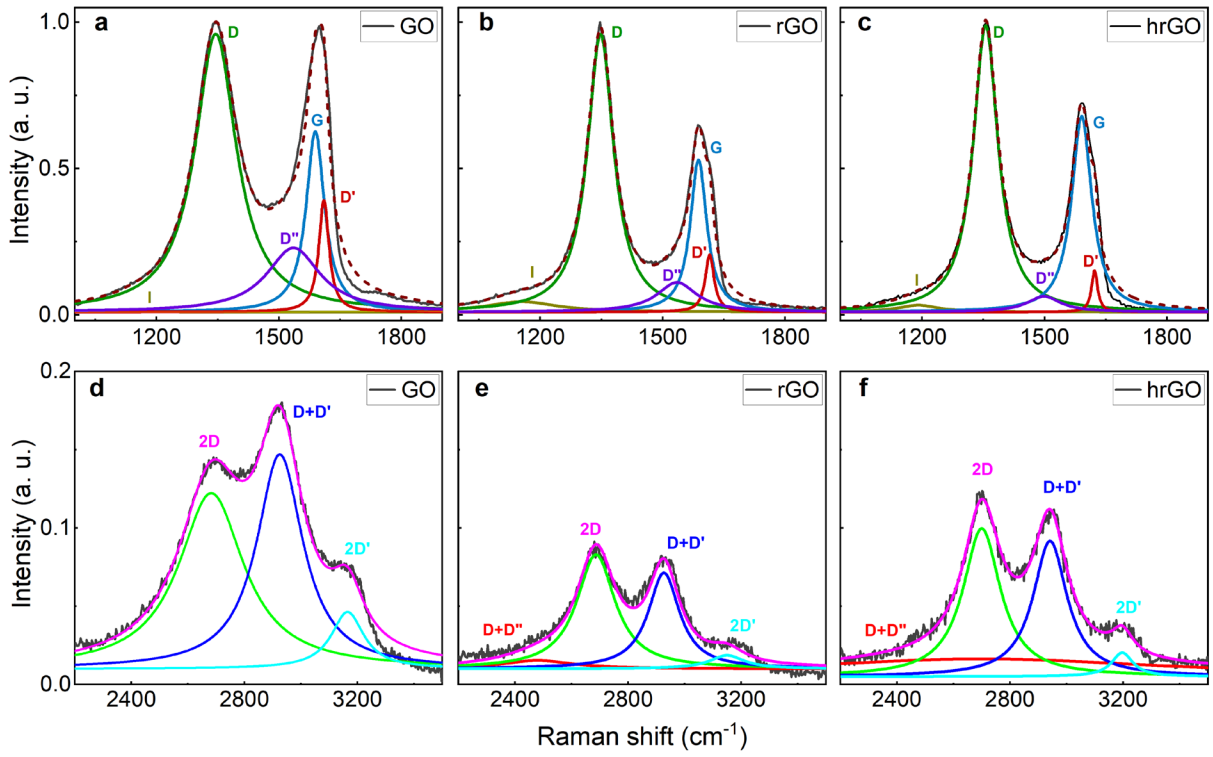

Fig. S1 Deconvoluted Raman spectra of graphene-based samples across first-order (top row: a–c) and second-order (bottom row: d–f) regions. Columns correspond to different materials: graphene oxide (GO, left), reduced graphene oxide (rGO, middle), and highly reduced graphene oxide (hrGO, right). Key Raman features, including D, G, D′, D″, I, 2D, D+D′, and 2D′ bands, highlight structural changes and disorder evolution during the reduction process.

Section S2: Spectral filters

Figure S2a presents the semilogarithmic transmittance profile of the highpass filter (HPF) used in our experimental setup. This filter efficiently transmits THz radiation in the 0.75–2 THz range with approximately 60% transmittance, while strongly attenuating low-frequency components below 0.5 THz by more than 40 dB, effectively suppressing the fundamental pump frequency. Figure S2b compares the THz intensity spectra of the filtered signals. The red curve corresponds to the pump pulse after passing through a bandpass filter (BPF) centered at 0.37 THz, which

defines our input excitation. The blue curve shows the spectrum after introducing the HPF into the beam path. As evident, the HPF suppresses the fundamental component (0.37 THz) by more than 40 dB while allowing higher-frequency harmonic signals to pass, thereby enabling clean detection of high-order harmonics.

Notably, the addition of the HPF significantly reduces system noise. The noise in pump is evident at the ~50 dB, while the addition of the HPF attenuates it to ~80 dB, reaching the background electronic noise of the setup. This region is indicated by the grey-shaded area in the plot, which marks the background noise level recorded with the THz beam blocked. Details on the structural features of the filters are reported in our previous work[3].

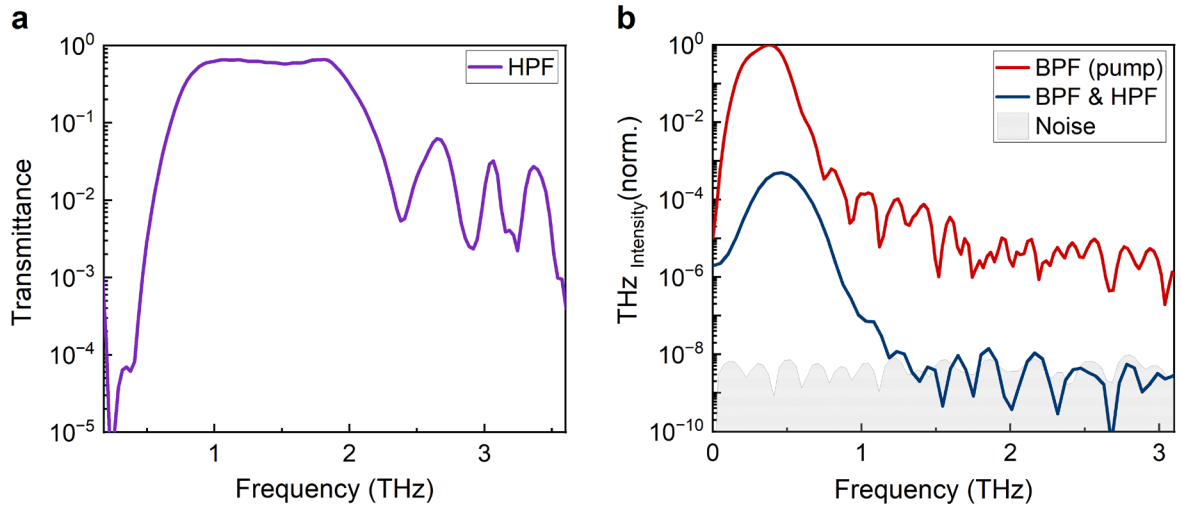

Fig. S2 Spectral characteristics of the THz filters. a Semilogarithmic transmittance spectrum of the highpass filter (HPF), showing strong suppression (> 40 dB) of low-frequency components below 0.5 THz and efficient transmission (~60%) in the passband range, 0.75–2 THz. **b** THz intensity spectra after different filtering stages: the red curve shows the pump spectrum after a bandpass filter (BPF), and the blue curve shows the spectrum after introducing the HPF in the beam path. The HPF effectively suppresses the pump frequency by over 40 dB and reduces the system noise floor down to background electronic noise (~80 dB). The gray-shaded region indicates the background electronic noise measured with the THz beam blocked.

Section S3: Power-dependent THz transmission of HHG

To investigate the field-dependent nonlinear response of graphene oxide (GO), we performed power-dependent THz transmission measurements using a pair of wire-grid polarizers in the THz beam path to precisely control the incident field strength. The peak electric field of the pump pulse is varied from 1 to 30 kV/cm. Figure S3a shows the time-domain waveforms of the driving THz pulses at different field strengths, while the corresponding generated HH spectra in GO samples, recorded after passing through the HPF, are shown in Fig. S3b. All spectra are normalized to the peak intensity of the driving pump at 30kV/cm. The dashed lines indicate the calculated 3rd, 4th, and 5th harmonics relative to the fundamental pump frequency (~0.37 THz). The strongest HHGs are observed at the maximum field strength of 30 kV/cm. As the field strength decreases, the harmonics' intensity gradually diminishes, and at low fields (< 6 kV/cm), the generated signals fall to the background noise level.

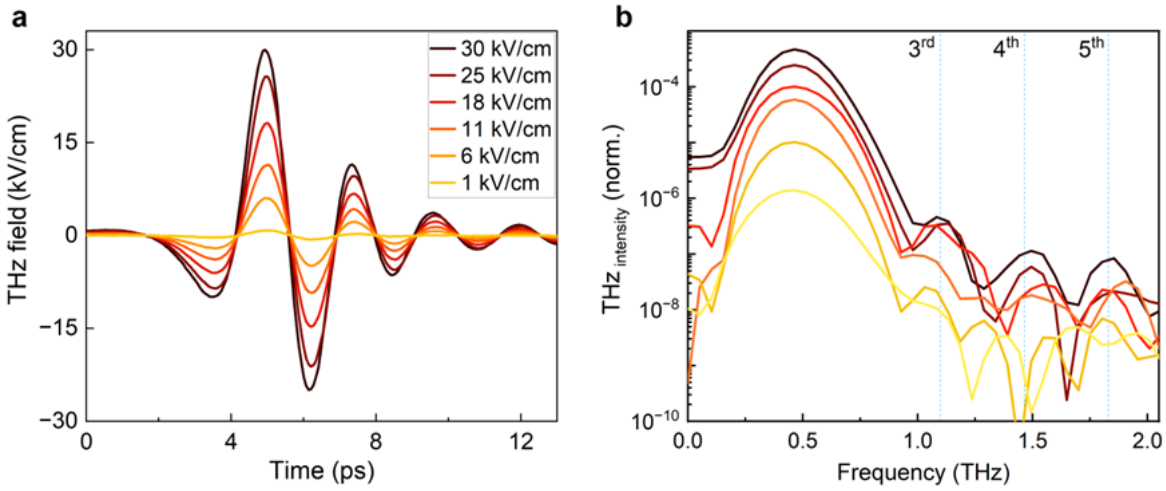

Fig. S3 Power-dependent HHG in GO. **a** Time-domain THz transients of the pump pulse at various peak electric field strengths ranging from 1 to 30 kV/cm. **b** Corresponding HHG spectra generated at 220 nm - thick GO sample. Dashed blue lines indicate the calculate 3rd, 4th, and 5th harmonics relative to the ~0.37 THz pump frequency.

Section S4: Theoretical saturable transmission model based on a two-level system

To interpret the field-dependent nonlinear transmission observed experimentally, we develop a theoretical model based on electron dynamics in a two-level system[4]. The model establishes a link

between the observed transmission T and the imaginary part of the material's optical susceptibility χ, which is directly related to absorption.

For a material with refractive index $n = \sqrt{1+\chi} \approx 1+\chi$, a plane-wave electric field propagating through a medium can be expressed as:

$$E(z,t) = E_0 \exp[ink_0 z - i\omega t] + c.c. \tag{1}$$

where the vacuum wave vector $k_0 = \omega_0/c$ and ω_0 is the angular frequency, c is the speed of light in vacuum and z is the propagation distance. If we focus on the phase term of the electric field, we have:

$$\begin{aligned} &\exp(ink_0 z) = \exp[i(1+\chi)k_0 z] = \exp[i(1+\mathrm{Re}(\chi))k_0 z] \cdot \exp[-\mathrm{Im}(\chi)k_0 z] \\ &\approx \exp[i(1+\chi)k_0 z] = \exp[i(1+\mathrm{Re}(\chi))k_0 z][1-\mathrm{Im}(\chi)k_0 z] \end{aligned} \tag{2}$$

From Eq. (2), we know that the transmission of the electric field T can be written as

$$T = E(z)/E(0) \approx 1 - \mathrm{Im}(\chi)k_0 z \tag{3}$$

We simplify the material as a two-level system with energy levels denoted by $|1\rangle$ and $|0\rangle$ with energies E1 and E0, respectively. The corresponding density matrix element is denoted as ρ_{ij}, $i, j \in \{0, 1\}$. By denoting $\sigma_{10} = \rho_{10} \exp(i\omega t)$ and $W = \rho_{11} - \rho_{00}$, the time evolution of density matrix elements can be written as

$$\frac{d\sigma_{10}}{dt} = \left(i\Delta - \frac{1}{T_2} \right)\sigma_{10} - \frac{i}{2}\Omega W \tag{4}$$

$$\frac{dW}{dt} = -\frac{W - W^{(eq)}}{T_1} + i(\Omega\sigma_{01} - \Omega^*\sigma_{10}) \tag{5}$$

where $\Delta = \omega - \omega_{10} - e\mathbf{E}\cdot(\eta_{11} - \eta_{00})/\hbar, \omega_{10} = (\varepsilon_1 - \varepsilon_0)/\hbar$, $e > 0$ is the elementary charge, $\hbar$ is the Planck constant, $\eta_{11} - \eta_{00}$ is the Berry connection. With the transition dipole between $|1\rangle$ and $|0\rangle$

defined as r_{10}, the Rabi frequency is denoted by $\Omega_{10} = 2eE \cdot r_{10}/\hbar$. By obtaining the steady state solution $\frac{d}{dt}\sigma_{10} = \frac{dW}{dt} = 0$, we obtain

$$W = \frac{W^{(eq)}\left(1/T_2^2 + \Delta^2\right)}{1/T_2^2 + \Delta^2 + \Omega^2 T_1/T_2}, \tag{6}$$

$$\sigma_{10} = \frac{\Omega}{2} \cdot \frac{-W^{(eq)}\left(1/T_2 + i\Delta\right)}{1/T_2^2 + \Delta^2 + \Omega^2 T_1/T_2} \tag{7}$$

We know that the nonlinear emission, i.e., the high-harmonic emission, is directly related to the polarization P, and we know that

$$P = N\varepsilon_0 \chi E \propto \sigma_{10} r_{01}, \tag{8}$$

where N is the number density of atoms, and ϵ_0 is the vacuum permittivity. Comparing Eqs. (8, 7), we have

$$\mathrm{Im}[\chi] \propto \frac{\Delta}{1/T_2^2 + \Delta^2 + \Omega^2 T_1/T_2} \tag{9}$$

Comparing Eqs.(9, 3), we know that the fitting function of the transmission should be of the following form.

$$T = c + \frac{1}{a_0 + a_1 |E| + a_2 |E|^2} \tag{10}$$

where c and a_i, $i \in \{0, 1, 2\}$ are fitting coefficients. Note that the coefficient a_1 is only non-zero for materials that break the inversion symmetry.

For materials described by two independent two-level systems, such as in our case, where the transmission exhibits a two-step saturation response, the model can be extended by adding a second term of the same form:

$$T = c + \frac{1}{a_0 + a_1 |E| + a_2 |E|^2} + \frac{1}{b_0 + b_1 |E| + b_2 |E|^2} \tag{11}$$

which is the expression we use to fit the measured two-step saturable transmission data in Fig. 4a, b. Here, c, a_i and b_i are fitting coefficients determined from the experimental data (Table S1)

Table S1. Fitting coefficients for GO and rGO obtained from the two-step saturable transmission model used to fit the experimental data.

Sample	c	a_0	a_1	a_2	b_1	b_2	b_3
GO	0.78	16	3	30	12.3	-0.01	0.0.0012
rGO	0.73	20	-5	30	10.8	-0.02	0.00055

Section S5: Spatial phase consistency of the 4th harmonic in GO

To examine the spatial coherence and phase uniformity of the generated even-like harmonic, we analyzed the measured time-domain waveforms of the 4th harmonic component in GO sample. HHG spectra were acquired from six spatially distinct spots across the samples, labeled S1 through S6. For each spot, the 4th harmonic is isolated by numerically applying a narrow spectral bandpass filter around the harmonic peak in the frequency domain, followed by an inverse Fourier transform to reconstruct the corresponding time-domain waveform (Fig. S5).

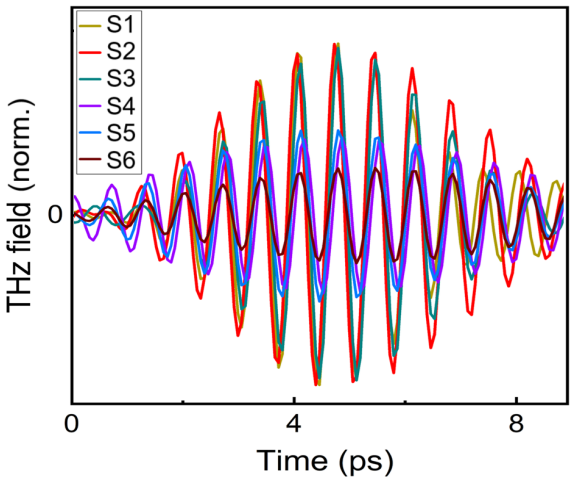

Fig. S5 Spatial phase uniformity of the 4th harmonic in GO. Time-domain waveforms of the 4th harmonic component extracted from six spatially separated spots (S1–S6) on the GO samples. The waveforms were obtained by numerically applying a spectral bandpass filter around the 4th harmonic peak in the measured HHG spectrum, followed by inverse Fourier transformation. All waveforms exhibit consistent phase and temporal profiles, indicating high spatial coherence of the 4th harmonic generation across the sample.

As shown in Fig. S5, the resulting waveforms from all six positions exhibit consistent phase and waveform structure, indicating a high degree of spatial phase uniformity across the sample. This in-phase behavior of the 4^{th} harmonic across macroscopically different sample regions supports the interpretation that the observed even-like harmonic generation is a coherent nonlinear response, rather than a result of random local symmetry breaking.

Section S6: Simulated HHG using a Gaussian pump pulse and saturable transmission model

We performed numerical simulations of HHG using a Gaussian pump pulse to investigate the factors influencing the emergence of even-like harmonics in GO. The two-step saturable transmission (ST) model developed in Section S2 was applied to the time-domain Gaussian pulse, and the resulting nonlinear response was Fourier-transformed to obtain the HHG spectra. We systematically varied three parameters: pump field strength, pulse duration, and carrier–envelope phase (CEP), to assess their impact on the spectral features and to identify conditions that could reproduce the experimentally observed harmonic structure.

Field-dependent analysis of HHG

We analyze the simulated HHG response of GO at three different peak THz field strengths; 1, 30, and 100 kV/cm, as shown in Fig. S6. These values correspond to distinct regimes of the saturable transmission curve in Fig. 4a, whereas 30 kV/cm lies within the plateau region and matches the THz field strength used in our measurements, and 1 kV/cm and 100 kV/cm fall in regions where the transmission increases monotonically with field strength. The simulations reveal that even-like harmonics emerge only when the driving field is in the plateau region (30 kV/cm). In this case, the simulated spectrum reproduces the experimental result, including the 1.45 THz feature corresponding to the 4^{th} harmonic. In contrast, driving fields outside the plateau (1 kV/cm and 100 kV/cm) generate only odd harmonics, consistent with expectations for conventional saturable absorbers such as graphene, whose transmission response (Fig. 4b) can be expanded as a power series in the optical field containing only odd-order terms. Figure S6b provides a zoomed-in view of the higher-frequency components, showing that the simulated HHG at 30 kV/cm agrees closely with the experimentally measured spectrum in GO (red line), both in harmonic positions and relative amplitudes.

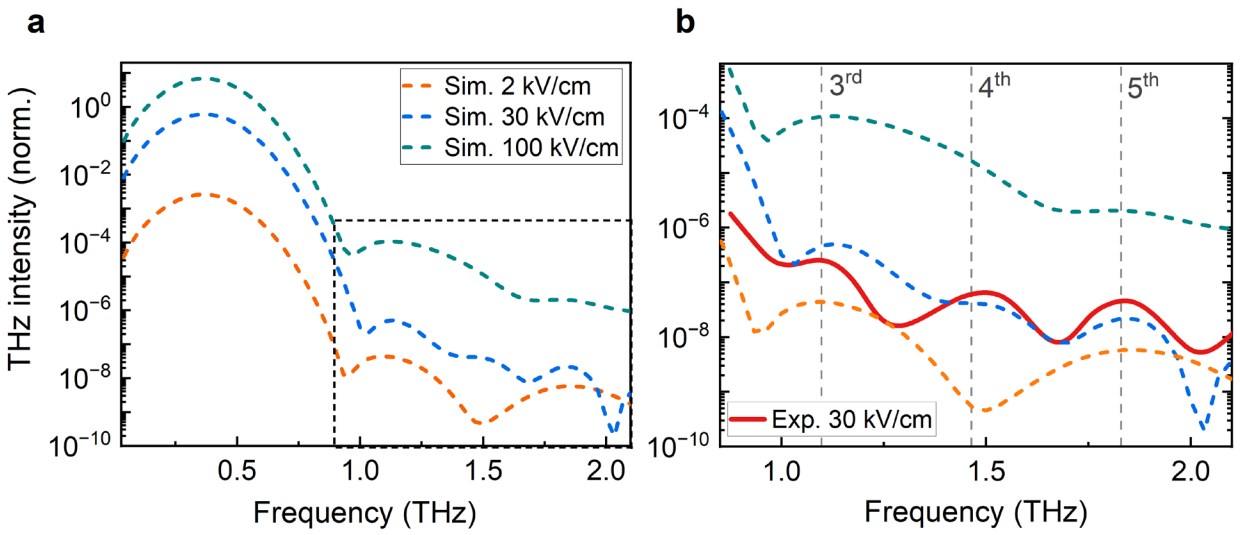

Fig. S6 Field-strength dependence of simulated HHG in GO. a Simulated HHG spectra for peak THz field strengths of 1, 30, and 100 kV/cm. Even-like harmonic emerges only at 30 kV/cm, which lies in the plateau region of the saturable transmission curve (Fig. 4a). **b** Zoomed-in view of the higher-frequency region comparing the simulated spectrum with the measured HHG in GO (red). The simulated HH spectrum at 30 kV/cm shows close agreement with experiment in both harmonic positions and amplitudes.

Pulse duration dependence

Figure S7 shows the time-domain waveforms and corresponding simulated HH spectra for Gaussian pulses with FWHM durations of 1 ps, 1.6 ps, and 3 ps. For longer pulses (e.g., 3 ps), the spectra display well-separated and clearly dominant odd harmonics. As the pulse duration decreases, additional spectral components emerge between the odd harmonics, indicating wave-mixing contributions beyond conventional odd-order generation. At the shortest duration examined (1 ps), the harmonic structure becomes less distinct, and the spectral separation deteriorates, indicating that temporal pulse shortening can disrupt spectral purity.

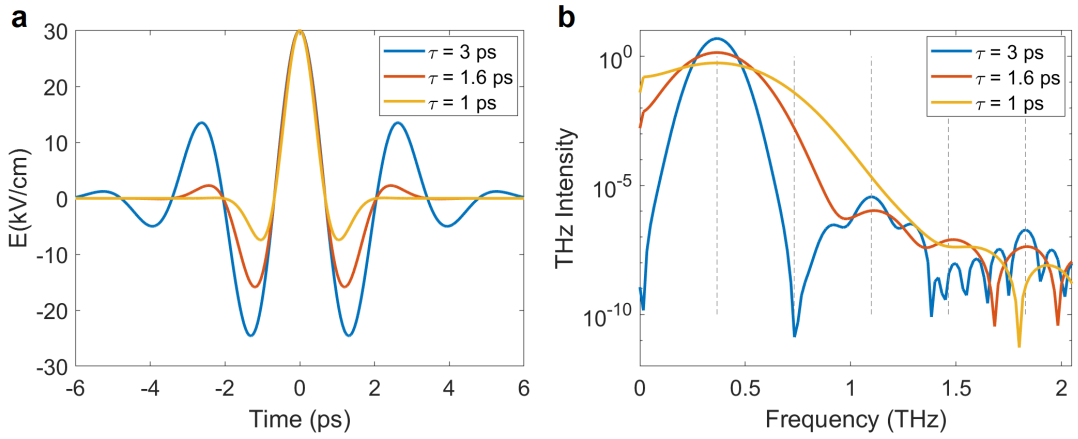

Fig. S7 Pulse duration dependence of HHG in GO. a Simulated time-domain waveforms of Gaussian pump pulses with durations (FWHM) of 1 ps, 1.6 ps, and 3 ps. (b) Corresponding HHG spectrum. Dashed gray lines indicate the fundamental frequency (0.37 THz) and the calculated positions of its odd harmonics.

Carrier-envelope phase (CEP) dependence

To examine the effect of the carrier-envelope phase, we simulated HHG driven by 1 ps and 5 ps pulses with CEP values of 0° and 90°. Figure S8 shows the simulated time-domain waveforms and corresponding HH spectra. For short pulses, the CEP strongly impacts the HHG spectrum: while the odd harmonics remain fixed in frequency, additional spectral features appear between them that are highly sensitive to the CEP. With a CEP of 90°, these features are positioned at the frequencies of even harmonics, whereas shifting the CEP to 0° changes both their position and amplitude. This behavior arises because the CEP modifies the phase relationships among interacting frequency components, altering the constructive and destructive interference conditions for multi-wave mixing. In contrast, for longer pulses containing many oscillation cycles, the relative phase between the carrier and the envelope averages out over the pulse duration, making CEP effects negligible. As a result, the harmonic spectrum remains largely unchanged, and only odd harmonics are observed.

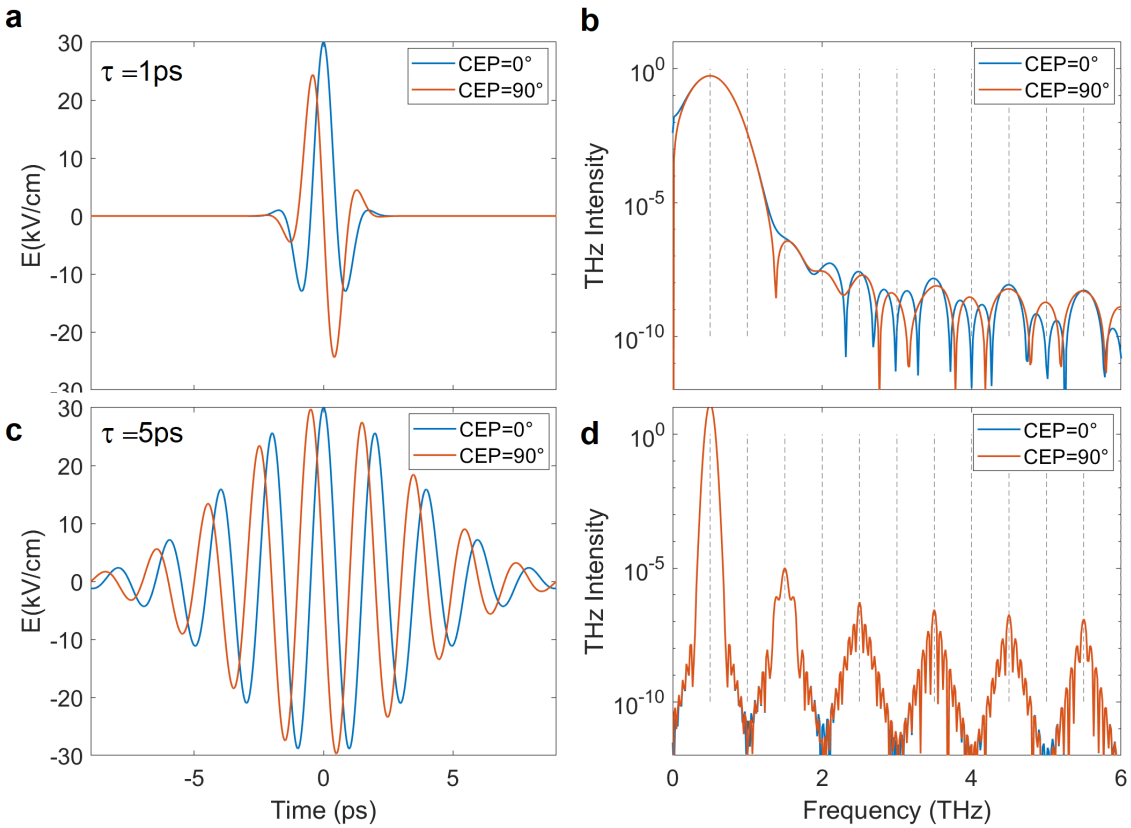

Fig. S8 CEP dependence of HHG in GO. a, Simulated time-domain waveforms of 1 ps Gaussian pump pulses with carrier-envelope phase (CEP) values of 0° and 90°. **b**, Corresponding HHG spectra showing strong CEP dependence, particularly in the emergence and structure of spectral features between odd harmonics **c**, Time-domain waveforms of 5 ps pulses for CEP = 0° and 90°. **d**, Corresponding HHG spectra, where CEP effects are negligible and the harmonic structure remains largely unchanged.

References

1. Ferrari, A. C. & Robertson, J. Interpretation of Raman spectra of disordered and amorphous carbon. *Phys Rev B* **61**, 14095–14107 (2000).

2. Lucchese, M. M. *et al.* Quantifying ion-induced defects and Raman relaxation length in graphene. *Carbon N Y* **48**, 1592–1597 (2010).

3. Maleki, A. *et al.* Metamaterial-based octave-wide terahertz bandpass filters. *Photonics Res* **11**, 526 (2023).

4. Boyd, R. W. *Nonlinear Optics*. *Nonlinear Optics* (Elsevier, 2020).

Chapter 7

Conclusions and Outlook

Summary

This thesis has explored the nonlinear optical behavior of graphitic materials in the THz regime, progressing from theoretical foundations and experimental platform development to the realization of advanced nonlinear effects in engineered 2D systems. The core objective was to understand and enhance HHG and other strong-field nonlinear phenomena in graphene and its functional derivatives under intense THz excitation.

Chapter 1 provided a concise introduction and thesis outline, motivating the importance of nonlinear THz optics in bridging high-speed electronics and photonics, and highlighting the potential of graphitic materials and metamaterials for enabling scalable THz devices.

In **Chapter 2**, we developed the theoretical framework that underpins THz nonlinear optics in 2D materials. We derived the nonlinear wave equation and examined both second- and third-order nonlinear polarizations, including the physics of optical rectification and phase matching. Special emphasis was placed on THz interactions with graphene, covering band structure, intraband and interband conductivity, and the role of field-driven carrier heating. We also introduced graphene oxide (GO) and its reduced forms, highlighting their tunable optical properties, fabrication routes, and potential for supporting symmetry-breaking effects. Finally, we discussed the role of plasmonic metasurfaces and localized surface plasmon resonances in manipulating THz fields and enhancing nonlinear interactions.

Chapter 3 presented the experimental infrastructure established for this work. A table-top tilted-pulse-front THz system was implemented to generate intense, single-cycle THz pulses. We described the design of a flexible detection setup using electro-optic sampling and polarization-sensitive filtering. Fabrication procedures for monolayer and multilayer CVD graphene, electrically gated architectures, and graphene oxide samples were detailed, alongside the design and lithographic fabrication of metamaterial-based spectral filters and metasurfaces. These tools formed the technological backbone for the experiments in later chapters.

In **Chapter 4**, we addressed a key challenge in table-top THz nonlinear optics: the difficulty of detecting weak nonlinear signals due to the broadband and noisy nature of intense THz sources. These limitations significantly complicate the measurement of subtle effects such as third-harmonic generation in thin 2D materials. To address this, we proposed a spectral filtering strategy to enhance detection sensitivity by selectively isolating nonlinear signals from the broadband background. Motivated by this need, we designed and fabricated metamaterial-based THz spectral filters, including octave-wide bandpass filters with sharp roll-offs and high extinction ratios. These filters were specifically engineered to match the THz pulse properties of our table-top system.

In **Chapter 5**, we first implemented the spectral filter configuration developed in Chapter 4—combining bandpass and highpass filters—to enable the detection of weak third-harmonic generation (THG) signals from graphene using a table-top THz source. This filtering setup significantly improved the signal-to-noise ratio and established a baseline for reliable nonlinear measurements. Building on this, we developed a comprehensive strategy to enhance THG efficiency in graphene through three main approaches: (i) increasing the light–matter interaction length by stacking decoupled multilayer graphene sheets, (ii) tuning carrier density via electrostatic gating, and (iii) hybridizing graphene with plasmonic metasurfaces to achieve local field enhancement. These techniques led to up to two orders of magnitude improvement in THG efficiency. However, we also identified an upper limit imposed by linear absorption in multilayer

graphene, with optimal performance around 6–8 layers. This chapter demonstrated how graphene's nonlinear response can be engineered and optimized for THz harmonic generation.

In **Chapter 6**, we addressed this limitation by turning to graphene oxide (GO), a functionalized derivative of graphene with lower linear THz absorption and broken inversion symmetry due to oxygen-containing functional groups. GO enabled the use of thicker films and longer interaction lengths without significant propagation loss. Our experiments revealed a rich nonlinear regime featuring coherent odd and even- like harmonic generation, and a unique saturable transmission behavior. A phenomenological two-level model was developed to explain the observed field-dependent transmission and harmonic spectra. These findings identified saturable transmission as a new mechanism for effective symmetry breaking and wave mixing in 2D materials, and established GO as a tunable platform for nonlinear THz photonics.

In summary, this thesis presents an integrated effort—spanning theoretical modeling, FDTD simulations, device fabrication, spectral filtering, and nonlinear THz spectroscopy—to advance our understanding of strong-field interactions in two-dimensional graphitic systems. To overcome the limitations of broadband and noisy table-top THz sources, we designed and fabricated custom THz spectral filters, enabling sensitive detection of weak nonlinear signals in ultrathin samples. We then developed a comprehensive platform to enhance the THz nonlinearity of 2D materials, implementing a synergistic strategy based on multilayer stacking, electrostatic gating, and plasmonic metasurface integration. This approach led to up to two orders of magnitude enhancement in third-harmonic generation in graphene. Finally, we extended this platform to functionalized systems such as graphene oxide, uncovering a unique THz-driven nonlinear regime characterized by saturable transmission and coherent even-like harmonic generation. Together, these contributions offer new insight into field-driven nonlinear dynamics in 2D materials and provide practical tools for developing scalable, tunable, and reconfigurable THz photonic components for next-generation signal processing and ultrafast optoelectronics.

7.1 Broader implications and future directions

The findings presented in this thesis establish new pathways for understanding and engineering strong-field THz nonlinearities in 2D graphitic materials. While the focus has primarily been on high-harmonic generation (HHG) and saturable transmission, the methods developed here—spanning sample design, spectral filtering, device fabrication, and nonlinear spectroscopy—are versatile and extensible. Several promising research directions emerge from this work.

7.2.1 *Extending nonlinearity enhancement to other 2D materials*

The three-strategy enhancement platform demonstrated in Chapter 5—based on multilayer stacking, gating, and metasurface coupling—was validated for graphene, but the underlying principles are broadly applicable to other 2D materials. Transition metal dichalcogenides (TMDs), black phosphorus, hBN, or emerging Janus monolayers all exhibit tunable optical and electronic properties, some with built-in bandgaps and inherent asymmetry. Applying these strategies to such systems could enable stronger or more diverse nonlinear responses, facilitating exploration of THz harmonic generation, four-wave mixing, or self-phase modulation in platforms previously inaccessible to strong-field optics.

7.2.2 *Expanding the nonlinear toolbox in the THz regime*

To date, this thesis has focused on HHG and saturable absorption, but nonlinear optics in the optical and near-IR domains includes a much wider array of phenomena—such as four-wave mixing, cross-phase modulation, optical Kerr switching, and two-photon absorption. These effects are well-known in the optical regime and form the basis for a wide range of applications, from wavelength conversion to quantum information processing. With appropriate material and device engineering, such nonlinearities could be translated into the THz regime, where they remain largely unexplored. Doing so could unlock new functionalities in THz signal generation, modulation, amplification, and logic.

7.2.3 *Hybridization with electronic THz emitters*

The experiments in this thesis were driven by optical table-top sources that generate broadband THz pulses via optical rectification. However, electronic THz emitters, such as resonant tunneling diodes, HEMTs, or quantum cascade lasers, now operate up to 200–300 GHz and beyond, offering a different class of THz sources that are compact, electrically driven, and frequency-stable. Coupling these electronic sources to nonlinear 2D materials opens up the possibility of on-chip harmonic generation, frequency multiplication, or THz upconversion using practical, scalable hardware. This hybrid opto-electronic direction could serve as a bridge toward compact THz photonic circuits.

7.2.4 *Toward integrated THz nonlinear photonics*

The ability to tune THz nonlinearities via structural design, gating, or chemical functionalization makes graphitic materials ideal for integrated THz photonics. Future work could focus on integrating materials like graphene or GO with on-chip THz waveguides, resonators, or metasurfaces to create reconfigurable nonlinear components. Gated architectures, as demonstrated in this thesis, could enable voltage-controlled harmonic generation or ultrafast optical switching at chip-scale. Combining these capabilities with silicon photonics or polymer-based platforms may lead to hybrid photonic–electronic devices operating in the 0.1–10 THz window.

7.2.5 *Ultrafast control and spectral shaping*

The observation of coherent harmonic generation and saturable transmission suggests that ultrafast dynamic control is possible using THz fields. Future experiments could explore pulse shaping, carrier-envelope phase (CEP) sensitivity, or even feedback-controlled waveform synthesis to manipulate nonlinear responses in real time. Such control could be used to create adaptive THz modulators, programmable harmonic sources, or phase-sensitive logic gates—especially if implemented in integrated or waveguided geometries.

7.2 Final remarks

Through a combination of experimental innovation, nonlinear modeling, FDTD simulations, and material engineering, this thesis advances the growing field of nonlinear terahertz optics. The work establishes graphitic materials—particularly stacked graphene architectures and functional derivatives like graphene oxide—as versatile and tunable platforms for driving strong-field light–matter interactions in the THz regime. The concepts, methods, and results presented here lay a foundation for future research in scalable, reconfigurable, and integrated THz photonic systems, with potential applications in ultrafast signal processing, sensing, and on-chip nonlinear optics.

It is our hope that the tools and insights developed in this thesis will contribute meaningfully to both the scientific understanding and the practical realization of next-generation THz technologies.

References

[1] M. Tonouchi, "Cutting-edge terahertz technology," *Nat Photonics* **1**, 97–105 (2007).

[2] S. S. Dhillon, M. S. Vitiello, E. H. Linfield, A. G. Davies, M. C. Hoffmann, J. Booske, C. Paoloni, M. Gensch, P. Weightman, et al., "The 2017 terahertz science and technology roadmap," *J Phys D Appl Phys* **50**, 043001 (2017).

[3] P. U. Jepsen, D. G. Cooke, and M. Koch, "Terahertz spectroscopy and imaging – Modern techniques and applications," *Laser Photon Rev* **5**, 124–166 (2011).

[4] B. Ferguson and X.-C. Zhang, "Materials for terahertz science and technology," *Nat Mater* **1**, 26–33 (2002).

[5] P. H. Siegel, "Terahertz Technology in Biology and Medicine," *IEEE Trans Microw Theory Tech* **52**, 2438–2447 (2004).

[6] M. B. Heindl, N. Kirkwood, T. Lauster, J. A. Lang, M. Retsch, P. Mulvaney, and G. Herink, "Ultrafast imaging of terahertz electric waveforms using quantum dots," *Light Sci Appl* **11**, 31–33 (Springer US, 2022).

[7] D. Nicoletti and A. Cavalleri, "Nonlinear light–matter interaction at terahertz frequencies," *Adv Opt Photonics* **8**, 401 (2016).

[8] X. Chai, X. Ropagnol, S. M. Raeis-Zadeh, M. Reid, S. Safavi-Naeini, and T. Ozaki, "Subcycle Terahertz Nonlinear Optics," *Phys Rev Lett* **121**, 143901 (American Physical Society, 2018).

[9] S. Koshihara, T. Ishikawa, Y. Okimoto, K. Onda, R. Fukaya, M. Hada, Y. Hayashi, S. Ishihara, and T. Luty, "Challenges for developing photo-induced phase transition (PIPT) systems: From classical (incoherent) to quantum (coherent) control of PIPT dynamics," *Phys Rep* **942**, 1–61 (Elsevier B.V., 2022).

[10] E. A. A. Pogna, X. Jia, A. Principi, A. Block, L. Banszerus, J. Zhang, X. Liu, T. Sohier, S. Forti, et al., "Hot-Carrier Cooling in High-Quality Graphene Is Intrinsically Limited by Optical Phonons," *ACS Nano* **15**, 11285–11295 (2021).

[11] S. D. Ganichev and W. Prettl, "TERAHERTZ NONLINEAR OPTICS," in *Intense Terahertz Excitation of Semiconductors* (Oxford University Press, 2005).

[12] R. W. Boyd, *Nonlinear Optics*, Fourth edi, in *Nonlinear Optics*, Fourth edi (Elsevier, 2020).

[13] J. Dai, J. Liu, and X.-C. Zhang, "Terahertz Wave Air Photonics: Terahertz Wave Generation and Detection With Laser-Induced Gas Plasma," *IEEE Journal of Selected Topics in Quantum Electronics* **17**, 183–190 (2011).

[14] W. Cui, K. M. Awan, R. Huber, K. Dolgaleva, and J. M. Ménard, "Broadband and High-Sensitivity Time-Resolved THz System Using Grating-Assisted Tilted-Pulse-Front Phase Matching," *Adv Opt Mater* **10** (2022).

[15] T. Seifert, S. Jaiswal, U. Martens, J. Hannegan, L. Braun, P. Maldonado, F. Freimuth, A. Kronenberg, J. Henrizi, et al., "Efficient metallic spintronic emitters of ultrabroadband terahertz radiation," *Nat Photonics* **10**, 483–488 (2016).

[16] J. Hebling, G. Almasi, I. Kozma, and J. Kuhl, "Velocity matching by pulse front tilting for large area THz-pulse generation," *Opt Express* **10**, 1161 (2002).

[17] W. Cui, E. K. Yalavarthi, A. V. Radhan, M. Bashirpour, A. Gamouras, and J.-M. Ménard, "High-field THz source centered at 2.6 THz," *Opt Express* **31**, 32468 (2023).

[18] J. Hebling, K.-L. Yeh, M. C. Hoffmann, B. Bartal, and K. A. Nelson, "Generation of high-power terahertz pulses by tilted-pulse-front excitation and their application possibilities," *Journal of the Optical Society of America B* **25**, B6 (2008).

[19] Yun-Shik Lee, *Principles of Terahertz Science and Technology* (Springer US, Boston, MA, 2009).

[20] H. W. Tian, H. Y. Shen, X. G. Zhang, X. Li, W. X. Jiang, and T. J. Cui, "Terahertz metasurfaces: Toward multifunctional and programmable wave manipulation," *Front Phys* **8**, 1–19 (2020).

[21] J. He, X. He, T. Dong, S. Wang, M. Fu, and Y. Zhang, "Recent progress and applications of terahertz metamaterials," *J Phys D Appl Phys* **55** (2022).

[22] L. Wang, Y. Zhang, X. Guo, T. Chen, H. Liang, X. Hao, X. Hou, W. Kou, Y. Zhao, et al., "A review of THz modulators with dynamic tunable metasurfaces," *Nanomaterials* **9**, 965 (2019).

[23] A. V. Kildishev, A. Boltasseva, and V. M. Shalaev, "Planar Photonics with Metasurfaces," *Science (1979)* **339** (2013).

[24] H. T. Chen, A. J. Taylor, and N. Yu, "A review of metasurfaces: Physics and applications," *Reports on Progress in Physics* **79** (IOP Publishing, 2016).

[25] J. He, J. Ye, X. Wang, Q. Kan, and Y. Zhang, "A broadband terahertz ultrathin multi-focus lens," *Sci Rep* **6**, 28800 (Nature Publishing Group, 2016).

[26] W. Withayachumnankul and D. Abbott, "Metamaterials in the terahertz regime," *IEEE Photonics J* **1**, 99–118 (2009).

[27] H. Tao, N. I. Landy, C. M. Bingham, X. Zhang, R. D. Averitt, and W. J. Padilla, "A metamaterial absorber for the terahertz regime: design, fabrication and characterization," *Opt Express* **16**, 7181 (2008).

[28] Q. Zeng, Y. Huang, S. Zhong, T. Lin, Y. Zhong, Z. Zhang, Y. Yu, and Z. Peng, "Multiple Resonances Induced Terahertz Broadband Filtering in a Bilayer Metamaterial," *Front Phys* **10**, 1–8 (2022).

[29] H. Sarieddeen, N. Saeed, T. Y. Al-Naffouri, and M. S. Alouini, "Next generation terahertz communications: A rendezvous of sensing, imaging, and localization," *IEEE Communications Magazine* **58**, 69–75 (2020).

[30] L. Gingras, A. Jaber, A. Maleki, O. Reshef, K. Dolgaleva, R. W. Boyd, and J.-M. Ménard, "Ultrafast modulation of the spectral filtering properties of a THz metasurface," *Opt Express* **28**, 20296 (2020).

[31] A. Maleki, A. Singh, A. Jaber, W. Cui, Y. Xin, B. T. Sullivan, R. W. Boyd, and J.-M. Ménard, "Metamaterial-based octave-wide terahertz bandpass filters," *Photonics Res* **11**, 526 (2023).

[32] L. Gingras, W. Cui, A. W. Schiff-Kearn, J.-M. Ménard, and D. G. Cooke, "Active phase control of terahertz pulses using a dynamic waveguide," *Opt Express* **26**, 13876 (2018).

[33] I. Alonso Calafell, L. A. Rozema, A. Trenti, J. Bohn, E. J. C. Dias, P. K. Jenke, K. S. Menghrajani, D. Alcaraz Iranzo, F. J. García de Abajo, et al., "High-Harmonic Generation Enhancement with Graphene Heterostructures," *Adv Opt Mater* **10** (2022).

[34] H. Y. Hwang, M. Liu, K. Fan, J. Zhang, A. C. Strikwerda, A. Sternbach, N. C. Brandt, B. G. Perkins, X. Zhang, et al., "Metamaterial-enhanced nonlinear terahertz spectroscopy," *EPJ Web Conf* **41** (2013).

[35] A. Di Gaspare, C. Song, C. Schiattarella, L. H. Li, M. Salih, A. Giles Davies, E. H. Linfield, J. Zhang, O. Balci, et al., "Compact terahertz harmonic generation in the Reststrahlenband using a graphene-embedded metallic split ring resonator array," *Nat Commun* **15**, 2312 (2024).

[36] J. C. Deinert, D. Alcaraz Iranzo, R. Pérez, X. Jia, H. A. Hafez, I. Ilyakov, N. Awari, M. Chen, M. Bawatna, et al., "Grating-Graphene Metamaterial as a Platform for Terahertz Nonlinear Photonics," *ACS Nano* **15**, 1145–1154 (2021).

[37] H. Qiu, T. Kurihara, H. Harada, K. Kato, K. Takano, T. Suemoto, M. Tani, N. Sarukura, M. Yoshimura, et al., "Enhancing terahertz magnetic near field induced by a micro-split-ring resonator with a tapered waveguide," *Opt Lett* **43**, 1658 (2018).

[38] H. A. Hafez, S. Kovalev, J. C. Deinert, Z. Mics, B. Green, N. Awari, M. Chen, S. Germanskiy, U. Lehnert, et al., "Extremely efficient terahertz high-harmonic generation in graphene by hot Dirac fermions," *Nature* **561**, 507–511 (Springer US, 2018).

[39] S. A. Mikhailov and K. Ziegler, “Nonlinear electromagnetic response of graphene: frequency multiplication and the self-consistent-field effects,” *Journal of Physics: Condensed Matter* **20**, 384204 (2008).

[40] X. Sun, S. Chen, C. Kuang, W. Fu, X. Li, Z. Duan, and Q. Wen, “Gradient-Reduced Graphene Oxide Aerogel with Ultrabroadband Absorption from Microwave to Terahertz Bands,” *ACS Appl Nano Mater* **6**, 3893–3902 (2023).

[41] X. Xing, L. Zhao, Z. Zhang, L. Fang, Z. Fan, X. Liu, X. Lin, J. Xu, J. Chen, et al., “Photoinduced Terahertz Conductivity and Carrier Relaxation in Thermal-Reduced Multilayer Graphene Oxide Films,” *Journal of Physical Chemistry C* **121**, 2451–2458 (2017).

[42] S. Naserbakht, A. Maleki, S. Mohajer, K. Hesari, M. H. Majlesara, and Z. Shaban, “Nonlinear optical response of liquid crystalline matrix doped with single walled carbon nanotube and graphene sheets,” *J Mol Liq* **222**, 1212–1217 (Elsevier B.V., 2016).

[43] F. Shafipour, S. Salmani, A. Maleki, and M. H. M. Ara, “Nonlinear optical properties of nematic liquid crystal matrix doped with graphene nanosheets,” *Phase Transitions* **94**, 871–884 (2021).

[44] Z. Mics, K. J. Tielrooij, K. Parvez, S. A. Jensen, I. Ivanov, X. Feng, K. Müllen, M. Bonn, and D. Turchinovich, “Thermodynamic picture of ultrafast charge transport in graphene,” *Nat Commun* **6**, 1–7 (2015).

[45] A. H. . Castro Neto, N. M. R. . Peres, K. S. . Novoselov, A. K. . Geim, and F. Guinea, “The electronic properties of graphene,” *Rev Mod Phys* **81**, 109–162 (2009).

[46] F. Bonaccorso, Z. Sun, T. Hasan, and A. C. Ferrari, “Graphene photonics and optoelectronics,” *Nat Photonics* **4**, 611–622 (2010).

[47] A. Maleki, M. B. Heindl, Y. Xin, R. W. Boyd, G. Herink, and J. M. Ménard, “Strategies to enhance THz harmonic generation combining multilayered, gated, and metamaterial-based architectures,” *Light Sci Appl* **14**, 1–10 (Springer US, 2025).

[48] H. A. Hafez, S. Kovalev, K. Tielrooij, M. Bonn, M. Gensch, and D. Turchinovich, “Terahertz Nonlinear Optics of Graphene: From Saturable Absorption to High-Harmonics Generation,” *Adv Opt Mater* **8** (2020).

[49] S. Kovalev, H. A. Hafez, K. J. Tielrooij, J. C. Deinert, I. Ilyakov, N. Awari, D. Alcaraz, K. Soundarapandian, D. Saleta, et al., “Electrical tunability of terahertz nonlinearity in graphene,” *Sci Adv* **7**, 1–10 (2021).

[50] S. Cha, M. Kim, Y. Kim, S. Choi, S. Kang, H. Kim, S. Yoon, G. Moon, T. Kim, et al., "Gate-tunable quantum pathways of high harmonic generation in graphene," *Nat Commun* **13**, 1–10 (Springer US, 2022).

[51] Y. Zhang, J. Wu, L. Jia, Y. Qu, Y. Yang, B. Jia, and D. J. Moss, "Graphene Oxide for Nonlinear Integrated Photonics," *Laser Photon Rev* **17**, 1–28 (2023).

[52] J. Wu, H. Lin, D. J. Moss, K. P. Loh, and B. Jia, "Graphene oxide for photonics, electronics and optoelectronics," *Nat Rev Chem* **7**, 162–183 (2023).

[53] X. Xu, X. Zheng, F. He, Z. Wang, H. Subbaraman, Y. Wang, B. Jia, and R. T. Chen, "Observation of Third-order Nonlinearities in Graphene Oxide Film at Telecommunication Wavelengths," *Sci Rep* **7**, 1–7 (Springer US, 2017).

[54] Y. Zhang, J. Wu, Y. Yang, Y. Qu, L. Jia, T. Moein, B. Jia, and D. J. Moss, "Enhanced Kerr Nonlinearity and Nonlinear Figure of Merit in Silicon Nanowires Integrated with 2D Graphene Oxide Films," *ACS Appl Mater Interfaces* **12**, 33094–33103 (2020).

[55] Y. Qu, J. Wu, Y. Yang, Y. Zhang, Y. Liang, H. El Dirani, R. Crochemore, P. Demongodin, C. Sciancalepore, et al., "Enhanced Four-Wave Mixing in Silicon Nitride Waveguides Integrated with 2D Layered Graphene Oxide Films," *Adv Opt Mater* **8** (2020).

[56] I. Russier-Antoine, H. Fakhouri, S. Basu, F. Bertorelle, P. Dugourd, P. F. Brevet, P. Velayudhan, S. Thomas, N. Kalarikkal, et al., "Second harmonic scattering from mass characterized 2D graphene oxide sheets," *Chemical Communications* **56**, 3859–3862 (2020).

[57] S. Kovalev, R. M. A. Dantas, S. Germanskiy, J.-C. Deinert, B. Green, I. Ilyakov, N. Awari, M. Chen, M. Bawatna, et al., "Non-perturbative terahertz high-harmonic generation in the three-dimensional Dirac semimetal Cd3As2," *Nat Commun* **11**, 2451 (2020).

[58] N. C. Panoiu, W. E. I. Sha, D. Y. Lei, and G.-C. Li, "Nonlinear optics in plasmonic nanostructures," *Journal of Optics* **20**, 083001 (2018).

[59] D. H. Auston, K. P. Cheung, J. A. Valdmanis, and D. A. Kleinman, "Cherenkov Radiation from Femtosecond Optical Pulses in Electro-Optic Media," *Phys Rev Lett* **53**, 1555–1558 (1984).

[60] D. Kleinman and D. Auston, "Theory of electrooptic shock radiation in nonlinear optical media," *IEEE J Quantum Electron* **20**, 964–970 (1984).

[61] P. Rasekh, "Kerr Effect at the THz Frequencies" (2020).

[62] H. Hirori, A. Doi, F. Blanchard, and K. Tanaka, “Single-cycle terahertz pulses with amplitudes exceeding 1 MV/cm generated by optical rectification in LiNbO3,” *Appl Phys Lett* **98** (2011).

[63] S. A. Maier, *Plasmonics: Fundamentals and Applications* (Springer US, New York, NY, 2007).

[64] S. V. Gaponenko, *Introduction to Nanophotonics* (Cambridge University Press, 2010).

[65] V. G. Veselago, “THE ELECTRODYNAMICS OF SUBSTANCES WITH SIMULTANEOUSLY NEGATIVE VALUES OF ϵ AND μ,” *Soviet Physics Uspekhi* **10**, 509–514 (1968).

[66] D. R. Smith, W. J. Padilla, D. C. Vier, S. C. Nemat-Nasser, and S. Schultz, “Composite Medium with Simultaneously Negative Permeability and Permittivity,” *Phys Rev Lett* **84**, 4184–4187 (2000).

[67] J. C. Deinert, D. Alcaraz Iranzo, R. Pérez, X. Jia, H. A. Hafez, I. Ilyakov, N. Awari, M. Chen, M. Bawatna, et al., “Grating-Graphene Metamaterial as a Platform for Terahertz Nonlinear Photonics,” *ACS Nano* **15**, 1145–1154 (2021).

[68] W. L. Barnes, A. Dereux, and T. W. Ebbesen, “Surface plasmon subwavelength optics.,” *Nature* **424**, 824–830 (2003).

[69] L. Ju, B. Geng, J. Horng, C. Girit, M. Martin, Z. Hao, H. A. Bechtel, X. Liang, A. Zettl, et al., “Graphene plasmonics for tunable terahertz metamaterials,” *Nat Nanotechnol* **6**, 630–634 (Nature Publishing Group, 2011).

[70] N. S. Kumar, K. C. B. Naidu, P. Banerjee, T. A. Babu, and B. V. S. Reddy, “A review on metamaterials for device applications,” *Crystals (Basel)* **11**, 1–23 (2021).

[71] L. Lin, X. Bi, Y. Gu, F. Wang, and J. Ye, “Surface-enhanced Raman scattering nanotags for bioimaging,” *J Appl Phys* **129** (American Institute of Physics Inc., 2021).

[72] D. S. L. Abergel, V. Apalkov, J. Berashevich, K. Ziegler, and T. Chakraborty, “Properties of graphene: A theoretical perspective,” *Adv Phys* **59**, 261–482 (2010).

[73] H. A. Hafez, S. Kovalev, K. J. Tielrooij, M. Bonn, M. Gensch, and D. Turchinovich, “Terahertz Nonlinear Optics of Graphene: From Saturable Absorption to High-Harmonics Generation,” *Adv Opt Mater* **8** (2020).

[74] P. R. Wallace, “The Band Theory of Graphite,” *Physical Review* **71**, 622–634 (1947).

[75] G. Wang, A. Chernikov, M. M. Glazov, T. F. Heinz, X. Marie, T. Amand, and B. Urbaszek, “Excitons in atomically thin transition metal dichalcogenides,” *Rev Mod Phys* **90**, 021001 (2018).

[76] Y. Zhang, T.-T. Tang, C. Girit, Z. Hao, M. C. Martin, A. Zettl, M. F. Crommie, Y. R. Shen, and F. Wang, "Direct observation of a widely tunable bandgap in bilayer graphene," *Nature* **459**, 820–823 (2009).

[77] D. C. Elias, R. R. Nair, T. M. G. Mohiuddin, S. V. Morozov, P. Blake, M. P. Halsall, A. C. Ferrari, D. W. Boukhvalov, M. I. Katsnelson, et al., "Control of Graphene's Properties by Reversible Hydrogenation: Evidence for Graphane," *Science (1979)* **323**, 610–613 (2009).

[78] S. Tamaru, M. Ikeda, Y. Shimidzu, S. Matsumoto, S. Takeuchi, and I. Hamachi, "Fluidic supramolecular nano- and microfibres as molecular rails for regulated movement of nanosubstances," *Nat Commun* **1**, 20 (2010).

[79] J. M. Dawlaty, S. Shivaraman, J. Strait, P. George, M. Chandrashekhar, F. Rana, M. G. Spencer, D. Veksler, and Y. Chen, "Measurement of the optical absorption spectra of epitaxial graphene from terahertz to visible," *Appl Phys Lett* **93** (2008).

[80] H. Choi, F. Borondics, D. A. Siegel, S. Y. Zhou, M. C. Martin, A. Lanzara, and R. A. Kaindl, "Broadband electromagnetic response and ultrafast dynamics of few-layer epitaxial graphene," *Appl Phys Lett* **94** (2009).

[81] S. Winnerl, M. Orlita, P. Plochocka, P. Kossacki, M. Potemski, T. Winzer, E. Malic, A. Knorr, M. Sprinkle, et al., "Carrier Relaxation in Epitaxial Graphene Photoexcited Near the Dirac Point," *Phys Rev Lett* **107**, 237401 (2011).

[82] K. F. Mak, M. Y. Sfeir, Y. Wu, C. H. Lui, J. A. Misewich, and T. F. Heinz, "Measurement of the Optical Conductivity of Graphene," *Phys Rev Lett* **101**, 196405 (2008).

[83] S. Das Sarma, S. Adam, E. H. Hwang, and E. Rossi, "Electronic transport in two-dimensional graphene," *Rev Mod Phys* **83**, 407–470 (2011).

[84] Y. Zhang, V. W. Brar, C. Girit, A. Zettl, and M. F. Crommie, "Origin of spatial charge inhomogeneity in graphene," *Nat Phys* **5**, 722–726 (2009).

[85] M. T. R. E. GLOVER, "Conductivity of Superconducting Films for Photon Energies between 0.3 and 40k T,~," *Physical Review*, 182–182 (1934).

[86] H. Y. Hwang, N. C. Brandt, H. Farhat, A. L. Hsu, J. Kong, and K. A. Nelson, "Nonlinear THz Conductivity Dynamics in P-Type CVD-Grown Graphene," *J Phys Chem B* **117**, 15819–15824 (2013).

[87] V. Bianchi, T. Carey, L. Viti, L. Li, E. H. Linfield, A. G. Davies, A. Tredicucci, D. Yoon, P. G. Karagiannidis, et al., "Terahertz saturable absorbers from liquid phase exfoliation of graphite," *Nat Commun* **8**, 15763 (2017).

[88] J. Gosciniak and D. T. H. Tan, “Theoretical investigation of graphene-based photonic modulators,” *Sci Rep* **3**, 1897 (2013).

[89] I.-T. Lin, J.-M. Liu, K.-Y. Shi, P.-S. Tseng, K.-H. Wu, C.-W. Luo, and L.-J. Li, “Terahertz optical properties of multilayer graphene: Experimental observation of strong dependence on stacking arrangements and misorientation angles,” *Phys Rev B* **86**, 235446 (2012).

[90] A. Maleki, M. H. M. Ara, Z. Mousavi, M. Rafiee, Z. Dehghani, and S. Mohajer, “Electro-optical Kerr effect of azo-dye-doped liquid crystals using nulled intensity method,” *Phase Transitions* **1594**, 1–9 (2016).

[91] A. M. Dimiev and S. Eigler, *Graphene Oxide: Fundamentals and Applications*, in *Graphene Oxide: Fundamentals and Applications* (2016).

[92] A. M. Dimiev and J. M. Tour, “Mechanism of Graphene Oxide Formation,” *ACS Nano* **8**, 3060–3068 (2014).

[93] D. Chen, H. Feng, and J. Li, “Graphene oxide: Preparation, functionalization, and electrochemical applications,” *Chem Rev* **112**, 6027–6053 (2012).

[94] K. P. Loh, Q. Bao, G. Eda, and M. Chhowalla, “Graphene oxide as a chemically tunable platform for optical applications,” *Nat Chem* **2**, 1015–1024 (Nature Publishing Group, 2010).

[95] O. C. Compton and S. T. Nguyen, “Graphene oxide, highly reduced graphene oxide, and graphene: Versatile building blocks for carbon-based materials,” *Small* **6**, 711–723 (2010).

[96] J. T. Hong, K. M. Lee, B. H. Son, S. J. Park, D. J. Park, J.-Y. Park, S. Lee, and Y. H. Ahn, “Terahertz conductivity of reduced graphene oxide films,” *Opt Express* **21**, 7633 (2013).

[97] J. Kim, J. Oh, C. In, Y. S. Lee, T. B. Norris, S. C. Jun, and H. Choi, “Unconventional terahertz carrier relaxation in Graphene oxide: Observation of enhanced auger recombination due to defect saturation,” *ACS Nano* **8**, 2486–2494 (2014).

[98] Y. Zhou, E. Yiwen, Z. Ren, H. Fan, X. Xu, X. Zheng, D. Yuan Lei, W. Li, L. Wang, et al., “Solution-processable reduced graphene oxide films as broadband terahertz wave impedance matching layers,” *J Mater Chem C Mater* **3**, 2548–2556 (Royal Society of Chemistry, 2015).

[99] V. Sajeev, S. Rane, D. Ghosh, N. Acharyya, P. Roy Choudhury, A. Mukherjee, and D. Roy Chowdhury, “Terahertz sensing of reduced graphene oxide nanosheets using sub-wavelength dipole cavities,” *Sci Rep* **13**, 1–9 (Nature Publishing Group UK, 2023).

[100] D. Steinberg, R. M. Gerosa, F. N. Pellicer, J. D. Zapata, S. H. Domingues, E. A. Thoroh de Souza, and L. A. M. Saito, “Graphene oxide and reduced graphene oxide as saturable

absorbers onto D-shaped fibers for sub 200-fs EDFL mode-locking," *Opt Mater Express* **8**, 144 (2018).

[101] X. Zhao, Z. B. Liu, W. B. Yan, Y. Wu, X. L. Zhang, Y. Chen, and J. G. Tian, "Ultrafast carrier dynamics and saturable absorption of solution-processable few-layered graphene oxide," *Appl Phys Lett* **98** (2011).

[102] Y. Zhang, J. Wu, Y. Yang, Y. Qu, L. Jia, B. Jia, and D. J. Moss, "Enhanced Spectral Broadening of Femtosecond Optical Pulses in Silicon Nanowires Integrated with 2D Graphene Oxide Films," *Micromachines (Basel)* **13** (2022).

[103] J. Qian, D. Wang, F. H. Cai, W. Xi, L. Peng, Z. F. Zhu, H. He, M. L. Hu, and S. He, "Observation of multiphoton-induced fluorescence from graphene oxide nanoparticles and applications in invivo functional bioimaging," *Angewandte Chemie - International Edition* **51**, 10570–10575 (2012).

[104] A. Leitenstorfer, S. Hunsche, J. Shah, M. C. Nuss, and W. H. Knox, "Detectors and sources for ultrabroadband electro-optic sampling: Experiment and theory," *Appl Phys Lett* **74**, 1516–1518 (1999).

[105] F. Blanchard, L. Razzari, H. C. Bandulet, G. Sharma, R. Morandotti, J. C. Kieffer, T. Ozaki, M. Reid, H. F. Tiedje, et al., "Generation of 1.5 μJ single-cycle terahertz pulses by optical rectification from a large aperture ZnTe crystal," *Opt Express* **15**, 13212 (2007).

[106] S. Scarfe, W. Cui, A. Luican-Mayer, and J. M. Ménard, "Systematic THz study of the substrate effect in limiting the mobility of graphene," *Sci Rep* **11**, 1–9 (Nature Publishing Group UK, 2021).

[107] S. Scarfe, "Optical Properties of Graphene in the Terahertz Region" (2020).

[108] A. Das, S. Pisana, B. Chakraborty, S. Piscanec, S. K. Saha, U. V. Waghmare, K. S. Novoselov, H. R. Krishnamurthy, A. K. Geim, et al., "Monitoring dopants by Raman scattering in an electrochemically top-gated graphene transistor," *Nat Nanotechnol* **3**, 210–215 (2008).

[109] H. M. Li, K. Xu, B. Bourdon, H. Lu, Y. C. Lin, J. A. Robinson, A. C. Seabaugh, and S. K. Fullerton-Shirey, "Electric Double Layer Dynamics in Poly(ethylene oxide) LiClO4 on Graphene Transistors," *Journal of Physical Chemistry C* **121**, 16996–17004 (2017).

[110] I. Bargaoui, N. Bitri, and J. M. Ménard, "A Comparative Investigation of Chemically Reduced Graphene Oxide Thin Films Deposited via Spray Pyrolysis," *ACS Omega* **7**, 11973–11979 (2022).

[111] B. Green, S. Kovalev, V. Asgekar, G. Geloni, U. Lehnert, T. Golz, M. Kuntzsch, C. Bauer, J. Hauser, et al., "High-field high-repetition-rate sources for the coherent THz control of matter," *Sci Rep* **6** (Nature Publishing Group, 2016).

[112] A. Maleki, A. Jaber, A. Singh, Y. Xin, J.-M. Guay, O. Reshef, K. Dolgaleva, R. W. Boyd, B. Sullivan, et al., "Broadband bandpass THz filters with stacked metasurfaces," in *OSA Advanced Photonics Congress 2021*, (Optica Publishing Group, Washington, D.C., 2021).

[113] A. Maleki, A. Singh, A. Jaber, W. Cui, Y. Xin, B. T. Sullivan, R. W. Boyd, and J.-M. Ménard, "Broadband THz bandpass filters based on multi-layered metasurfaces," in *2023 48th International Conference on Infrared, Millimeter, and Terahertz Waves (IRMMW-THz)*, (IEEE, 2023).

[114] A. Maleki, A. Jaber, L. Gingras, O. Reshef, K. Dolgaleva, R. W. Boyd, and J.-M. Ménard, "FDTD analysis of a tunable THz plasmonic metasurface," in *Frontiers in Optics / Laser Science*, (Optica Publishing Group, Washington, D.C., 2020).

[115] A. Maleki, M. B. Heindl, Y. Xin, R. W. Boyd, G. Herink, and J.-M. Ménard, "Enhanced THz third-harmonic generation in a graphene-metamaterial hybrid structure," in *Advanced Photonics Congress 2024*, (Optica Publishing Group, Washington, D.C., 2024).

[116] A. Maleki, M. Heindl, Y. Xin, R. W. Boyd, G. Herink, and J.-M. Ménard, "Enhanced THz Nonlinearity in a Multi-Layer Graphene Device on a Metasurface," in *2025 Photonics North (PN)*, (IEEE, 2025).